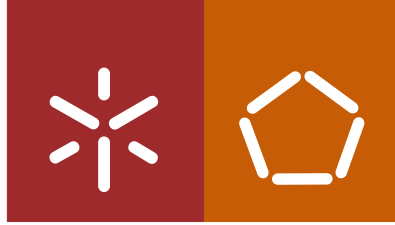




Universidade do Minho
Escola de Engenharia

Duarte Alexandre Campos Serra Moura

**Free-standing Multilayered Membranes
based on Graphene and Natural Polymers
for Biomedical Applications**



Universidade do Minho
Escola de Engenharia

Duarte Alexandre Campos Serra Moura

**Free-standing Multilayered Membranes
based on Graphene and Natural Polymers
for Biomedical Applications**

Dissertação de Mestrado
Mestrado Integrado em Engenharia Biomédica
Ramo de Biomateriais, Reabilitação e Biomecânica

Trabalho efetuado sob a orientação da
Professora Doutora Natália Maria Araújo Alves
e da
**Professora Doutora Maria da Conceição de Jesus
Rego Paiva**

DECLARAÇÃO

Nome: Duarte Alexandre Campos Serra Moura

Endereço eletrónico: a66173@alunos.uminho.pt

Telefone: +351 917 951 615

Número do Bilhete de Identidade: 14103845

Título da dissertação: Free-standing Multilayered Membranes based on Graphene and Natural Polymers for Biomedical Applications

Orientadores: Professora Doutora Natália Maria Araújo Alves

Professora Doutora Maria da Conceição de Jesus Rego Paiva

Ano de conclusão: 2015

Designação do Mestrado: Mestrado Integrado em Engenharia Biomédica

Área de Especialização: Biomateriais, Reabilitação e Biomecânica

Escola de Engenharia

Departamento de Engenharia de Polímeros

É AUTORIZADA A REPRODUÇÃO PARCIAL DESTA DISSERTAÇÃO, APENAS PARA EFEITOS DE INVESTIGAÇÃO, MEDIANTE DECLARAÇÃO ESCRITA DO INTERESSADO, QUE A TAL SE COMPROMETE.

Universidade do Minho, ___/___/_____

Assinatura:

Duarte Alexandre Campos Serra Moura

ACKNOWLEDGEMENTS

This work marks the end of 5 years, that although have passed too fast, it was full of experiences that contributed to my personal and professional growth. Here, I would like to thank all people that directly or indirectly made this journey possible.

First of all, I would like to express my gratitude and acknowledgement to my supervisor Professor Natália Alves, for the guidance, availability and especially for the strong encouragement given, without which it would not have been possible to finish this work.

To my co-supervisor, Professor Conceição Paiva, I also would like to thank for all the advices, suggestions and for all the knowledge passed during this work.

I am also deeply grateful to Professor João Mano for the support, advices and for encourage me to try a semester abroad. Thank you so much Professor, it was an experience that I will never forget.

I also would like to thank all people from 3B's research group, particularly to Sofia Caridade for always being available to help me with the valuable guidelines, for your confidence and above all for your critical and constructive discussions. I am as well really grateful to Catarina Vale, for your constant support along this work and for your availability. To Maria Sousa, I want to thank for the time spent with the cell culture experiments and for your patience to explain me how the "cellular world" works. To Eunice Cunha from Polymer's Department, thank you so much for your kindness and for always being available to spend a lot of time helping me to produce graphene and to answer all my questions.

Although this work did not result from my Erasmus experience, I would like to acknowledge Professor Aldo Boccaccini for his guidance, welcoming and for helping me in my first real lab experience that somehow was important to this work. To all the friends that I met in Germany, in particular to Kim, Mairead and Lars, thank you so much for your friendship, kindness and for being my little multicultural german family.

I am also thankful to all my biomedical engineer friends and to the ones that along with me have entered in this journey, in particular Lisete, Mariana, Zé, Elsa, Daniela, Filipa and Raquel. Thank you so much for the crazy ideas to solve scientific problems, for the endless laughing moments and above all for the advices and company. You made the difference!

To my friends from Paços de Ferreira, I want to thank for the support, good moments and for be there for me in every moment.

To Cláudia, I would like to say that after all these years that I spent with you studying, travelling, laughing, living and fighting to achieve our goals, you have shown me the true meaning of the word friendship. I am absolutely sure that I found my long-standing friend. I could never ever done this without you!

At last I would like to thank to my beloved ones, my family. To my sister and parents, thank you so much for always supporting my decisions, for helping me to pursuit my dreams but above all for being my wonderful and safe shelter. None of this would be possible without you!

“Learn from yesterday, live for today, hope for tomorrow.

The important thing is not to stop questioning.”

- *Albert Einstein*

Membranas Free-Standing Multicamada de Grafeno e Polímeros Naturais para Aplicações Biomédicas

RESUMO

Em diferentes aplicações biomédicas, uma das maiores desvantagens apresentadas pelos polímeros naturais são as baixas propriedades mecânicas. Tais desvantagens têm levado a uma maior procura de soluções, nomeadamente através do desenvolvimento de nanocompósitos de grafeno e de grafeno oxidado. Neste trabalho, foi estudado os benefícios que o uso destes materiais podem trazer para aplicações biomédicas. Para tal, foi usada a técnica de camada-a-camada para a produção de membranas poliméricas *free-standing*, onde, quitosano (CHI, policatião) e alginato (ALG, polianião) foram usados como matriz biopolimérica e o grafeno oxidado (GO) como um nanomaterial de reforço. Antes da deposição das diversas camadas foi necessário proceder à síntese do GO através do método de Hummer modificado, usando para isso dois materiais: a grafite e os nanotubos de carbono de paredes múltiplas (MWNTs), resultando em flocos (o-GF) e nanofitas (o-GNR) de grafeno oxidados, respetivamente.

De modo a alcançar os objetivos propostos foram desenvolvidos 3 tipos de membranas, (CHI/ALG/CHI/ALG)₁₀₀ como controlos, (CHI/ALG/CHI/o-GF)₁₀₀ e (CHI/ALG/CHI/o-GNR)₁₀₀ como prova do conceito. A sua caracterização morfológica foi realizada através do recurso a técnicas como: microscopia eletrónica de varrimento, microscopia de força atómica e mapeamento de Raman. Já as propriedades físicas foram avaliadas através termogravimetria, medição dos ângulos de contacto, pela capacidade de absorção de água e pela perda de massa. Testes de tração e análise mecânica dinâmica foram usados para analisar as propriedades mecânicas. Para além disso, a aplicabilidade das membranas foi ainda testada através de ensaios celulares, usando-se para tal linhas celulares L929.

Os resultados demonstraram que a adição de o-GF e o-GNR resultam num melhoramento mecânico das membranas sem que exista alteração das propriedades térmicas. Ao mesmo tempo foi também registada uma maior rugosidade e hidroflicidade das membranas. No que diz respeito aos testes celulares, as membranas onde o-GF estava presente obtiveram uma maior adesão e proliferação celular. Sendo assim, as membranas com o-GF poderão encontrar várias aplicações biomédicas, nomeadamente em aplicações para a cicatrização de tecidos ou ainda para aplicações cardíacas ou ósseas.

Free-Standing Multilayered Membranes based on Graphene and Natural Polymers for Biomedical Applications

ABSTRACT

In several biomedical applications, one of the major disadvantages of natural polymers is their low mechanical performances. Such drawback has led scientists to search for new materials capable to improve their mechanical properties. In the last few years, graphene and graphene oxide (GO) nanocomposite materials have been proposed to be used in different applications due their outstanding mechanical and electrical properties. We hypothesized that the incorporation of such materials could be useful for biomedical applications. To achieve this goal, we transpose the layer-by-layer technology for the production of nanostructured free-standing (FS) polymeric membranes that have such nanofillers in their composition. To this end, chitosan (CHI, polycation) and alginate (ALG, polyanion) were used as a biopolymeric matrix and GO (polyanion) as a reinforcement nanofiller.

Prior to FS membranes production, different GO were synthesized, using a modified Hummers' method, from two different materials: exfoliated graphite and multi-walled carbon nanotubes, resulting in oxidized graphene flakes (o-GF) and graphene nanoribbons (o-GNR), respectively. Such oxidation process provided oxygen functional groups that among other features improve the bonding with biopolymers. Three membranes were developed, (CHI/ALG/CHI/ALG)₁₀₀ that acted as controls, while (CHI/ALG/CHI/o-GF)₁₀₀ and (CHI/ALG/CHI/o-GNR)₁₀₀ were built up as proof of concept. The morphological analysis was performed by scanning electron microscopy, atomic force microscopy and Raman mapping. The physical properties were assessed by thermogravimetric analysis, water contact angle measurements, water uptake and weight loss. Tensile tests and dynamic mechanical analysis were employed to test the mechanical behavior of the FS membranes. Moreover, biological assays using L929 mouse fibroblasts line were executed to investigate their cytocompatibility.

Our results showed that the addition of both o-GF and o-GNR forms improved the mechanical properties however with no significant changes on the thermal properties. At the same time, the FS membranes presented a rough surface and an hydrophilic behavior. Concerning the cellular assays, the FS membranes with o-GF revealed a better promotion of cell adhesion and proliferation than both controls and o-GNR FS membranes. The outcomes of this thesis suggests that o-GF membranes may have potential for wound healing, cardiac and bone applications.

TABLE OF CONTENTS

Acknowledgements	iii
Resumo	v
Abstract	vii
Table of Contents	ix
List of Abbreviations	xiii
List of Figures	xv
List of Tables	xviii
Chapter 1. Introduction	1
1. Introduction.....	3
1.1 Motivation	3
1.2 Multi-walled Carbon Nanotubes (MWNTs).....	4
1.2.1 Structure	4
1.2.2 Properties	5
1.3 Graphite	6
1.3.1 Structure	6
1.3.2 Properties	7
1.4 Graphene	7
1.4.1 Structure	7
1.4.2 Properties	8
1.5 Production Techniques	9
1.6 Graphene Oxide (GO).....	12
1.7 Natural Polymers.....	13
1.7.1 Chitosan	13
1.7.2 Alginates	15
1.8 Processing Techniques for Free-Standing Membranes	16
1.8.1 Layer-by-Layer (LbL) Assembly.....	17
1.9 Final Remarks	20
1.10 References	22
Chapter 2. State of the Art	29
2. Chitosan Nanocomposites for Biomedical Applications	31
2.1 Introduction.....	32
2.2 Chitosan Nanocomposites	33
2.2.1 Layered Silicates	34
2.2.2 Metal/ceramic Nanoparticles.....	36
2.2.3 Carbon Nanotubes (CNTs).....	38
2.2.4 Graphene based Materials	39
2.3 Materials Processing Strategies for Chitosan Nanocomposites	41
2.3.1 Solvent Casting	41
2.3.2 Freeze Drying	42
2.3.3 Layer-by-layer (LbL)	43
2.3.4 Electrospinning.....	45
2.4 Biomedical Applications.....	47

2.4.1	Bone Tissue Engineering	49
2.4.2	Drug Delivery.....	50
2.4.3	Soft Tissue Applications.....	51
2.4.4	Biosensing	52
2.5	Conclusions	53
2.6	References	55

Chapter 3. Materials and Methods.....67

3.	Materials and Methods	69
3.1	Materials.....	69
3.1.1	Graphene Oxide (GO).....	69
3.1.2	Free-Standing (FS) Multilayered Membranes	69
3.2	Methods.....	70
3.2.1	Synthesis of GO.....	70
3.2.2	Structural Characterization of GO.....	72
3.2.2.1	Thermogravimetric analysis (TGA).....	72
3.2.2.2	Raman spectroscopy	72
3.2.2.3	Ultraviolet-visible (UV-Vis) spectroscopy	73
3.2.2.4	Fourier transform infrared (FTIR) spectroscopy.....	74
3.2.2.5	Zeta potential	74
3.2.3	Production of the FS Multilayered Membranes	75
3.2.4	FS Multilayered Membranes Characterization.....	77
3.2.4.1	Scanning electron microscopy (SEM)	77
3.2.4.2	Atomic force microscopy (AFM) imaging	77
3.2.4.3	Raman mapping.....	78
3.2.4.4	TGA measurements.....	79
3.2.4.5	Water contact angle (WCA) measurements.....	79
3.2.4.6	Water uptake (WU)	80
3.2.4.7	Weight loss.....	80
3.2.4.8	Mechanical characterization	81
3.2.4.8.1	Tensile testing.....	81
3.2.4.8.2	Dynamic mechanical analysis (DMA).....	82
3.2.4.9	Cellular assays	82
3.2.4.9.1	Cell culture and seeding	83
3.2.4.9.2	DAPI-phalloidin staining.....	83
3.2.4.9.3	MTS assay	84
3.2.4.9.4	DNA quantification.....	84
3.3	Statistical Analysis	85
3.4	References	86

Chapter 4. Free-standing Multilayered Membranes based on Graphene and Natural Polymers for Biomedical Applications.....89

4.	Free-Standing Multilayered Membranes based on Graphene and Natural Polymers for Biomedical Applications.....	91
4.1	Experimental Section.....	94
4.1.1	Materials.....	94
4.1.2	Synthesis of GO.....	94

4.1.3	Structural Characterization of GO.....	95
4.1.4	Production of the Free-standing (FS) Multilayered Membranes.....	96
4.1.5	Scanning Electron Microscopy (SEM) of the FS membranes	97
4.1.6	Atomic Force Microscopy (AFM) Imaging.....	97
4.1.7	Raman Mapping.....	97
4.1.8	Thermogravimetric Analysis (TGA).....	97
4.1.9	Contact Angle Measurements	97
4.1.10	Water Uptake (WU).....	98
4.1.11	Weight Loss.....	98
4.1.12	Mechanical Characterization.....	99
4.1.13	Biological Assays.....	99
4.1.14	Statistical Analysis.....	101
4.2	Results and Discussion.....	101
4.2.1	Structural Characterization of Carbon Nanoparticles Oxides.....	101
4.2.2	Scanning Electronic Microscopy (SEM) Analysis	104
4.2.3	AFM Analysis.....	107
4.2.4	Raman Mapping.....	108
4.2.5	TGA Analysis	109
4.2.6	Water Contact Angle (WCA) Measurements	110
4.2.7	Swelling Ability Studies	111
4.2.8	Biodegradation Studies.....	112
4.2.9	DMA Analysis	113
4.2.10	Tensile Tests.....	114
4.2.11	Biological assays	115
4.3	Conclusions	118
Chapter 5. Conclusions and Future Work.....		125
5.	Conclusions and Future Work	127
5.1	General Conclusions.....	127
5.2	Future Work	128

LIST OF ABBREVIATIONS**A**

A	Ampere
AFM	Atomic force microscopy
Ag NPs	Silver nanoparticles
ALG	Alginate
Au NPs	Gold nanoparticles

B

BG	Bioactive glass
BG NPs	Bioactive glass nanoparticles

C

CHI	Chitosan
cm	Centimeter
CNTs	Carbon nanotubes
cP	Centipoise
CVD	Chemical vapor deposition

D

DAPI	4',6-diamidino-2-phenylindole
DD	Deacetylation degree
2D	Bi-dimensional
3D	Three-dimensional
DMA	Dynamic mechanical analysis
DMEM	Dulbecco's modified eagle medium
DNA	Deoxyribonucleic acid
DW	Distilled water
DWNTs	Double-walled nanotubes

E

E	Young's Modulus
E'	Storage Modulus
EG	Exfoliated graphite
ES	Electrospinning

F

FS	Free-standing
FTIR	Fourier transform infrared spectroscopy

G

g	Grams
---	-------

G-blocks	α -L-gulonate
GICs	Graphite intercalation compounds
GO	Graphene oxide
GPa	Gigapascal

H

h	Hours
HA	Hydroxyapatite
HA NPs	Hydroxyapatite nanoparticles
H_{AV}	Average height value
HCl	Hydrochloric acid
Hz	Hertz

K

K	Kelvin
Kg	Kilograms
kN	Kilonewton
kV	Kilovolts

L

L	Liter
LB	Langmuir-Blodgett
LbL	Layer-by-layer
LD50	Lethal dose for 50% of test population

M

m	Meter
M-blocks	β -D-mannurate
μ M	Micromole
$\mu\Omega$	Microohm
min	Minute
mL	Mililiters
MMT	Montmorillonite
MPa	Megapascal
MTS	3-(4,5-dimethylthiazol-2-yl)-5-(3-carboxymethoxyphenyl)-2-(4-sulfophenyl)-2H-tetrazolium
MWNTs	Multi-walled nanotubes

N

N	Newton
---	--------

nm	Nanometers	UTS	Ultimate tensile strength
NPs	Nanoparticles	UV-vis	Ultraviolet-visible spectroscopy
<u>Q</u>		<u>V</u>	
Ω	Ohm	v/v	Volume/volume
o-EG	Oxidized exfoliated graphite		
o-GF	Oxidized graphene flakes	<u>W</u>	
o-GNR	Oxidized graphene nanoribbons	W	Watts
o-MWNTs	Oxidized multi-walled nanotubes	WCA	Water contact angle
		W_f	Final dry weight
<u>P</u>		W_i	Initial dry weight
PBS	Phosphate Buffered Saline	wt	Mass fraction
PE	Polyelectrolyte	WU	Water uptake
PEI	Poly(ethyleneimine)		
PLL	Poly(L-lysine)	<u>X</u>	
PMMA	Poly(methyl metacrylate)	XRD	X-ray diffraction
PP	Polypropylene		
<u>R</u>		<u>Z</u>	
rGO	Reduced graphene oxide	ZnO NPs	Zinc oxide nanoparticles
RNA	Ribonucleic acid		
rpm	Revolutions per minute		
R_{RMS}	Root mean squared roughness		
<u>S</u>			
S	Siemens		
SAM	Self-assembled monolayer		
SD	Standard Deviation		
SEM	Scanning electron microscopy		
SiC	Silicon carbide		
sq	Square		
SWNTs	Single-walled nanotubes		
<u>I</u>			
Tan δ	Loss factor		
TCPS	Tissue culture polystyrene		
TEM	Transmission electron microscopy		
TGA	Thermogravimetric analysis		
tL	Tetralayer		
TPa	Terapascal		
<u>U</u>			
UHV	Ultrahigh vacuum		

LIST OF FIGURES

Figure 1.1 Number of publications regarding graphene based materials, in the last 10 years, resulting from a literature review carried out using the database Scopus®.....	3
Figure 1.2 Structural representation of the single-walled nanotubes (SMWTs) and the multi-walled nanotubes (MWNTs) [10].....	4
Figure 1.3 Representation of the two CNTs conformations: (a) armchair conformation and (b) zig-zag conformation [7].....	5
Figure 1.4 Physical illustration of the graphite structure [25].....	6
Figure 1.5 (a) Schematic representation of the graphene crystal structure; (b) Structural model of the pristine graphene lattice, where it is possible to observe the ripples presence [4].	8
Figure 1.6 Energy dispersion of the π electrons. It is also possible to visualize the valence band (π) and the conduction band (π^*) as well as the Fermi level where these two connect with each other [37].....	9
Figure 1.7 Schematic representation of the unzipping of a SWNTs and consequent nanoribbon formation [54].	11
Figure 1.8 Chemical structure of GO according to the model proposed by Lerf and Klinowski [44].	12
Figure 1.9 Schematic representation of chitin chemical structure [75].	14
Figure 1.10 Schematic representation of chitosan chemical structure [75].	14
Figure 1.11 Chemical structure of alginate: M and G blocks [83].	15
Figure 1.12 LbL dip coating assembly process representation with the different steps illustration.	19
Figure 2.1 Representation of the basic units (a) Si-O tetrahedron and (b) Al-O octahedron present on the clay minerals [43]. (c) Representation of the different structures resulted from different clay dispersion in the polymeric matrix. (i) Tactoid structures, (ii) intercalated structures and (iii) exfoliated structures [39].....	35
Figure 2.2 Schematic representation of (a) graphene and (b) graphene oxide sheet [90].....	40
Figure 2.3 (a) Schematic representation of the procedure to obtain a membrane/film using the solvent casting method (b) Comparison between the surface of a (i) CHI membrane and (ii) CHI/bioactive glass membrane [115], both obtained by solvent casting.....	42

- Figure 2.4** Representation of **(a)** three main LbL methods: (i) dip coating; (ii) spin coating and (iii) spray coating; and **(b)** Image of a chitosan/alginate free-standing membrane, where (i) represents the membrane obtained by dip coating a polypropylene substrate after 100 cycles and (ii) its respective cross-section SEM picture [128]. 44
- Figure 2.5** Schematic illustration of the different structures resulted from the different building blocks and substrates used in the LbL process [129]. 44
- Figure 2.6 (a)** Representation of the different electrospinning approaches, namely (i) wet-dry spinning, (ii) wet-wet spinning and (iii) co-axial electrospinning. **(b)** Representation of a (i) macroscopic electrospun chitosan fiber mat and (ii) chitosan/hydroxyapatite nanoparticles fibers morphology obtained by SEM with respective insert image at lower magnification [135]. 46
- Figure 3.1** Representation of the color changing along with the procedure evolution. **(a)** Magnetic stirring of the solution with EG and H₂SO₄ (solution completely black); **(b)** solution after adding 300 mL of DW (brownish solution) and **(c)** solution following the H₂O₂ adding (yellow solution).. 70
- Figure 3.2** Schematic representation of the nanoribbons process. **1)** Initial conformation of MWNTs; **2)** Manganate ester formation; **3)** with further oxidation is possible to achieve the dione; **4)** next to the ketones there is distorts of the β,γ alkenes (red part), making them more prone to the next attack by permanganate. As the process continues, the strength ketones induce less strain on the β,γ alkenes since there is more space for carbonyl projection, however the enlarging hole make them more reactive. The opening has been initiate and the ketones can be converted to carboxylic acid which will be responsible for the aligning of the nanoribbons edges; **5)** the nanotube opens and originates the graphene ribbon [3]. 71
- Figure 3.3** Schematic representation of the LbL processing. **(a)** Methodology used to produce (CHI/ALG/CHI/o-GF)₁₀₀ or (CHI/ALG/CHI/o-GNR)₁₀₀ where **1** and **5**: CHI solutions (2 mg/ml; pH=5.5); **2, 4** and **6**: washing solutions (DW; pH=5.5); **3**: ALG solution (2 mg/ml; pH=5.5); **7**: empty cup; **8**: o-GF or o-GNR solutions (0.25 mg/ml; pH=8); **9**: washing solutions (DW; pH=8). **(b)** Methodology used to produce (CHI/ALG/CHI/ALG)₁₀₀, where **1** and **5**: CHI solutions (2 mg/ml; pH=5.5); **2, 4** and **6**: washing solutions (DW; pH=5.5); **3**: ALG solution (2 mg/ml; pH=5.5); **7**: empty cup; **8**: ALG solution (2 mg/ml; pH=5.5); **9**: washing solutions (DW; pH=5.5). 76
- Figure 3.4** Schematic representation of AFM system [22]. 78
- Figure 3.5** Schematic representation of contact angle measurements on a solid surface. **(a)** Hydrophobic surface; **(b)** and **(c)** hydrophilic surfaces [25]. 79

- Figure 4.1** TGA thermograms of **(a)** o-EG and **(b)** o-MWNTs, under a heating rate of 10 °C/min; **(c)** and **(d)** are the Raman spectra obtained at 532 nm for o-EG and pristine EG and o-MWNTs and pristine MWNTs, respectively. 102
- Figure 4.2 (a)** UV-Vis spectra of o-GNR (black line) and o-GF (red line) aqueous solution at a concentration of 0.25 mg/mL. **(b)** FTIR spectra of dried o-GNR (black line) and o-GF (red line). 104
- Figure 4.3** SEM images of **(a₁)** upper side and **(a₂)** substrate side of (CHI/ALG/CHI/ALG)₁₀₀ FS; **(b₁)** upper side and **(b₂)** substrate side of (CHI/ALG/CHI/o-GF)₁₀₀ FS; **(c₁)** upper side and **(c₂)** substrate side of (CHI/ALG/CHI/o-GNR)₁₀₀ FS. The cross-section of each membrane is depicted on **(a₃)**, **(b₃)** and **(c₃)** micrographs. 104
- Figure 4.4** AFM surface images with respective 3D representation of: controls FS membranes **(a; a₁)**, (CHI/ALG/CHI/o-GF)₁₀₀ membranes **(b; b₁)** and (CHI/ALG/CHI/o-GNR)₁₀₀ membranes **(c; c₁)**. **(d)** R_{RMS} and **(e)** is the H_{av} . Significant differences were state for $p < 0.001$ (***) and $p < 0.0001$ (****). 108
- Figure 4.5 (a,c)** Distribution of o-GNR and o-GF (blue) in the polymeric matrix (CHI/ALG) obtained by Raman spectroscopy, with respective intensity color scale (a.u); **(b,d)** optical image of the o-GNR and o-GF composite membranes; **(e,f)** Raman spectra obtained for the o-GNR and o-GF before (black line) and after the dispersion (red line) in the (CHI/ALG) matrix, respectively. 109
- Figure 4.6** TGA graphic representation **(a)** Thermogravimetric (TGA) curves with inset showing a magnification for the temperature range of 792.5-795 °C and **(b)** Derivative of the weight loss curves (DTGA) for all membranes, as a function of temperature (°C). 110
- Figure 4.7** Water contact angle results with representative images for both sides of all membranes. Significant differences were state for $p < 0.0001$ (****). 111
- Figure 4.8.** Variation of the water uptake ability as a function of time of (CHI/ALG/CHI/ALG)₁₀₀ (black round symbol), (CHI/ALG/CHI/o-GF)₁₀₀ (grey triangle symbol) and (CHI/ALG/CHI/o-GNR)₁₀₀ (red square symbol) in PBS at 37 °C. 112
- Figure 4.9** Degradation behavior of (CHI/ALG/CHI/ALG)₁₀₀ (black round symbol), (CHI/ALG/CHI/o-GF)₁₀₀ (grey triangle symbol) and (CHI/ALG/CHI/o-GNR)₁₀₀ (red square symbol) FS membranes when immersed in PBS or Lysozyme over a period of 21 days at 37 °C. 113

Figure 4.10 DMA measurements. Variation of the Storage modulus (a) and the loss factor (b) along a frequency scan ranging from 0.1-15 Hz, at 37°C of the FS membranes while immersed in PBS to closely simulate the physiological conditions. 114

Figure 4.11 Representation and comparison of mechanical properties of controls, o-GNR and o-GF composite membranes. **(a)** Ultimate tensile strength (UTS) and **(b)** strain at break (ϵ_B). Significant differences were found for $p < 0.001$ (***) and $p < 0.0001$ (****). 115

Figure 4.12 Evaluation of cells' morphology using DAPI for nuclei staining (blue labeled) and phalloidin for F-actin filaments staining (red labeled) by fluorescence microscopy at 1, 3, and 7 days post-seeding on (CHI/ALG/CHI/ALG)₁₀₀, (CHI/ALG/CHI/o-GNR)₁₀₀ and (CHI/ALG/CHI/o-GF)₁₀₀ FS membranes. 116

Figure 4.13 (a) Cellular viability analysis for (CHI/ALG/CHI/ALG)₁₀₀, (CHI/ALG/CHI/o-GNR)₁₀₀ and (CHI/ALG/CHI/o-GF)₁₀₀ membranes using the MTS assay for 1,3 and 7 days. **(b)** DNA quantification assay performed on (CHI/ALG/CHI/ALG)₁₀₀, (CHI/ALG/CHI/o-GNR)₁₀₀ and (CHI/ALG/CHI/o-GF)₁₀₀. Significant differences were found for $p < 0.05$ (*), $p < 0.01$ (**), $p < 0.001$ (***) and $p < 0.0001$ (****), N=3. 117

LIST OF TABLES

Table 1.1. Comparison between the different bottom-up techniques for membranes production. 18

Table 2.1. Chitosan based nanocomposites for different biomedical applications. 48

CHAPTER 1. INTRODUCTION

1. INTRODUCTION

The aim of this chapter is to highlight the motivation of the work and to provide the essential information about the materials and production techniques adopted in this thesis.

1.1 Motivation

Could graphene become the material for the next disruptive technology, replacing some of the currently used materials and leading to new markets?[1] This question, mentioned by Nosovlev *et al.* in their paper about “*A roadmap for graphene*”, is the main reason why we decided to investigate this material. In fact, since 2004, when Novosolev and Geim successfully isolated and characterized a single sheet of graphene, the scientific research about this topic has increased exponentially (Figure 1.1) leading to new ways of graphene production suitable for mass fabrication [2, 3].

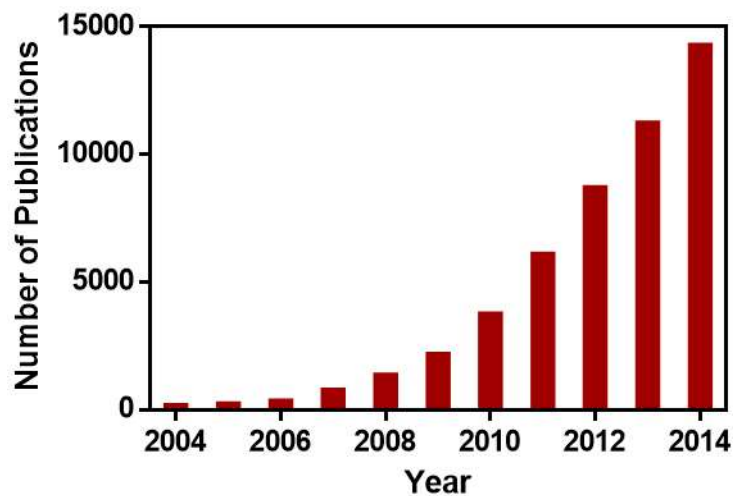


Figure 1.1 Number of publications regarding graphene based materials, in the last 10 years, resulting from a literature review carried out using the database Scopus®.

One of the most common methods of graphene production involves the chemical oxidation of carbon bulk materials such as, graphite and carbon nanotubes, resulting in graphene oxide. This form of graphene is notable for showing excellent aqueous processability, amphiphilicity, ease of surface functionalization, surface and fluorescence quenching ability, and thus revealing important features for biomedical applications [4]. The possibility to use this material as a filler, in particular of natural polymeric matrixes, is a practical approach to achieve nanocomposites with mechanical, optical, barrier and electronic potential [5].

Regarding the aforementioned information, the present work investigates the production of free-standing multilayered composite membranes, by assembling layers of graphene oxide and natural polymers, such as chitosan and alginate, through the layer-by-layer technique. Such membranes, which combine the advantages of graphene and those of natural polymers, such as biodegradability and biocompatibility, may find potential for several biomedical applications, namely for bone or cardiac regeneration.

1.2 Multi-walled Carbon Nanotubes (MWNTs)

1.2.1 Structure

Carbon nanotubes (CNTs), first brought to the attention of the scientific community by S. Iijima in 1991 [6], are seamless tubes of one or more layers of graphene rolled in a concentric way, with open or closed ends [7, 8]. Two major types of carbon nanotubes may be distinguished: the single-walled nanotubes (SWNTs), formed by a rolled single layer of graphene, with a diameter approximately of 1-2 nm; and the multi-walled nanotubes (MWNTs), which are an arrangement of concentric graphite cylinders, held together by secondary van der Waals bonding and separated from each other by 0.35 nm. The diameter of the MWNTs ranges typically from 5 to 20 nm and in some cases it can reach 100 nm, Figure 1.2 [8, 9].

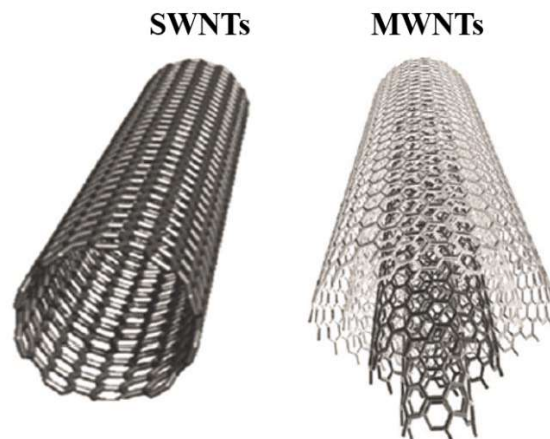


Figure 1.2 Structural representation of the single-walled nanotubes (SMWTs) and the multi-walled nanotubes (MWNTs) [10].

The properties of nanotubes are affected by different parameters, particularly by: the geometry of the atomic arrangement relative to the nanotube axis direction (chirality), diameter, length and morphology. The nanotube chirality is the most influent feature on the CNTs properties, especially on the electronic characteristics. This is described in terms of the tube chirality and it is

affected by the chiral angle (amount of twists in the tube). The chiral angle can adopt different conformations from the zig-zag (chiral angle=0°) to the armchair conformation (chiral angle=30°), Figure 1.3. For angles between 0 and 30° the nanotubes are designed as chiral. Depending on this angle, the carbon nanotubes can be classified as metallic, semi-metallic or semi-conducting [9-11].

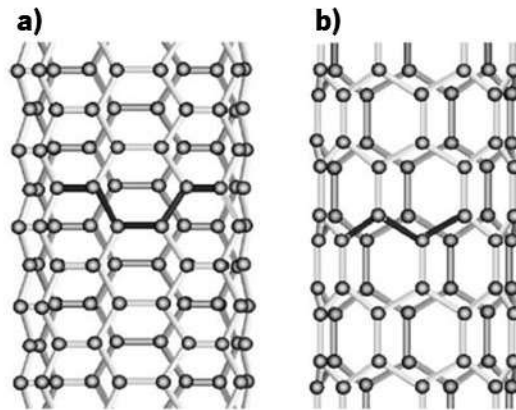


Figure 1.3 Representation of the two CNTs conformations: **(a)** armchair conformation and **(b)** zig-zag conformation [7].

1.2.2 Properties

Focusing on MWNTs, their electrical properties are typical of metallic materials, capable of carry currents up to 10^9 A.cm^{-2} [12]. Mechanically, they have shown an elastic modulus reaching 1 TPa and a tensile strength of 63 GPa [13]. Besides, they present a density near 1.74 g.cm^{-3} and in ideal conditions, where the carbon lattice does not exhibit any defect, the MWNTs are able of a ballistic electron transport. A room temperature thermal conductivity up to $6000 \text{ W.(m.K)}^{-1}$ has been predicted, which is twice as high as diamond [14-17].

MWNTs can be synthesized through different methods, namely: arc-discharge, laser ablation, gas-phase catalytic growth and chemical vapor deposition (CVD) [7, 18, 19]. Among all these techniques, CVD is the most used industrial procedure, once it reveals to be a cost-effective process [20]. However, the MWNTs formed by this method generally present some lattice defects, influencing several physical properties, such as: thermal, mechanical and electronic [9].

Since 1994, after Ajayan *et al.* used CNTs as a polymer fillers [21], different applications have been investigated using MWNTs. For instance, Shin *et al.* demonstrated to achieve functional cardiac patches, to replace damaged heart tissue, by seeding neonatal cardiomyocytes onto MWNTs, incorporated into photo-cross linkable gelatin methacrylate [22]. The electrical

conductivity of the CNTs, as well as, the nanofibrous network formed with the gelatin network, resulted in a patch with enhanced cardiac cell adhesion, excellent mechanical integrity and electrophysiological functions [22]. Other applications have been explored, such as the work done by Holy *et al.* [23], where pluripotent P19 mouse embryonal carcinoma stem cells were seeded onto cell culture glass coverslips coated with MWNTs thin films, using layer-by-layer technique. The cells were either maintained in an undifferentiated state or induced to differentiate by the addition of retinoic acid. The results indicated that the cell adhesion was increased on the MWNTs-coated glass surface and it may facilitate neuronal differentiation of P19 stem cells [23].

1.3 Graphite

1.3.1 Structure

Graphite is a three-dimensional (3D) layered crystal, Figure 1.4, made of stacked parallel graphene sheets that may occur in two different crystal phases: hexagonal and rhombohedral [24]. Typically, the sp^2 orbitals are bonded in a hexagonal network and the graphene sheets are separated from each other by 0.335 nm [25]. Due to the p_z orbitals of the carbon atoms that overlap each other, the lowest energy is obtained when the graphene sheet is completely flat. Graphite is anisotropic due to the differences in the bonding of the carbon atoms in the in-plane and out-of-plane dimensions [25].

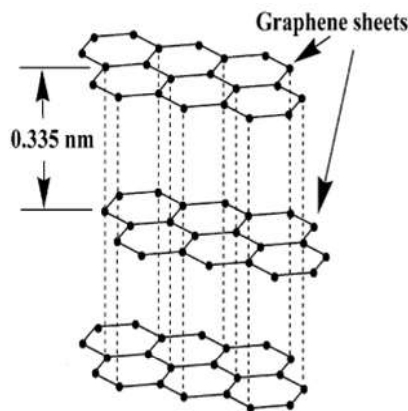


Figure 1.4 Physical illustration of the graphite structure [25].

The carbon bonding in the graphite structure is covalent between the carbon atoms in the in-plane dimension, and based on weak van der Waals forces in the inter-planar area, keeping together the graphene sheets. In fact, these non-covalent interactions allows the graphene sheets

to slide one over the other, giving to the graphite a soft and lubricating character, as well as its most known feature, the ability to mark paper [25, 26].

1.3.2 Properties

Regarding its mechanical properties, graphite is characterized by a high elastic modulus, 1TPa for the in-plane directions, and a good strength value, approximately 130 GPa. It presents a thermal conductivity of $3000 \text{ W} \cdot (\text{m} \cdot \text{K})^{-1}$ and an electrical character along the basal planes with a resistivity of $50 \mu\Omega \cdot \text{cm}$. At the same time, graphite acts as an insulator, perpendicular to the basal planes, being for that, alternatively considered a semi-metal or a zero-gap semiconductor [27-29].

Regarding the production of nanocomposites, high aspect ratio materials are desirable. For that, new methodologies to achieve graphite structures with few layers separated down to a nanometer thickness, presenting high aspect ratio and high modulus, were investigated leading to the production of exfoliated graphite (EG). This type of graphite is produced by separation of the graphite layers through intercalation of alkali metals followed by exfoliation with aqueous solvents [30, 31].

Taking into consideration all these characteristics, graphite has been investigated for varied applications. For instance, Shen *et al.* have developed electrically conductive nanocomposites based on maleic anhydride grafted polypropylene (gPP) and EG [32]. Zanni *et al.* assessed the toxicity and antimicrobial properties of graphite, using the model organism *Caenorhabditis elegans* (*C. elegans*) where the absence of any acute or chronic toxicity was verified [33].

1.4 Graphene

1.4.1 Structure

Graphene, initially called as “graphite layers”, is one of the allotropes of elemental carbon and, in 1960 [34], it was defined as the higher conductive basal plane in the graphite structure.

This material is a monolayer of sp^2 bonded carbon atoms arranged into a two-dimensional (2D) honeycomb like-structure, with a carbon-carbon bond length bond of 0.142 nm, Figure 1.5 a) [35].

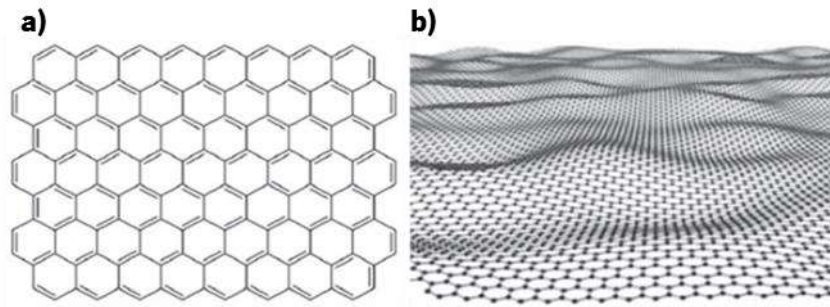


Figure 1.5 (a) Schematic representation of the graphene crystal structure; **(b)** Structural model of the pristine graphene lattice, where it is possible to observe the ripples presence [4].

The graphene lattice may be described by two sub-lattices of σ bonded carbon, where each carbon shows a π orbital that contributes to a delocalized network of electrons [36]. In fact, the chemical bonding of graphene can be explained through the benzene molecule, which consists of a hexagon with σ bonded carbon atoms in the vertices. Each carbon atom is also covalently bonded with hydrogen atoms that stick out from the hexagon in a star-like shape. In addition to the six σ bonds there are three π bonds created by the $2p_z$ orbitals. The result is a hexagon structure with alternate π bonds. So, graphene may be seen as a benzene-type of structure where the hydrogen atoms are replaced by carbon atoms forming a continuous network of carbon hexagons [37].

One of the most interesting features shown by this material is the van der Waals thickness of a graphene sheet (0.34 nm), making it the thinnest 2D filler known to date [38]. According to transmission electron microscopy (TEM) studies, another structural characteristic that should be highlighted is the existence of intrinsic ripples, Figure 1.5 b), which are extremely important, as they influence the graphene properties such as electrical and optical [39].

1.4.2 Properties

As consequence of its structure, graphene presents exceptional mechanical, electrical and thermal properties. It has a high elastic modulus of approximately 1 TPa, the highest known intrinsic electrical conductivity of $6 \times 10^5 \text{ S.m}^{-1}$ and the high thermal conductivity of $5.1 \times 10^3 \text{ W.(m.K)}^{-1}$ [1, 40, 41].

The outstanding electrical and thermal properties are related with the high mobility of the π electrons. The energy dispersion of the π electrons is given by the Figure 1.6, where the Fermi level, situated at the Dirac Points, is formed where the π band (valence band) touches the π^* band (conduction band). This feature provides graphene with a zero gap behavior, which contributes for a unique electronic structure in which the electrons behave as massless particles ballistically

conductive [5, 37, 42]. Besides, graphene also shows a large theoretical specific area of $2630 \text{ m}^2\text{g}^{-1}$, an optical transmittance of 97.7% and a high flexibility [36, 43].

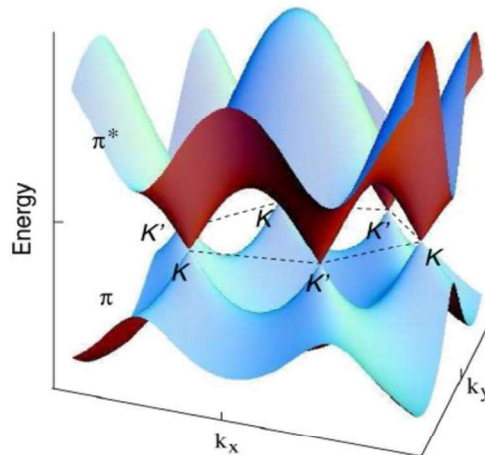


Figure 1.6 Energy dispersion of the π electrons. It is also possible to visualize the valence band (π) and the conduction band (π^*) as well as the Fermi level where these two connect with each other [37].

1.5 Production Techniques

Currently there is a wide number of methods that may be used to produce graphene with various dimensions, shapes and qualities. In general, these methods fall into five main groups:

- (i) Mechanical exfoliation of a single sheet of graphene from bulk graphite, also known as “Scotch tape method”

This technique is a simple peeling process of commercially available graphite that originates thin flakes, which are composed of a monolayer or a few layers of graphene. This process has often demonstrated a low probability to achieve individual graphene sheets [44].

- (ii) Chemical vapor deposition (CVD)

This is the most promising technique reported to be capable of producing mono- or few-layer graphene films [44]. A typical CVD process uses a carbon rich gas precursor, such as methane, which is dissolved on the surface of a metal foil (copper (Cu) or nickel (Ni)) under inert atmosphere and high temperature. Typically the metal substrate is placed in the CVD chamber at 1000°C with a diluted hydrocarbon gas. The incorporation of the carbon atoms into the metal foil starts and after that a rapid cooling process takes place causing an out-diffusion of the carbon atoms to the metal surface [1, 45]. By controlling parameters such as the temperature, and the substrate, single or double layers of graphene can be obtained [38]. However there are some drawbacks such as

the large energy consumption, the defects on grain boundaries and those caused by the removal of the underlying metal, as well as the lack of control over the layer's number [1].

(iii) Epitaxial growth of graphene films from silicon carbide (SiC)

Silicon carbide (SiC) is a common material used for high power electronics and because of that, this technique has been an attractive approach for the electronic field, since it does not require the removal of the underlying substrate. This method uses ultrahigh vacuum (UHV), which when applied to the SiC wafer induces the sublimation of the silicon (Si) atoms, resulting in a graphitized surface. Still, there are some issues with this technique, namely the high cost of the SiC wafers, the high temperature used (above 1000°C) and the small size of the wafers [46, 47].

(iv) Exfoliating graphite towards graphene

This top-down production method may be achieved through two different processes, namely: solution based exfoliation of graphite intercalation compounds (GICs) and chemical oxidation/exfoliation of graphite to graphene oxide (GO) followed by reduction of graphene oxide (rGO) [48]. Regarding the last one, it was first described by Brodie *et al.* [49], in 1859, and since then several changes were made regarding the concentration and types of oxidants agents used [40, 49]. Currently, the most popular method for the production of GO is based on the modifications introduced by Hummers and Offeman in 1958 [50], which consists in the oxidation of graphite by a harsh treatment. The oxidation is carried out by combining graphite powder in sulfuric acid (H_2SO_4) concentrated solution, containing potassium permanganate (KMnO_4) and sodium nitrate (NaNO_3) in the weight proportion of 1:1:3:0.5. When compared to previous methods, this methodology displays the advantage of lower explosion risk and good efficiency [50, 51]. However there is still the drawback of toxic gas release and existence of sodium ions (Na^+) and nitrate ions (NO_3^-), which are difficult to remove from the solution [51].

In order to overcome these limitations a new method (modified Hummer's method) was developed, where the NaNO_3 was replaced by increasing the amount of KMnO_4 , allowing to increase the reaction yield and reduce the toxic gas production [40]. Therefore, this method was chosen to produce the GO used in this work. Due to the structural defects generated during the chemical reaction, the electronic structure of graphene is disrupted. In order to recover this feature, chemical or physical reduction of GO is usually applied [36, 52].

(v) Longitudinal unzipping of carbon nanotubes

Different approaches have been performed and developed to obtain graphene nanoribbons from CNTs. Two approaches have been explored for this top-down synthesis, namely: (i) the cutting or etching of graphene or graphite precursors into narrow graphene strips and (ii) the longitudinal unzipping of CNTs [48].

As an example of the first methodology is the work performed by Day *et al.* [53], where they embedded MWNTs in a poly(methyl methacrylate) (PMMA) film. This film (MWNT-PMMA) was etched by argon plasma and then, in order to remove the polymeric part, solvent vapor was used [53].

The methodology used in this work consisted on the extensive oxidation of carbon nanotubes until their unzipping is achieved. Typically, a chemical attack performed by H_2SO_4 and KMnO_4 at room temperature, followed by a mild heating treatment allows to unzip the CNTs longitudinally. It should be noticed that different opening routes may occur, such as longitudinally or in a spiraling way. These opening mechanisms are dependent of the initial site attack as well as of the chiral angle of CNTs. Although the unzipping was depicted by the authors as starting at one specific point and continuing along the CNTs, Figure 1.7, in fact the CNT wall is extensively oxidized, and it appears that manganate ions (MnO_4^{2-}) has a catalyst action upon breaking the C-C bonds along the CNT length [54]. As a result of the opening process, an oxidized graphene nanoribbon-like structure (o-GNR) is obtained with high water and organic solvents solubility [54]. A further detailed analysis of the opening mechanism is described in the Materials and Methods section.

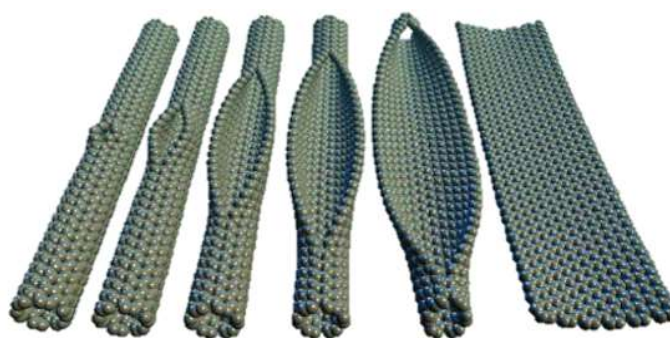


Figure 1.7 Schematic representation of the unzipping of a SWNTs and consequent nanoribbon formation [54].

Although the routes (i),(ii) and (iii) may be preferred for devices that require high quality graphene, due to the quality of the produced graphene, the techniques (iv) and (v) are more attractive for large scale manufacturing, once they represent a scalable possibility to obtain high

volume production and at the same time a versatile technique, in terms of being well suited for chemical functionalization [55].

1.6 Graphene Oxide (GO)

Graphene oxide (GO) is a graphene derivative that has been widely used as an alternative or as a precursor of graphene [38]. A wide number of chemical models have been proposed to describe GO structure, such as the Hoffman's model, the Ruess's model or the most accepted and known - the Lerf and Klinowski model's, Figure 1.8. In this model, hydroxyl and epoxy groups are present on both sides of the basal plane, and carbonyl along with carboxyl acids are distributed in the sheet edges [44]. These containing oxygen groups render GO a biocompatibility and physiological solubility behavior [56].

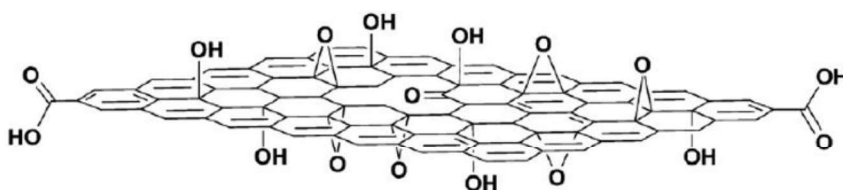


Figure 1.8 Chemical structure of GO according to the model proposed by Lerf and Klinowski [44].

Usually the carbon:oxygen ratio is approximately 2:1 and the oxidized regions can reach up to 70% [44, 57, 58]. This material shows a negative charge in acidic or basic environments, largely due to the carboxyl groups, and the zeta potential is able to reach values in the order of -50 mV for a pH=10.5 [59].

Commonly, GO is described as a hydrophilic carbon material, however recent works suggests GO as an amphiphilic material, once it may present a hydrophobic and hydrophilic domain, depending on the surface region and extent of oxidation [38, 60].

Regarding its mechanical properties, a decrease is observed when compared to graphene, although GO stills exhibit good properties, such as an elastic modulus of 250 GPa and extreme flexibility [61]. One of the major drawbacks caused by the oxidation process is the damage of the sp^2 hybridization and consequently lack in the conductive character shown by graphene. Although not performed in this work, this damage may be partially repaired through a reduction process using hydrazine, among other reducing agents [36, 52].

One of the major advantages of GO is its chemical versatility that allows it to be combined with different materials including polymers, emerging as innovative nanocomposites with enhanced

properties. The interfacial interactions between these materials may be of diverse nature, including: covalent bonding; polymers with a carboxyl terminated groups that can crosslink with GO hydroxyl groups through esterification; electrostatic interactions; and hydrogen bonding between highly polarized donor and acceptors, which are extremely abundant in GO due to its epoxy, hydroxyl, carboxyl and carbonyl groups. Because of that GO can bond with different polar polymers. Depending on the bonding characteristics, different mechanical response may be observed in the composite materials formed [38, 62].

1.7 Natural Polymers

Polymers and more specifically polymeric biomaterials have been investigated and used for health care applications for a long time [63]. A biomaterial is defined as a natural or synthetic material engineered to interface with biological systems to evaluate, treat, augment or replace any type of tissue, organ or function of the body [64, 65].

Regarding natural polymers, it is possible to distinguish three different types: proteins, such as gelatin and collagen; polysaccharides, where it is possible to find materials such as chitosan and alginate; and finally polynucleotides, where it is worth to highlight DNA and RNA [66].

Despite of the material selected, there is an essential prerequisite that needs to be present to classify the material as a biomaterial, the biocompatibility. This feature means that the biomaterial should have the ability to perform its function with an appropriate host response for the desired application [65, 67]. In fact, natural polymers are known for being extremely similar to macromolecular substances which are recognized by the biological environment, and so, the natural polymers are metabolically eliminated. This similarity suppress problems such as toxicity and chronic inflammation reactions, which are related with synthetic polymers. However, one of the main disadvantages of natural polymers is the low processing ability when compared to the synthetic ones, limiting their applications [66].

1.7.1 Chitosan

Chitosan (CHI) is a linear and semi-crystalline polysaccharide obtained from the deacetylation of the natural polymer named chitin (Figure 1.9) by chemical hydrolysis under alkaline conditions or by enzymatic hydrolysis, such as, chitin deacetylase [68]. Apart from cellulose, chitin is the most common biopolymer in the nature, being present in biological structures like: exoskeleton of crustaceans and insects, and also in some fungi cell walls [69-71].

CHI has two allomorphs forms: namely α and β forms, being the first form the most abundant in nature [69, 72].

Identified in 1884, the chemical structure of CHI is composed of glucosamine (2-amino-2-deoxy- β -D-glucan) and *N*-acetyl glucosamine (2-acetamido-2-deoxy- β -D-glucan) units bonded by $\beta(1\rightarrow4)$ glycosidic linkage, Figure 1.10 [69, 73]. The glucosamine amount present in chitin structure reveals its deacetylation degree (DD), and in fact chitin becomes soluble in aqueous acidic conditions when this amount is higher than 60%, being named chitosan. In addition, the DD is responsible for some of the main characteristics presented by CHI, including crystallinity, molecular weight and biological properties [74].

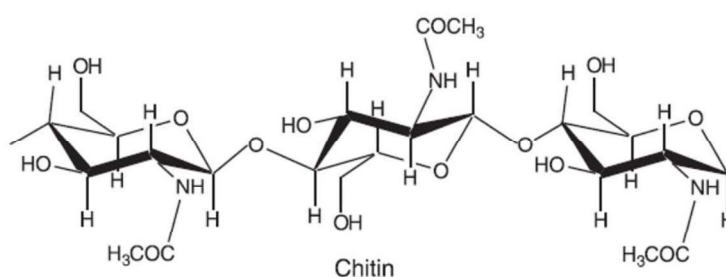


Figure 1.9 Schematic representation of chitin chemical structure [75].

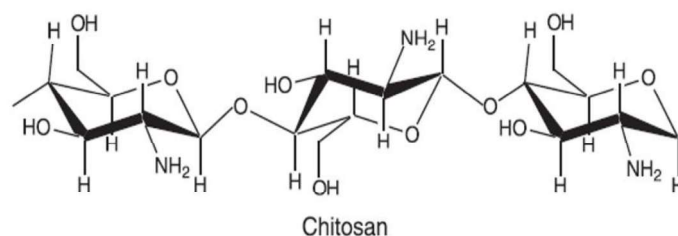


Figure 1.10 Schematic representation of chitosan chemical structure [75].

Taking into considerations the previous figures, it is possible to observe that the main difference between both structures, is the presence of the amino groups in CHI. In fact, this group is responsible for the solubility in acidic solutions ($\text{pH} < 6$), once it might be protonated and its pK_a is 6.3 [76]. This protonation gives CHI a polycationic character allowing it to form ionic complexes with a wide range of synthetic and natural anionic polymers, including alginate [77].

This material has been extensively investigated for healthcare applications, due to the antibacterial, antifungal, mucoadhesive, analgesic and haemostatic activity [73, 75, 78, 79]. Recently, Huang *et al.* has explored the fabrication of CHI into sponges, which according to the

presented results an excellent blood compatibility was achieved, with a lower blood loss and faster degradation than gelatin sponges, showing a promising potential for application of these as hemostatic sponges [80]. Zhang *et al.*, using electrospun nanofibers of hydroxyapatite and CHI, demonstrated to be possible to stimulate the bone formation, once it was shown cell proliferation and mineral deposition [81].

1.7.2 Alginates

Alginates (ALG) are natural polysaccharides extracted from various species of brown seaweed (*Phaeophyceae*) or provide by bacterial biosynthesis, such as *Pseudomonas aeruginosa* [82]. Although ALG obtained from bacterial sources are more chemically and physically well-defined than the ones obtained from brown algae, currently the most common source of ALG comes from this last type of organisms [83, 84]. The extraction from algae can be achieved through a treatment with alkali solution, such as sodium hydroxide (NaOH), followed by a filtration process and precipitation with sodium chloride (NaCl). The purification process, realized with hydrochloric acid (HCl) treatment leads to production of alginic acid which can be converted to salt, ending in a water-soluble sodium alginate powder [84].

The structure of ALG, first reported by Haug *et al.* in 1966 [85], consists in a soluble fraction composed exclusively of β -D-mannurate (M-blocks) or α -L-guluronate (G-blocks) monomers covalently linked through a glycoside bond (1 \rightarrow 4), and in an insoluble part made of alternating M and G residues-Figure 1.11 [83, 86]. It is believed that the G-block length and molecular weight are critical factors that will influence the physical and mechanical properties of ALG. For instance, the high concentration of G-blocks in ALG chain leads to higher stiffness [87]. On the other hand when the amount of M-blocks is higher than G-blocks, the material will be weaker but more flexible [88].

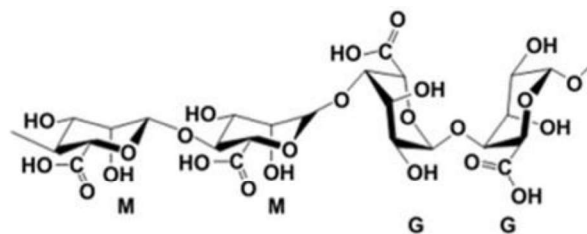


Figure 1.11 Chemical structure of alginate: M and G blocks [83].

Due to the abundance of algae in the nature, ALG can be obtained from different species which will differ in the content and length of each block. The obtained copolymer composition as well as the sequence and molecular weight of the obtained ALG will be dependent of the specie that produce the copolymer. Currently being produced more than 200 different ALG [83, 89].

ALG are hydrophilic polysaccharides that for a pH value above pKa M-blocks and G-blocks (3.38 and 3.65, respectively) are polyanions, due to the negative charge of the carboxylic groups [88]. It is a biocompatible and non-immunogenic material, not inducing any significant inflammatory reaction when implanted in animals, and capable to absorb water 200-300 times of its own weight [90, 91]. One of the main disadvantages of these materials it is its poor biodegradability, once alginase, an enzyme responsible for the degradation process, is not present in human beings or any other mammals [84].

Regarding the above characteristics, ALG have been widely investigated for biomedical applications. Caridade *et al.* has proved to be possible to achieve free-standing membranes, based in ALG and CHI with enhanced permeability and biocompatibility essential for tissue engineering applications [92]. More recently it was shown that the mentioned membranes could be used for bone defects applications when cross-linked with 1-ethyl-3-(3-dimethylaminopropyl)carbodiimide hydrochloride (EDC) since they were able to induce skeletal myoblasts proliferation and differentiate into myotubes. It was also verified that, when loaded with bone morphogenetic protein 2 (BMP-2), the membranes release the growth factor over 1 month providing an osteoinduction effect [93].

1.8 Processing Techniques for Free-Standing Membranes

Commonly, 2D multilayer membranes are made from the adsorption of layers to an underlying substrate. However, one of the major weaknesses of this technique is the impossibility to remove them without any kind of damage [94]. The need to achieve untainted membranes resulted in the development of free-standing (FS) membranes.

FS membranes are consequence of a detachment from the underlying substrate without using any kind of method to remove them, and with the ability to maintain its shape and integrity. In fact, the key factor to obtain these membranes relies on the type of substrate used. Two different types may be chosen: sacrificial templates that will be dissolved by the solvents; or low-energy substrates, such as the polypropylene (PP) substrates used in this work. The latter was first investigated by Larkin *et al.* [95], and the main strategy to get these structures depends on the weak van der Waals interactions between the polyelectrolytes and the substrate [94, 95].

1.8.1 Layer-by-Layer (LbL) Assembly

Different approaches have been reported to obtain membranes, namely: the Langmuir-Blodgett (LB) technique, the self-assembled monolayer (SAM) method, and the layer-by-layer (LbL) process. The last has emerged as an important bottom-up process for surface engineering strategies, once it offers a reliable, easy, versatile and cost effective technique, among other advantages when compared to the LB and SAM methods -Table 1.1 [96].

The LbL assembling, first introduced in 1966 by Iler [97] and later expanded by Decher [98, 99], consists in a sequential adsorption of oppositely charged materials (including polycations and polyanions) on a substrate surface, via electrostatic or non-electrostatic, which includes hydrophobic interactions, hydrogen bonds and van der Waals forces [100]. Typically, a solid support with a negative charge is incubated in the solution containing polycations and a layer is adsorbed (Figure 1.12, step 1). Once the adsorption is carried out at high concentration, the surface charge is effectively reversed. The supports are then rinsed in a washing solution to remove the excess of free polyions and then are immersed in an anionic solution, being the original charge restored (Figure 1.12, step 2). This cycles are repeated until the desired number of layers (Figure 1.12, step 3). Then, (Figure 1.12, step 4) due to the weak van der Waals interactions, the membrane detaches from the substrate, resulting in a FS membrane, step 5 [101].

Table 1.1. Comparison between the different bottom-up techniques for membranes production.

Technique	Advantages	Disadvantages
LB [100, 102, 103]	<ul style="list-style-type: none"> - No restrictions regarding the shape and size of the substrate; - Possible to obtain highly ordered films. 	<ul style="list-style-type: none"> - Expensive; - Requires specialized instrumentation; - Time-consuming; - Requires amphiphilic components; - Limited types of biomolecules can be embedded in the film; - Absence of a strong molecular interaction; - Films mechanically unstable.
SAM [96, 100]	<ul style="list-style-type: none"> - Can be applied to a large number of substances; - Control of the properties in a molecular level. 	<ul style="list-style-type: none"> - Expensive; - Films with limited robustness in physiological conditions; - Need of specific compounds on the substrate; - Not useful for multilayer fabrication.
LbL [96, 104]	<ul style="list-style-type: none"> - Production of robust films; - Discards the use of expensive and specialized equipment; - Does not require activation between the substrate and the building blocks; - Possible to obtain ordered films; - Several materials can be used, including biofunctional molecules; - Attractive technique for biological based applications; - Allows to create higher dimensional structures. 	<ul style="list-style-type: none"> - Time consuming process; - Due to the wide variety interactions, it is difficult to choose the best construction parameters.

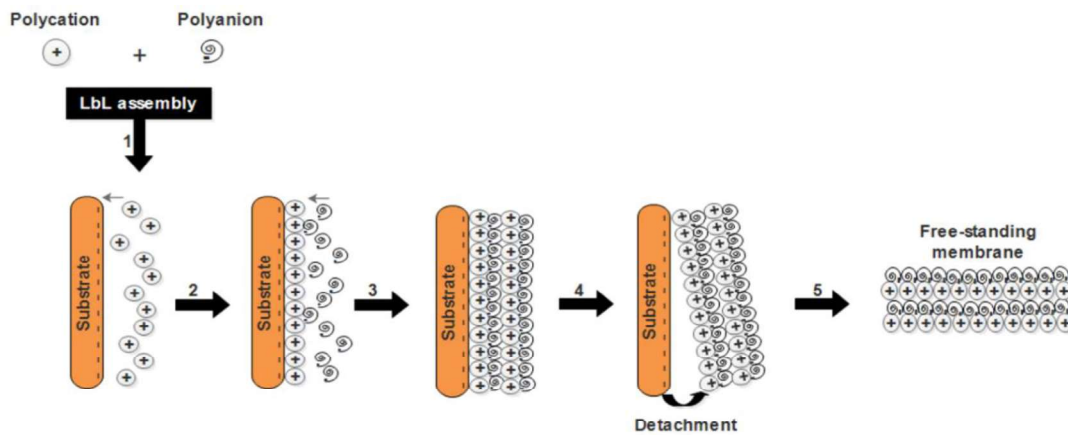


Figure 1.12 LbL dip coating assembly process representation with the different steps illustration.

Even though it is a very simple process, a wide number of parameters affect the assembly of the layers. Starting with the drying steps during the process, it was demonstrated that the thickness of the adsorbed film increases, mainly due to the higher surface roughness arising from the drying. On the other hand, the washing steps between each adsorption are extremely important once it will remove the loosely attached material, and only the effective adsorption stays in the film, fomenting a successful adsorption and a stable film. The temperature is also an important factor, once for higher temperatures, the mobility of the adsorbed molecules is higher and the chances of finding better binding sites is greater [96].

Regarding the intrinsic properties of the polyelectrolytes (PE) solutions, the pH revealed to be extremely important once it varies the protonation state of the ionizable groups and because of that, the availability of the charged groups is altered [96]. The ionic strength also plays a significant role, especially in the membranes thickness. This feature can be tuned with the amount of salt added to the PE, which in turn induces the contraction of the PE with formation of compact globules of reduced net charge resulting in enhanced LbL assembly [103]. PE length ratio, the interaction between the PE chains, the PE concentration and the coexisting electrolyte species are moreover parameters to be taken into consideration [101].

The LbL ability to tailor the physico-chemical properties as well as the structure of different materials has opened new possibilities in different application, such as: biosensing, bioelectronics, drug and gene delivery, food industrialization, cell adesion/differentiation, proliferation, and tissue engineering. Regarding the LBL assembly of different polymers with graphene, a considerable amount of bibliography has been published [105-112]. This possibility was also explored by Shin and co-workers [113], who investigated a 3D tissue construction by alternative cell-seeding and

(poly(L-Lysine) (PLL) and GO deposition. By starting the membranes with a stable and homogeneous layer of 3T3 fibroblasts followed by PLL/GO deposition, it was shown to be possible to achieve a multilayer tissue where each cell layer was strongly attached due to the PLL/GO layer. These authors also have shown the possibility to obtain a spontaneous beating by replacing the 3T3 fibroblasts for a cardiomyocytes layer. Further, Yu *et al.* studied the formation of graphene and carbon nanotubes films for energy-storage applications [114]. Using the LbL process, layers of graphene grafted with poly(ethyleneimine) (PEI) were assembled with carbon nanotubes, resulting in multilayer films with a uniform network structure and well defined nanoscale pores which could serve as a fast electronic and ionic conducting channels, offering electrodes for energy store devices [114].

Bearing in mind the topic of this work, where FS membranes were obtained using the LbL technique, it is important to highlight that no scientific publications were found where CHI and ALG together with graphene based materials were assembled, through LbL, to originate FS membranes.

Besides, to the best of our knowledge, only the work of Wang *et al.* explored the production of FS membranes with GO and CHI, although using a vacuum filtration method, where it was found great mechanical and electrical improvements [115]. Comparing this work with the one developed on this thesis, significant differences were performed, namely, besides CHI and GO we also used ALG, and we produced the FS membranes using only the LbL technique.

1.9 Final Remarks

The possibility to achieve devices with improved targeting, mechanical, and electrical features and, at the same time, with biocompatible and potential regeneration behavior has resulted in the development of promising materials to be further applicable to human situations. Nowadays, one of the major challenges in this field relies on the development of green and more environmental friendly procedures not only to produce graphene, but also to reduce the graphene oxide and restore the electrical behavior. In fact, these ambitious goals have suffered significant improvements in the last few years.

Despite the extensive research about this topic, it is important to notice that, although some information about graphene and GO membranes obtained by LbL has been published, this is not the case of free-standing membranes based on these materials, making this research work extremely valuable. In order to fully understand the great potential to use nanocomposites in the

biomedical field, a review of the state of the art of chitosan-based nanocomposites, including nanocomposites with graphene and GO, among others, will be presented in the next chapter.

1.10 References

- [1] Novoselov KS, Fal'ko VI, Colombo L, Gellert PR, Schwab MG, Kim K. A roadmap for graphene. *Nature*. 2012;490:192-200.
- [2] Novoselov KS, Geim AK, Morozov SV, Jiang D, Zhang Y, Dubonos SV, et al. Electric field effect in atomically thin carbon films. *Science*. 2004;306:666-9.
- [3] Bitounis D, Ali-Boucetta H, Hong BH, Min DH, Kostarelos K. Prospects and Challenges of Graphene in Biomedical Applications. *Advanced Materials*. 2013;25:2258-68.
- [4] Shao YY, Wang J, Wu H, Liu J, Aksay IA, Lin YH. Graphene Based Electrochemical Sensors and Biosensors: A Review. *Electroanalysis*. 2010;22:1027-36.
- [5] Wang Y, Li ZH, Wang J, Li JH, Lin YH. Graphene and graphene oxide: biofunctionalization and applications in biotechnology. *Trends in Biotechnology*. 2011;29:205-12.
- [6] Iijima S. Helical microtubules of graphitic carbon. *Nature*. 1991;354:56-8.
- [7] Thostenson ET, Ren ZF, Chou TW. Advances in the science and technology of carbon nanotubes and their composites: a review. *Composites Science and Technology*. 2001;61:1899-912.
- [8] De Volder MFL, Tawfick SH, Baughman RH, Hart AJ. Carbon Nanotubes: Present and Future Commercial Applications. *Science*. 2013;339:535-9.
- [9] Coleman JN, Khan U, Blau WJ, Gun'ko YK. Small but strong: A review of the mechanical properties of carbon nanotube-polymer composites. *Carbon*. 2006;44:1624-52.
- [10] Farsi M, Sani FM. Effects of multi-walled carbon nanotubes on the physical and mechanical properties of high-density polyethylene/wood flour nanocomposites. *Journal of Thermoplastic Composite Materials*. 2014;27:1139-54.
- [11] Jones DEH. Science of fullerenes and carbon nanotubes - Dresselhaus,MS, Dresselhaus,G, Eklund,PC. *Nature*. 1996;381:384.
- [12] Wei BQ, Vajtai R, Ajayan PM. Reliability and current carrying capacity of carbon nanotubes. *Applied Physics Letters*. 2001;79:1172-4.
- [13] Yu MF, Lourie O, Dyer MJ, Moloni K, Kelly TF, Ruoff RS. Strength and breaking mechanism of multiwalled carbon nanotubes under tensile load. *Science*. 2000;287:637-40.
- [14] Che JW, Cagin T, Goddard WA. Thermal conductivity of carbon nanotubes. *Nanotechnology*. 2000;11:65-9.
- [15] Osman MA, Srivastava D. Temperature dependence of the thermal conductivity of single-wall carbon nanotubes. *Nanotechnology*. 2001;12:21-4.
- [16] Berber S, Kwon YK, Tomanek D. Unusually high thermal conductivity of carbon nanotubes. *Physical Review Letters*. 2000;84:4613-6.
- [17] Collins PG, Avouris P. Nanotubes for electronics. *Scientific American*. 2000;283:62.
- [18] Journet C, Maser WK, Bernier P, Loiseau A, delaChapelle ML, Lefrant S, et al. Large-scale production of single-walled carbon nanotubes by the electric-arc technique. *Nature*. 1997;388:756-8.
- [19] Nikolaev P, Bronikowski MJ, Bradley RK, Rohmund F, Colbert DT, Smith KA, et al. Gas-phase catalytic growth of single-walled carbon nanotubes from carbon monoxide. *Chemical Physics Letters*. 1999;313:91-7.
- [20] Lehman JH, Terrones M, Mansfield E, Hurst KE, Meunier V. Evaluating the characteristics of multiwall carbon nanotubes. *Carbon*. 2011;49:2581-602.
- [21] Ajayan PM, Iijima S. Capillarity-induced filling of carbon nanotubes. *Nature*. 1993;361:333-4.
- [22] Shin SR, Jung SM, Zalabany M, Kim K, Zorlutuna P, Kim SB, et al. Carbon-Nanotube-Embedded Hydrogel Sheets for Engineering Cardiac Constructs and Bioactuators. *Acs Nano*. 2013;7:2369-80.

- [23] Holy J, Perkins E, Yu X. Adhesion, proliferation and differentiation of pluripotent stem cells on multi-walled carbon nanotubes. *Int Nanobiotechnology*. 2011;5:41-6.
- [24] Ooi N, Rairkar A, Adams JB. Density functional study of graphite bulk and surface properties. *Carbon*. 2006;44:231-42.
- [25] Sengupta R, Bhattacharya M, Bandyopadhyay S, Bhowmick AK. A review on the mechanical and electrical properties of graphite and modified graphite reinforced polymer composites. *Progress in Polymer Science*. 2011;36:638-70.
- [26] Mao WL, Mao HK, Eng PJ, Trainor TP, Newville M, Kao CC, et al. Bonding changes in compressed superhard graphite. *Science*. 2003;302:425-7.
- [27] Endo Y. *Advanced composite materials & technology for aerospace application*. Sen-I Gakkaishi. 2004;60:P298-P304.
- [28] Xie XL, Mai YW, Zhou XP. Dispersion and alignment of carbon nanotubes in polymer matrix: A review. *Materials Science & Engineering R-Reports*. 2005;49:89-112.
- [29] Schadler LS. Polymer-based and Polymer-filled Nanocomposites. In: KGaA W-VVGC, editor. *Nanocomposite Science and Technology*. Weinheim 2003. p. 77-153.
- [30] Viculis LM, Mack JJ, Mayer OM, Hahn HT, Kaner RB. Intercalation and exfoliation routes to graphite nanoplatelets. *Journal of Materials Chemistry*. 2005;15:974-8.
- [31] Yasmin A, Luo JJ, Daniel IM. Processing of expanded graphite reinforced polymer nanocomposites. *Composites Science and Technology*. 2006;66:1182-9.
- [32] Shen JW, Chen XM, Huang WY. Structure and electrical properties of grafted polypropylene/graphite nanocomposites prepared by solution intercalation. *Journal of Applied Polymer Science*. 2003;88:1864-9.
- [33] Zanni E, De Bellis G, Bracciale MP, Broggi A, Santarelli ML, Sarto MS, et al. Graphite Nanoplatelets and *Caenorhabditis elegans*: Insights from an in Vivo Model. *Nano Letters*. 2012;12:2740-4.
- [34] Singh V, Joung D, Zhai L, Das S, Khondaker SI, Seal S. Graphene based materials: Past, present and future. *Progress in Materials Science*. 2011;56:1178-271.
- [35] Slonczewski JC, Weiss PR. Band structure of graphite. *Physical Review*. 1958;109:272-9.
- [36] Zhu YW, Murali S, Cai WW, Li XS, Suk JW, Potts JR, et al. Graphene and Graphene Oxide: Synthesis, Properties, and Applications. *Advanced Materials*. 2010;22:3906-24.
- [37] Goerbig MO. Electronic properties of graphene in a strong magnetic field. *Reviews of Modern Physics*. 2011;83:1193-243.
- [38] Hu KS, Kulkarni DD, Choi I, Tsukruk VV. Graphene-polymer nanocomposites for structural and functional applications. *Progress in Polymer Science*. 2014;39:1934-72.
- [39] Meyer JC, Geim AK, Katsnelson MI, Novoselov KS, Booth TJ, Roth S. The structure of suspended graphene sheets. *Nature*. 2007;446:60-3.
- [40] Chen J, Yao BW, Li C, Shi GQ. An improved Hummers method for eco-friendly synthesis of graphene oxide. *Carbon*. 2013;64:225-9.
- [41] Mayorov AS, Gorbachev RV, Morozov SV, Britnell L, Jalil R, Ponomarenko LA, et al. Micrometer-Scale Ballistic Transport in Encapsulated Graphene at Room Temperature. *Nano Letters*. 2011;11:2396-9.
- [42] Zhang YB, Tan YW, Stormer HL, Kim P. Experimental observation of the quantum Hall effect and Berry's phase in graphene. *Nature*. 2005;438:201-4.
- [43] Nair RR, Blake P, Grigorenko AN, Novoselov KS, Booth TJ, Stauber T, et al. Fine structure constant defines visual transparency of graphene. *Science*. 2008;320:1308.
- [44] Compton OC, Nguyen ST. Graphene Oxide, Highly Reduced Graphene Oxide, and Graphene: Versatile Building Blocks for Carbon-Based Materials. *Small*. 2010;6:711-23.

- [45] Li XS, Cai WW, An JH, Kim S, Nah J, Yang DX, et al. Large-Area Synthesis of High-Quality and Uniform Graphene Films on Copper Foils. *Science*. 2009;324:1312-4.
- [46] Forbeaux I, Themlin JM, Debever JM. Heteroepitaxial graphite on 6H-SiC: Interface formation through conduction-band electronic structure. *Physical Review B*. 1998;58:16396-406.
- [47] Berger C, Song ZM, Li TB, Li XB, Ogbazghi AY, Feng R, et al. Ultrathin epitaxial graphite: 2D electron gas properties and a route toward graphene-based nanoelectronics. *Journal of Physical Chemistry B*. 2004;108:19912-6.
- [48] Chen L, Hernandez Y, Feng XL, Mullen K. From Nanographene and Graphene Nanoribbons to Graphene Sheets: Chemical Synthesis. *Angewandte Chemie-International Edition*. 2012;51:7640-54.
- [49] Brodie BC. On the Atomic Weight of Graphite. *Phil. Trans. R. Soc. Lond*; 1859. p. 249-59.
- [50] Hummers WS, Offeman RE. Preparation of graphitic oxide. *Journal of the American Chemical Society*. 1958;80:1339.
- [51] Chung C, Kim YK, Shin D, Ryou SR, Hong BH, Min DH. Biomedical Applications of Graphene and Graphene Oxide. *Accounts of Chemical Research*. 2013;46:2211-24.
- [52] Wang H, Tian HW, Wang SM, Zheng WT, Liu YC. Simple and eco-friendly solvothermal synthesis of luminescent reduced graphene oxide small sheets. *Materials Letters*. 2012;78:170-3.
- [53] Jiao LY, Zhang L, Wang XR, Diankov G, Dai HJ. Narrow graphene nanoribbons from carbon nanotubes. *Nature*. 2009;458:877-80.
- [54] Kosynkin DV, Higginbotham AL, Sinitskii A, Lomeda JR, Dimiev A, Price BK, et al. Longitudinal unzipping of carbon nanotubes to form graphene nanoribbons. *Nature*. 2009;458:872-U5.
- [55] Park S, Ruoff RS. Chemical methods for the production of graphenes. *Nature Nanotechnology*. 2009;4:217-24.
- [56] Shen H, Zhang LM, Liu M, Zhang ZJ. Biomedical Applications of Graphene. *Theranostics*. 2012;2:283-94.
- [57] Kuilla T, Bhadra S, Yao DH, Kim NH, Bose S, Lee JH. Recent advances in graphene based polymer composites. *Progress in Polymer Science*. 2010;35:1350-75.
- [58] Kulkarni DD, Kim S, Chyasnavichyus M, Hu KS, Fedorov AG, Tsukruk VV. Chemical Reduction of Individual Graphene Oxide Sheets as Revealed by Electrostatic Force Microscopy. *Journal of the American Chemical Society*. 2014;136:6546-9.
- [59] Li D, Muller MB, Gilje S, Kaner RB, Wallace GG. Processable aqueous dispersions of graphene nanosheets. *Nature Nanotechnology*. 2008;3:101-5.
- [60] Kim J, Cote LJ, Kim F, Yuan W, Shull KR, Huang JX. Graphene Oxide Sheets at Interfaces. *Journal of the American Chemical Society*. 2010;132:8180-6.
- [61] Suk JW, Piner RD, An JH, Ruoff RS. Mechanical Properties of Mono layer Graphene Oxide. *ACS Nano*. 2010;4:6557-64.
- [62] Pei SF, Cheng HM. The reduction of graphene oxide. *Carbon*. 2012;50:3210-28.
- [63] Ikada Y, Tsuji H. Biodegradable polyesters for medical and ecological applications. *Macromolecular Rapid Communications*. 2000;21:117-32.
- [64] Dhandayuthapani B, Yoshida Y, Maekawa T, Kumar DS. Polymeric Scaffolds in Tissue Engineering Application: A Review. *International Journal of Polymer Science*. 2011:19.
- [65] Ulerly BD, Nair LS, Laurencin CT. Biomedical Applications of Biodegradable Polymers. *Journal of Polymer Science Part B-Polymer Physics*. 2011;49:832-64.
- [66] Ratner B, Hoffman A, Schoen F, Lemons J. *An Introduction to Materials in Medicine*. 3rd ed 2013.
- [67] Nair LS, Laurencin CT. Biodegradable polymers as biomaterials. *Progress in Polymer Science*. 2007;32:762-98.

- [68] Croisier F, Jerome C. Chitosan-based biomaterials for tissue engineering. *European Polymer Journal*. 2013;49:780-92.
- [69] Rinaudo M. Chitin and chitosan: Properties and applications. *Progress in Polymer Science*. 2006;31:603-32.
- [70] Rane KD, Hoover DG. Production of chitosan by fungi. *Food Biotechnology*. 1993;7:11-33.
- [71] Aranaz I, Harris R, Heras A. Chitosan Amphiphilic Derivatives. *Chemistry and Applications. Current Organic Chemistry*. 2010;14:308-30.
- [72] Riva R, Ragelle H, des Rieux A, Duhem N, Jerome C, Preat V. Chitosan and Chitosan Derivatives in Drug Delivery and Tissue Engineering. In: Jayakumar R, Prabakaran M, Muzzarelli RAA, editors. *Chitosan for Biomaterials II*. Berlin: Springer-Verlag Berlin; 2011. p. 19-44.
- [73] Kumar M. A review of chitin and chitosan applications. *Reactive & Functional Polymers*. 2000;46:1-27.
- [74] Alves NM, Mano JF. Chitosan derivatives obtained by chemical modifications for biomedical and environmental applications. *International Journal of Biological Macromolecules*. 2008;43:401-14.
- [75] Jayakumar R, Prabakaran M, Kumar PTS, Nair SV, Tamura H. Biomaterials based on chitin and chitosan in wound dressing applications. *Biotechnology Advances*. 2011;29:322-37.
- [76] Leedy MR, Martin HJ, Norowski PA, Jennings JA, Haggard WO, Bumgardner JD. Use of Chitosan as a Bioactive Implant Coating for Bone-Implant Applications. In: Jayakumar R, Prabakaran M, Muzzarelli RAA, editors. *Chitosan for Biomaterials II*. Berlin: Springer-Verlag Berlin; 2011. p. 129-65.
- [77] Madhally SV, Matthew HWT. Porous chitosan scaffolds for tissue engineering. *Biomaterials*. 1999;20:1133-42.
- [78] Sudarshan NR, Hoover DG, Knorr D. Antibacterial action of chitosan. *Food Biotechnology*. 1992;6:257-72.
- [79] Ong SY, Wu J, Moochhala SM, Tan MH, Lu J. Development of a chitosan-based wound dressing with improved hemostatic and antimicrobial properties. *Biomaterials*. 2008;29:4323-32.
- [80] Huang XF, Sun YF, Nie JY, Lu WT, Yang L, Zhang ZL, et al. Using absorbable chitosan hemostatic sponges as a promising surgical dressing. *International Journal of Biological Macromolecules*. 2015;75:322-9.
- [81] Zhang YZ, Venugopal JR, El-Turki A, Ramakrishna S, Su B, Lim CT. Electrospun biomimetic nanocomposite nanofibers of hydroxyapatite/chitosan for bone tissue engineering. *Biomaterials*. 2008;29:4314-22.
- [82] Rhim JW. Physical and mechanical properties of water resistant sodium alginate films. *Lebensmittel-Wissenschaft Und-Technologie-Food Science and Technology*. 2004;37:323-30.
- [83] Pawar SN, Edgar KJ. Alginate derivatization: A review of chemistry, properties and applications. *Biomaterials*. 2012;33:3279-305.
- [84] Lee KY, Mooney DJ. Alginate: Properties and biomedical applications. *Progress in Polymer Science*. 2012;37:106-26.
- [85] Haug A, Larsen B, Smidsrod O. A study of constitution of alginic acid by partial acid hydrolysis. *Acta Chemica Scandinavica*. 1966;20:183.
- [86] Goh CH, Heng PWS, Chan LW. Alginates as a useful natural polymer for microencapsulation and therapeutic applications. *Carbohydrate Polymers*. 2012;88:1-12.
- [87] Donati I, Holtan S, Morch YA, Borgogna M, Dentini M, Skjak-Braek G. New hypothesis on the role of alternating sequences in calcium-alginate gels. *Biomacromolecules*. 2005;6:1031-40.

- [88] Morais DS, Rodrigues MA, Silva TI, Lopes MA, Santos M, Santos JD, et al. Development and characterization of novel alginate-based hydrogels as vehicles for bone substitutes. *Carbohydrate Polymers*. 2013;95:134-42.
- [89] Franklin MJ, Ohman DE. Identification of algf in the alginate biosynthetic gene-cluster of *Pseudomonas aeruginosa* which is required for alginate acetylation. *Journal of Bacteriology*. 1993;175:5057-65.
- [90] Liakos I, Rizzello L, Scurr DJ, Pompa PP, Bayer IS, Athanassiou A. All-natural composite wound dressing films of essential oils encapsulated in sodium alginate with antimicrobial properties. *International Journal of Pharmaceutics*. 2014;463:137-45.
- [91] Orive G, Ponce S, Hernandez RM, Gascon AR, Igartua M, Pedraz JL. Biocompatibility of microcapsules for cell immobilization elaborated with different type of alginates. *Biomaterials*. 2002;23:3825-31.
- [92] Caridade SG, Monge C, Gilde F, Boudou T, Mano JF, Picart C. Free-Standing Polyelectrolyte Membranes Made of Chitosan and Alginate. *Biomacromolecules*. 2013;14:1653-60.
- [93] Caridade SG, Monge C, Almodovar J, Guillot R, Lavaud J, Josserand V, et al. Myoconductive and osteoinductive free-standing polysaccharide membranes. *Acta Biomaterialia*. 2015;15:139-49.
- [94] Picart C, Caruso F, Voegel J-C, Decher G. *Layer-by-layer films for Biomedical Applications* Wiley-VCH; 2004. p. 592.
- [95] Larkin AL, Davis RM, Rajagopalan P. Biocompatible, Detachable, and Free-Standing Polyelectrolyte Multilayer Films. *Biomacromolecules*. 2010;11:2788-96.
- [96] Costa RR, Mano JF. Polyelectrolyte multilayered assemblies in biomedical technologies. *Chemical Society Reviews*. 2014;43:3453-79.
- [97] Iler RK. Multilayers of colloidal particles. *Journal of Colloid and Interface Science*. 1966;21:569.
- [98] Decher G, Lvov Y, Schmitt J. Proof of multilayer structural organization in self-assembled polycation polyanion molecular films. *Thin Solid Films*. 1994;244:772-7.
- [99] Decher G. Fuzzy nanoassemblies: Toward layered polymeric multicomposites. *Science*. 1997;277:1232-7.
- [100] Borges J, Mano JF. Molecular Interactions Driving the Layer-by-Layer Assembly of Multilayers. *Chemical Reviews*. 2014;114:8883-942.
- [101] Silva JM, Caridade SG, Oliveira NM, Reis RL, Mano JF. Chitosan-alginate multilayered films with gradients of physicochemical cues. *Journal of Materials Chemistry B*. 2015;3:4555-68.
- [102] Li XL, Zhang GY, Bai XD, Sun XM, Wang XR, Wang E, et al. Highly conducting graphene sheets and Langmuir-Blodgett films. *Nature Nanotechnology*. 2008;3:538-42.
- [103] Park JS, Cho SM, Kim WJ, Park J, Yoo PJ. Fabrication of Graphene Thin Films Based on Layer-by-Layer Self-Assembly of Functionalized Graphene Nanosheets. *ACS Applied Materials & Interfaces*. 2011;3:360-8.
- [104] Ariga K, Hill JP, Ji QM. Layer-by-layer assembly as a versatile bottom-up nanofabrication technique for exploratory research and realistic application. *Physical Chemistry Chemical Physics*. 2007;9:2319-40.
- [105] Li YY, Lu ZZ, Li ZJ, Nie GJ, Fang Y. Cellular uptake and distribution of graphene oxide coated with layer-by-layer assembled polyelectrolytes. *Journal of Nanoparticle Research*. 2014;16:14.
- [106] Wang LS, Lai AN, Lin CX, Zhang QG, Zhu AM, Liu QL. Orderly sandwich-shaped graphene oxide/Nafion composite membranes for direct methanol fuel cells. *Journal of Membrane Science*. 2015;492:58-66.

- [107] Yan N, Capezzuto F, Buonocore GG, Lavorgna M, Xia HS, Ambrosio L. Gas-Barrier Hybrid Coatings by the Assembly of Novel Poly(vinyl alcohol) and Reduced Graphene Oxide Layers through Cross-Linking with Zirconium Adducts. *Acs Applied Materials & Interfaces*. 2015;7:22678-85.
- [108] Kurapati R, Raichur AM. Graphene oxide based multilayer capsules with unique permeability properties: facile encapsulation of multiple drugs. *Chemical Communications*. 2012;48:6013-5.
- [109] Chen JT, Fu YJ, An QF, Lo SC, Huang SH, Hung WS, et al. Tuning nanostructure of graphene oxide/polyelectrolyte LbL assemblies by controlling pH of GO suspension to fabricate transparent and super gas barrier films. *Nanoscale*. 2013;5:9081-8.
- [110] Bao HM, Chen QW, Zhang LY, Chen G. Immobilization of trypsin in the layer-by-layer coating of graphene oxide and chitosan on in-channel glass fiber for microfluidic proteolysis. *Analyst*. 2011;136:5190-6.
- [111] Barsan MM, David M, Florescu M, Tugulea L, Brett CMA. A new self-assembled layer-by-layer glucose biosensor based on chitosan biopolymer entrapped enzyme with nitrogen doped graphene. *Bioelectrochemistry*. 2014;99:46-52.
- [112] Weng XX, Cao QX, Liang LX, Chen JR, You CP, Ruan YM, et al. Simultaneous determination of dopamine and uric acid using layer-by-layer graphene and chitosan assembled multilayer films. *Talanta*. 2013;117:359-65.
- [113] Shin SR, Aghaei-Ghareh-Bolagh B, Gao XG, Nikkhah M, Jung SM, Dolatshahi-Pirouz A, et al. Layer-by-Layer Assembly of 3D Tissue Constructs with Functionalized Graphene. *Advanced Functional Materials*. 2014;24:6136-44.
- [114] Yu DS, Dai LM. Self-Assembled Graphene/Carbon Nanotube Hybrid Films for Supercapacitors. *Journal of Physical Chemistry Letters*. 2010;1:467-70.
- [115] Wang XL, Bai H, Yao ZY, Liu AR, Shi GQ. Electrically conductive and mechanically strong biomimetic chitosan/reduced graphene oxide composite films. *Journal of Materials Chemistry*. 2010;20:9032-6.

CHAPTER 2. STATE OF THE ART

2. CHITOSAN NANOCOMPOSITES FOR BIOMEDICAL APPLICATIONS

Duarte Moura^{1,2}, João F. Mano^{1,2}, Maria C. Paiva³, Natália M. Alves^{1,2}.

¹ 3B's Research Group, Biomaterials, Biodegradables and Biomimetics, University of Minho, Headquarters of the European Institute of Excellence on Tissue Engineering and Regenerative Medicine, AvePark-Parque de Ciência e Tecnologia, 4805-017 Barco, Taipas, Guimarães, Portugal

² ICVS/3B's, Associate PT Government Laboratory, Braga/Guimarães, Portugal

³ Institute for Polymers and Composites/I3N, Department of Polymer Engineering, University of Minho, 4800-058 Guimarães, Portugal

Abstract

Chitosan (CHI), a biocompatible and biodegradable polysaccharide, with the ability to provide a non-protein matrix for tissue growth, is considered to be an ideal material in the biomedical field, due to the aforementioned characteristics and their environmental-friendly potential. However, the lack of good mechanical properties, limits its applications. In order to overcome this drawback, CHI has been combined with different polymers and fillers, leading to a variety of chitosan-based nanocomposites. The extensive research on CHI nanocomposites as well as their main biomedical applications are reviewed in this paper. An overview of the different fillers and assembly techniques available to produce CHI nanocomposites is presented. Finally, the properties of such nanocomposites are discussed with particular focus for bone regeneration, drug delivery, wound healing and biosensing applications.

Keywords: Chitosan; Polymer nanocomposites; Biomedical applications.

2.1 Introduction

The increasing need to develop green polymeric materials with improved thermal stability, gas barrier properties, strength and biodegradation, has led to the development of composite materials based on natural polymers [1].

Chitosan (CHI) is a linear semicrystalline polysaccharide, obtained by deacetylation of chitin and composed by N-acetyl D-glucosamine and D-glucosamine units, linked through β (1 \rightarrow 4) glycosidic bonds [2, 3]. Chitin or poly(β -(1 \rightarrow 4)-N-acetyl-D-glucosamine) is synthesized by living organisms and it is the structural component of the shells of crustaceans, cell walls of fungi and exoskeletons of insects [3-5]. Typically, shrimp and crab shell waste are the primary source for isolation and purification of this polysaccharide [3, 6-8]. When subjected to a deacetylation process, under alkaline conditions, part of the N-acetyl groups are lost and when at least 60% of the chitin units are D-glucosamine this polysaccharide is named chitosan [9, 10]. A soluble CHI is obtained after deacetylation, requiring 80-85% of free amino groups and acidic pH [5]. The free amino groups confer to CHI exceptional chemical and physical properties, among which are worth mentioning the positive charge in aqueous solutions at low pH [5]. At pH values above its $pK_a \approx 6.5$, the polymer loses the positive charge and precipitates which makes CHI a pH responsive material [5].

Moreover, CHI exhibits outstanding properties, such as biocompatibility and biodegradability [11], a lethal dose for 50% of test population (LD_{50}) of 16 g/Kg body weight [5], ability to be sterilized by any method without losing its properties [12], along with antibacterial, antifungal, mucoadhesive, analgesic and haemostatic properties [4, 13-16]. Besides, CHI has revealed to provide a non-protein matrix for tissue growth with potential to stimulate cell proliferation and tissue organization [13]. The chemical structure of CHI can be modified in order to improve the mentioned features, and also its solubility [2, 13]. Usually, these modifications are achieved by copolymerization, grafting the free amino groups or the C_3 and C_6 carbons in the CHI units with different types of moieties, including alkyl and carboxymethyl groups, resulting in different CHI derivatives [17, 18]. However, CHI still exhibits some limitations such as the lack of an appropriate biological response, partly caused by the weak mechanical properties for many applications (e.g. low stiffness) and high water content [19]. To overcome these problems, composites with polymers or fillers that can establish bonds with CHI have been produced [5]. The use of nanofillers is particularly interesting due to their high surface area, providing a large interface that, combined with high interfacial strength, will increase the load transfer capacity and greatly improve the

mechanical properties of the composite, eliminating the catastrophic failure caused by poor loading transfer [20, 21].

The interesting characteristics of CHI allied with the ability to be processed in different architectures and combined with different nanomaterials find a wide number of applications, including biomedical, such as wound healing, drug delivery, tissue regeneration and biosensing [13, 22]. Nanocomposites based on CHI are able to improve both structural and functional properties of this polysaccharide. In this review, an overview of the main types of CHI nanocomposite materials, their properties and processing strategies will be given. The biomedical applications of these nanocomposites will be discussed.

2.2 Chitosan Nanocomposites

Polymer nanocomposites are commonly defined as multiphase materials, where one of the phases exhibit at least one dimension smaller than 100 nm [23]. Typically, two essential key aspects are responsible for the successful development of nanocomposites:

- (1) High specific interfacial area;
- (2) Controlled stress transfer across the interface;

The first key factor is of major importance concerning the properties of nanocomposites. The large specific area of the nanoparticles provides a high surface-to-volume ratio, resulting in extensive binding between the polymer and the nanofiller. Achieving a strong interfacial bonding is then necessary in order to transfer the excellent nanoparticles' properties into the composite [24]. Thus, a strong interfacial bonding will allow the efficient stress transfer across the interface. This key aspect relates to the bonding energy at the interface, which may be improved through covalent bonding, electrostatic interactions, hydrogen bonding and van der Waals interactions [25]. In order to achieve the desired enhanced mechanical, electrical and optical properties, it is also important that a good nanofiller dispersion within the matrix is achieved, overcoming the aggregation tendency that is typical of nanoparticles that results in decreased interfacial area and poor mechanical properties [23, 24].

The interfacial strength plays a major role in the nanocomposites ultimate mechanical properties, including toughness, tensile strength and elastic modulus [26].

Among the different nanofillers used as reinforcement phase, the most used in the development of CHI nanocomposites were: (i) layered silicates, such as clay [27-29]; (ii)

metal/ceramic nanoparticles [30-32]; (iii) carbon nanotubes [33-35]; and more recently (iv) graphene based materials [36-38]. Next, each of these fillers will be analyzed.

2.2.1 Layered Silicates

Polymer-clay nanocomposites have been widely studied due to the improved material properties when compared to micro and macro composites [39]. Clays are hydrous silicates or alumino silicates with high aspect ratio and high intercalation chemistry. Typically, this nanofiller shows a layered structure which contains silicon, aluminum or magnesium, oxygen and hydroxyl with various associated cations [40].

In a more detailed analysis, the layers are built from tetrahedrally bonded silicon (Si) atoms surrounded by four oxygen atoms, and from octahedrally bonded aluminum (Al) or magnesium (Mg) surrounded by eight oxygen atoms, Figure 2.1 a) and b). These two sheets are bonded by sharing the oxygen atoms, leading to one layered structure of clay with 1 nm thick [41]. The structure and composition of clays can be classified according to the ratio of silica and alumina sheets: (i) kaolins (1:1 Type), which consists in one tetrahedral sheet and one octahedral sheet linked by hydrogen bonding between the hydroxyl groups, present in octahedral sheets, and the oxygen atoms present in tetrahedral sheets; (ii) smectites (2:1 Type), which results from the presence of one octahedral sheet between two tetrahedral sheets. In this conformation, the aluminium ions present in the octahedron sheets may be substituted by Fe^{2+} , Mg^{2+} or Li^+ , and the Si^{4+} , present in tetrahedral sheet by Al^{3+} , resulting in an overall negative charge; and (iii) layered silicate acids, where silicon tetrahedron sheets with different thickness are interlayered with alkali metal cations [40, 42, 43]. Clays are hydrophilic in nature and need to be modified for mixing with organic polymers, usually by treatment with ammonium or phosphonium ions, in order to increase the interlayer space between sheets and facilitate the diffusion of the polymer [43-45].

For the successful development of nanocomposites with layered silicates, it is important to ensure that the silicate structures are homogeneously dispersed into the polymeric matrix. Commonly, three different dispersion conformations can be obtained: (i) Tactoid structures, when the interlayer space of the clay does not expand, not allowing the intercalation of the polymer, which is not desirable [39]; (ii) Intercalated structures, when the layered clay structure is maintained but the interlayer distance increases, allowing penetration of the polymer; and (iii) Exfoliated structures, when the clay layers are well separated from each other, resulting in a good dispersion and mixing with the polymer phase, Figure 2.1 c) [46].

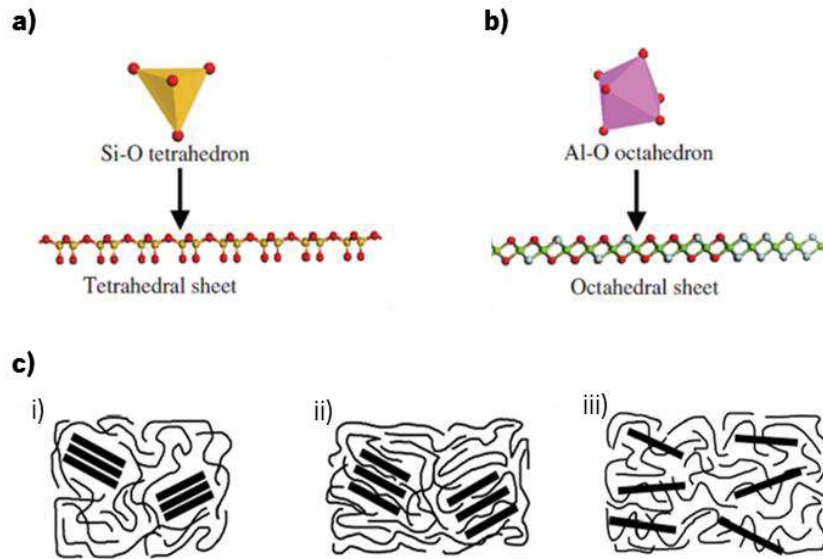


Figure 2.1 Representation of the basic units **(a)** Si-O tetrahedron and **(b)** Al-O octahedron present on the clay minerals [43]. **(c)** Representation of the different structures resulted from different clay dispersion in the polymeric matrix. (i) Tactoid structures, (ii) intercalated structures and (iii) exfoliated structures [39].

Montmorillonite (MMT) is an aluminosilicate belonging to smectites group, and is one of the most studied for nanocomposite applications [47, 48]. This layered silicate presents a negative charge of 0.67 per unit cell, which attributes to this material a weak acid behavior, and provides a strong capacity for hydration, swelling and dispersion. These characteristics provide MMT affinity to cations, and allow exfoliation of its layers, bonded by weak electrostatic and van der Waals interactions [43, 48].

Since the intercalation of MMT with CHI is feasible due to the electrostatic and hydrogen bond interaction established between the positive amino groups in CHI and the negative sites in MMT, and between amino groups and hydroxyl groups, respectively, these nanocomposites have been the focus of many studies [27-29, 49-51].

Lertsutthiwong *et al.* studied the influence of the CHI properties, such as molecular weight and deacetylation degree, on the properties of the CHI/MMT nanocomposites [49]. Using X-ray diffraction (XRD) analysis, the authors demonstrated that it was possible to intercalate CHI between the MMT layers, and that this effect was independently of the CHI molecular weight, since the diffraction peak of all nanocomposites moved to lower values [49]. Ennajih and coworkers demonstrated that the thermal properties of CHI/MMT nanocomposites were significantly improved when compared with the control CHI, showing a shift of the first decomposition peak from 230 to 255 °C for a MTT:CHI ratio of 80:20 wt% [50]. They also demonstrated that silicate layers were highly dispersed in the polymer, as XRD analysis demonstrated a shift of the angle to

lower values, revealing an interlayer increase from 1.21 nm to 1.5 nm when the ratio MMT:CHI used was 20:80 wt% [50]. Wang *et al.* explored the possibility to develop nacre-like structures by adding MMT to CHI films [51]. They have shown by scanning electron microscopy (SEM) analysis that CHI/MTT films were densely stacked forming a well-defined layered structure, similar to the brick-mortar structure of nacre, and were able to reach a higher elastic modulus (approximately 3 times higher) than pure CHI, showing a great ability of MMT to transfer load across the interface [51].

2.2.2 Metal/ceramic Nanoparticles

Nanoparticles (NPs) combined with polymer matrices lead to a whole new family of materials where the nanocomposites are expected to exhibit improved performances [52]. In fact, the incorporation of inorganic particles into the polymeric matrix is performed to achieve improved mechanical properties and, in some cases, to provide bioactivity to an inert material [53]. Usually three main groups of particles are identified as fillers for CHI nanocomposites: bioactive glass, bioactive ceramic nanoparticles and metal nanoparticles.

Bioactive glass (BG) represents a group of surface reactive materials with ability to bond to physiological structures, such as bone, and which are typically obtained by melt or sol-gel methods [54]. This type of NPs are essentially made of silicate with a variable composition of sodium, calcium and phosphorus. Due to their nanometric dimensions, these particles present a high specific surface area with ability to release ions and to provide a good substrate for protein adsorption [52, 55]. Sol-gel methodologies permit to produce nano-sized bioactive particles with controlled compositions [56-58]. Mota *et al.* produced CHI/BG NPs for periodontal defect applications and found that the introduction of BG NPs resulted in increased stiffness of the membrane, reaching an elastic modulus of 4.7 ± 0.3 MPa. However, a decrease on the ultimate tensile strength from 6.3 ± 0.8 MPa down to 3.3 ± 0.6 MPa was observed [59]. Moreover, upon immersion in SBF the nanocomposite membranes were able to promote the deposition of an apatite layer, evidencing an osteoconductive potential [59]. Seuss *et al.* explored the use of BG and BG NPs with CHI to produce nanocomposite coatings [60]. They also found that a hydroxyapatite (HA) layer was formed on all coatings after 21 days, however, a difference between microsized and nanosized composite coatings was found, since the BG NPs showed higher HA forming ability. The bactericidal effects of these coatings were studied against *Escherichia coli* (E. coli) and it was found that both composite coatings showed antibacterial activity [60].

Similarly to the previous fillers mentioned, ceramic NPs are used to form nanocomposites, providing enhanced mechanical properties and improving the interaction with surrounding tissues [55]. In particular, hydroxyapatite nanoparticles (HA NPs) have shown potential for nanocomposites fabrication, showing good osteoconductivity, osteoinductivity, biodegradability and high mechanical strength [61]. However, the brittle character of these materials is detrimental for the composite properties when the ceramic nanoparticles are incorporated at high concentrations [62]. Lee *et al.* developed CHI scaffolds with micro and nano HA and tested their potential to be used as bone graft substitutes in an *in vivo* model [63]. They found that the scaffolds were not cytotoxic for mouse osteoblastic cell line MC3T3-E1, and showed through microcomputer tomography, that the rabbit tibia showed cortical bone formation independently of the HA size, although reaching higher levels for HA NPs [63]. Li and co-workers studied the properties of CHI/HA NPs cross-linked with genipin [64]. They found that the mechanical properties, in particular the tensile strength, were highly dependent of the concentration of the HA NPs used, exhibiting an increase from 36.45 ± 5.34 MPa to 73.50 ± 7.67 MPa when the NPs concentration increased up to 10 wt%. At higher HA NPs concentrations a decrease of the tensile strength was observed. The *in vitro* cytotoxicity assays showed that the crosslinking composite membranes were non-cytotoxicity against fibroblasts cell line L929, after 24 h of incubation [64].

Metal NPs combined with polymers are known for provide antibacterial [65] and biosensing [66] characteristics. In fact, nearly all metals were already reported to be used for nanoparticles production, including: silver [66, 67], gold [66, 68] and zinc oxide [69] nanoparticles, among others [70-72]. Potara *et al.* used CHI/silver nanoparticles (Ag NPs) and found that both components act synergistically against two strains of Gram-positive *Staphylococcus aureus* (*S. aureus*), showing a decrease in the minimal inhibitory concentrations (MIC) when compared with Ag NPs and CHI individually [67]. Du *et al.* investigated the use of gold nanoparticles (Au NPs) together with a CHI matrix for glucose biosensing applications [68]. They found that the film characteristics could be adjusted by controlling the deposition conditions of the CHI and Ag NPs and achieved a biosensor with a detection limit of about 13 μ M [68]. Li and co-workers produced CHI/zinc oxide nanoparticles (ZnO NPs) membranes, identifying an antibacterial activity against *Bacillus subtilis*, *E. coli* and Gram-positive bacteria *S. aureus* for a ZnO NPs concentration of 6–10 wt % [69]. They demonstrated that for 6 wt% of ZnO NPs enhanced mechanical properties were achieved, reaching an improvement of $\approx 24\%$ in tensile strength [69].

Independently of the NPs type, several parameters may be controlled in order to tune the composites properties, including: particle size, chemical composition, crystallinity and shape [73].

2.2.3 Carbon Nanotubes (CNTs)

Carbon nanotubes (CNTs) were first identified by Iijima in 1991 [74], and may be described as hexagonal sp^2 carbon structures rolled up in a tube [75]. These seamless cylinders may present open or closed ends, the latter being capped by hemi-fullerenes structures [76]. Two types of CNTs may be identified: (i) single-walled carbon nanotubes (SWNTs); and (ii) multi-walled carbon nanotubes (MWNTs) [77]. The first type consists on a single graphene sheet rolled up in a cylinder, presenting a diameter of approximately 1 nm and a length that may reach the centimeters range, while the MWNTs are composed by multiple concentric cylindrical sheets of graphene, held together by van der Waals forces, with an interlayer space of approximately 0.35 nm [78]. The diameter of the MWNTs may range from 5-20 nm depending on the number of layers, although it may reach 100 nm [77, 79]. The nanotubes with double-walled structure (DWNTs) have revealed interesting properties such as higher flexural modulus than SWNTs and higher toughness than MWNTs [80].

CNTs exhibit a high elastic modulus, reaching 1 TPa (the elastic modulus of diamond is 1.2 TPa), a tensile strength of 63 GPa [81], and a density of 1.74 g/cm^3 . Under ideal conditions, in the absence of defects of the carbon lattice, CNTs are able to achieve a ballistic electron transport [82], due to the absence of scattering which reduces the heat loss and allows to carry large current densities [83]. A room temperature thermal conductivity up to 6000 W/m.K has been reported, which is twice as high as that of diamond [82, 84-86].

These remarkable properties may vary according to several factors, such as the presence of defects in the atomic arrangement, the diameter and length of the CNTs, the synthetic process used and impurities present in the structure [76]. One of the most influential features for SWNTs properties is their atomic arrangement relative to the nanotube axis. This is described in terms of the tube chirality, defined by the chiral angle. The SWNTs may present different conformations, namely the zig-zag (chiral angle= 0°) and the armchair conformation (chiral angle= 30°). Depending on the conformation, the carbon nanotubes may be classified as metallic, semi-metallic or semi-conducting [77, 87, 88, 89].

The excellent properties of CNTs make them attractive for composite applications. However, for biomedical applications the elimination of metallic impurities is often required, and CNTs

dispersion in the polymer matrix should also be achieved in order to attain good composite properties [91]. CNTs grow entangled and form stable agglomerates, increasing the difficulty of dispersion in polymer matrices. New fabrication methods have been studied to achieve composites with well dispersed CNTs, such as the use of ultrasounds in solution blending [76]. Gupta *et al.* were able to develop CHI/aligned MWNTs for neural tissue regeneration using an electrical field alignment technique [33]. The obtained scaffolds presented an increase of about 35.7% in Young modulus when MWNTs were added to CHI, reaching 1694 ± 70.6 MPa. Electrical conductivity measurements showed an increase in the order of 10^5 S/m with the addition of MWNTs [33]. Hwang *et al.* reported the coating of CHI on the CNTs surface, reporting that for 50 wt% CHI/CNTs a tensile strength of 51 MPa was reached, as well as a low resistivity in order of $16 \Omega/\text{sq}$ [92]. Although the previous works have demonstrated that the addition of carbon based materials to polymeric matrix resulted in enhanced polymeric properties, in fact, the need to improve the interaction polymer/carbon material to truly take advantage of the carbon materials properties should be further explored by defects induction, covalent and non-covalent functionalization of CNTs [93].

2.2.4 Graphene based Materials

Graphene consists on a layer of sp^2 hybridized carbon atoms forming a hexagonal structure, and it is considered the building block of all sp^2 hybridized carbon allotropes [26]. This carbon material presents a honeycomb like-structure, with a bond length between the carbon atoms of 0.142 nm [94] and it is known as the thinnest 2D material, with a van der Waals thickness of 0.34 nm [24]. Graphene has outstanding properties such as high elastic modulus (≈ 1 TPa), the highest known intrinsic electrical conductivity of 6×10^5 S.m⁻¹ and a high thermal conductivity of 5.1×10^3 W.m⁻¹.K⁻¹ [95-97]. Moreover it shows a large theoretical specific area of $2630 \text{ m}^2\text{g}^{-1}$, an optical transmittance of 97.7% and a high flexibility [98, 99].

Due to its intrinsic properties and to the possibility of achieving thermally and electrically conductive nanocomposites, graphene has aroused interest from the scientific community [100-102]. Its interfacial bonding with polymer matrices remains a challenge due its surface chemical inertia [23, 26]. Individual graphene layers may be formed on metal surfaces, however for the production of bulk graphene the methods based on graphite exfoliation are preferred. The extensive exfoliation of graphite into graphene is a topic of intense research, and quite difficult to attain. It

has been achieved by chemical oxidation of graphene layers in graphite, with the advantage of inducing reactivity to this material, at the expense of the electrical conductivity. In fact the graphene oxide (GO) formed presents hydroxyl and epoxy groups on both sides of the graphene plane, and carbonyl or carboxyl distributed along the edges, as represented in Figure 2.2 [103].

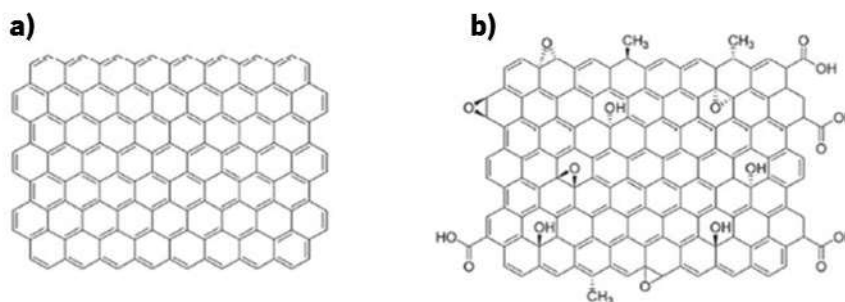


Figure 2.2 Schematic representation of **(a)** graphene and **(b)** graphene oxide sheet [90].

The presence of oxygen-containing functional groups render GO a biocompatible and physiologically soluble behavior, and allow stronger interactions with many polymers [104]. The major drawback that comes from the oxidation of graphene is the loss of the electrical conductivity [23]. However this property may be partially restored through a chemical reduction of GO, using highly reducing reagents such as hydrazine monohydrate [105, 106].

He *et al.* studied the influence of GO on the thermal stability and mechanical properties of CHI films, reporting a good dispersion of GO [36] and observing an increase in the glass transition temperature from 186.6 °C to 192.5 °C. For a filler concentration of 0.5 wt% the storage modulus was maximized and a nacre-like structure was obtained, an organization widely explored in the development of tough biomimetic nanocomposites [107]. The significant enhancement in the mechanical properties were interpreted as an effective attachment of CHI to the GO sheets [36]. Fan *et al.* also focused on the mechanical properties, although using graphene in its pristine form [108]. Experimental data revealed that the addition of small amounts of graphene (0.1-0.3 wt%) significantly increased the elastic modulus over 200% [108]. In another study, a new nanocomposite was developed forming GO/CHI fibers and the adsorption of fuchsin acid dye by these fibers was analyzed [37]. The GO/CHI fibers revealed that the initial pH of the solution was an important factors that affected the adsorption capacity of fuchsin acid dye onto the fibers [37]. Li *et al.* developed GO genipin cross-linked CHI films through solvent casting, proving a reinforcement of the native films with a tensile strength increase and a resistance to enzymatic

degradation [109]. It was also demonstrated that the incorporation of GO was non-toxic, probably due to its hydrophilic and biocompatible nature [109]. The mechanical behavior of the nanocomposites films in the wet state was also evaluated, revealing that the presence of an aqueous medium increased the tensile strength (3 times higher than in dry state), an important result when considering potential biomedical applications [38].

2.3 Materials Processing Strategies for Chitosan Nanocomposites

The main techniques that have been used to produce CHI nanocomposites, namely solvent casting, freeze drying, layer-by-layer, and electrospinning are described in this section.

2.3.1 Solvent Casting

Solvent casting is one of the most common techniques for preparation of CHI nanocomposites films and membranes [53, 110]. Typically, the polymer is dissolved in a solvent and then cast onto a surface, such as glass Petri dishes. The solvent is subsequently allowed to evaporate at room temperature or in air oven, and after that, the films/membranes are detached from the cast form (Figure 2.3 a) [111]. This method is a simple approach to fabricate CHI nanocomposites, with the possibility to incorporate drugs or chemicals within the structures, with no need of expensive manufacturing equipments and high processing temperatures [112, 113]. However, it still exhibits drawbacks, namely: the possible retention of residual solvents, which may cause toxicity effects, becoming harmful to transplanted cells or host tissues [114]; only simple shapes can be formed; and usually the structures present very low pore interconnectivity, unsuitable for some tissue engineering applications [112].

Several studies concerning nanocomposites of CHI obtained by solvent casting can be found in literature [115-117]. Kithva *et al.* studied the formaldehyde influence on CHI–HA nanostructured composite films, including in their mechanical properties [116]. These authors have shown that the formaldehyde presence strongly affects the interaction between CHI and HA, leading to a significant increase of the Young's modulus (E) and ultimate tensile strength (UTS) as high as 17.3 GPa and 222 MPa, respectively, for films containing 66 wt.% HA [116].

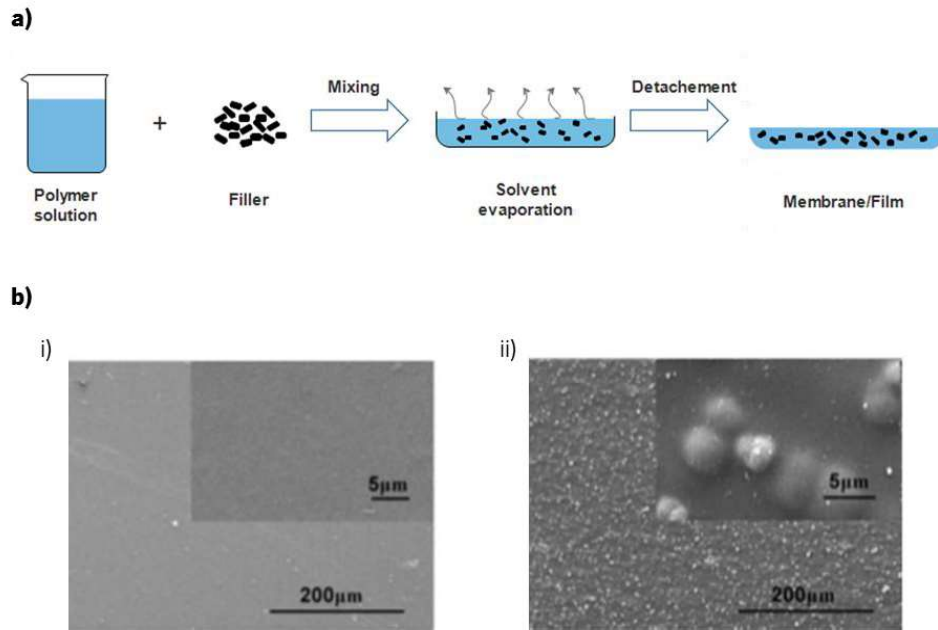


Figure 2.3 (a) Schematic representation of the procedure to obtain a membrane/film using the solvent casting method **(b)** Comparison between the surface of a (i) CHI membrane and (ii) CHI/bioactive glass membrane [115], both obtained by solvent casting.

The bioactivity and viscoelasticity of CHI/Bioglass® solvent casting membranes was investigated by Caridade *et al.*, Figure 2.3 b) [115]. The data showed that after 1 day immersion in SBF, apatite structures had already been developed which completely covered the samples after 5 days and exhibiting typical cauliflower structures after 7 days. The study of the viscoelasticity of the membranes by dynamic mechanical analysis (DMA) revealed that storage modulus (E') presented a continuous decrease that tended to approach to the E' values of the pure CHI membranes. This loss of stiffness was an indication that the BG particles were being dissolved from the membranes [115]. He and co-workers, exploring the same production methodology, fabricated reduced graphene oxide (rGO)/CHI composite films cross-linked with genipin [117]. They found that the addition of rGO increased the tensile strength of the films up to 72.5 MPa and also increased the thermal stability of those for an amount of 0.7% [117].

2.3.2 Freeze Drying

This method is one of the most widely used for the preparation of highly porous scaffolds by inducing thermally phase separation. Commonly, the solution temperature is lowered until the solid-liquid demixing occurs, forming two different phases: frozen solvent and polymer phase. Then, the frozen solvent, through sublimation, leaves the polymeric structure forming a pore. The resultant structure can be controlled by varying the type of polymer and its concentration [118].

Anisha *et al.* using freeze drying process, were able to develop antimicrobial sponges composed of CHI, hyaluronic acid and Ag NPs as a wound dressing with drug resistant bacteria [119]. The homogenous mixing of CHI, hyaluronic acid and Ag NPs followed by freeze drying resulted into a flexible and porous structure with ideal wound dressing swelling, biodegradation and haemostatic potential [119]. Mohandes *et al.* using also the same processing methodology were able to synthesize a composite of CHI, GO and HA NPs, and studied its bioactivity, revealing a higher Ca and P ions release, after 14 days, than HA by itself [120]. CHI-gelatin/MMT-HA scaffolds were prepared through freeze drying showing a nanoscale architecture with well-interconnected pores, with a mean pore size of 250 μm , similar to natural bone [121]. Sun and coworkers synthesized multilayered CHI/CNTs nanocomposite films, through freeze drying and solvent casting, and found that the tensile stress and ductility of solvent casted films are higher than by freeze drying, probably due to the porosity [122].

2.3.3 Layer-by-layer (LbL)

Layer-by-Layer (LbL) assembling, proposed by Iler in 1996 [123] and popularized by Decher [124], is a method capable of modifying surfaces and fabricating highly ordered polymeric films and nanocomposites over different types of substrates [125]. This simple, reproducible and flexible method is based on the sequential adsorption of different macromolecular components, which are attracted to each other due to electrostatic interactions, hydrogen bonding, van der Waals forces, and electron exchange, among others [125, 126]. Different LbL approaches can be used to build up a multilayer film, including dip coating, spin coating and spraying coating (Figure 2.4 a)) [127]. Figure 2.4 b) shows a FS multilayered membrane obtained by dip coating and where it is possible to visualize a robust and layered membrane.

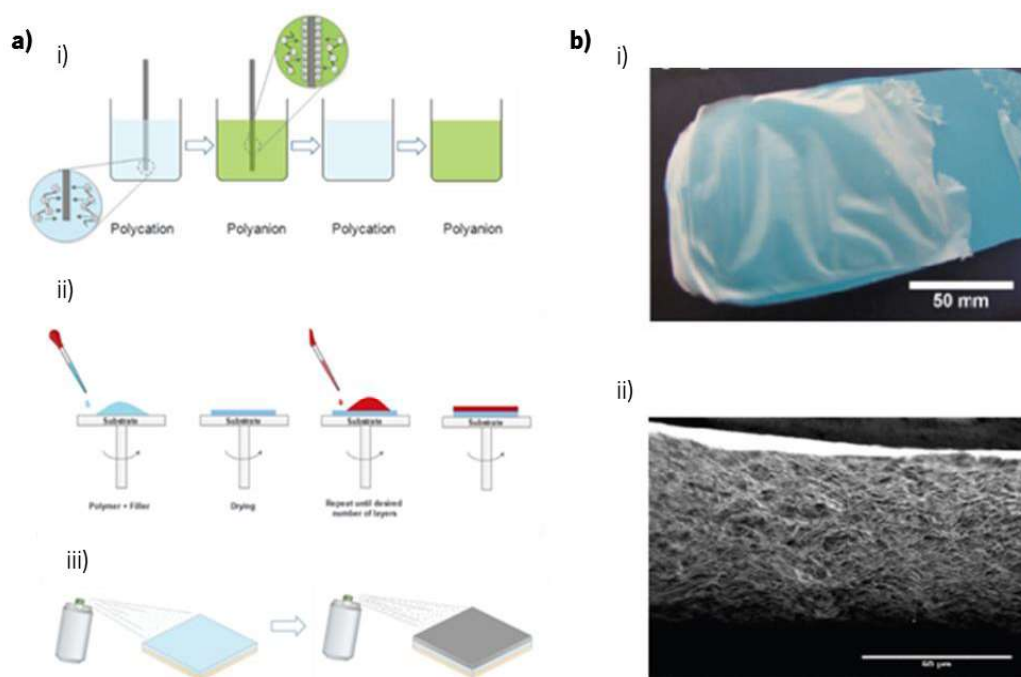


Figure 2.4 Representation of (a) three main LbL methods: (i) dip coating; (ii) spin coating and (iii) spray coating; and (b) Image of a chitosan/alginate free-standing membrane, where (i) represents the membrane obtained by dip coating a polypropylene substrate after 100 cycles and (ii) its respective cross-section SEM picture [128].

Due to its versatility and great availability of building blocks (e.g., CNTs, clays, NPs, polymers), this technology allows to fabricate multilayered devices of any nature, size, shape, and chemical composition, assuring the development of nanostructures with desired geometries and functionalities (Figure 2.5) [129]. Besides, the properties of multilayered devices can be tuned through solution pH, temperature, or ionic strength [126].

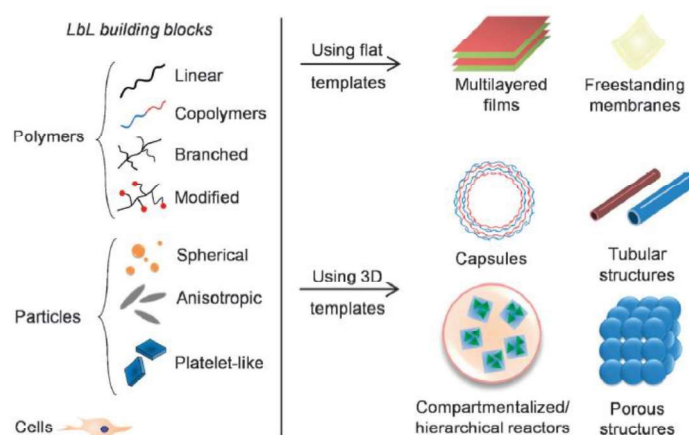


Figure 2.5 Schematic illustration of the different structures resulted from the different building blocks and substrates used in the LbL process [129].

Yang *et al.* used the LbL assembly approach to fabricate BG NPs/CHI/alginate (ALG) scaffolds [130]. The bioactive glass scaffolds were immersed in each biopolymer and the results showed that as the CHI and ALG were infiltrated in the porous scaffold, a decline in the porosity was achieved, reaching 1.8% less at the end of three cycles. This continuous assembling between the BG scaffold and both biopolymers also resulted in an increase of the mechanical properties, achieving an elastic modulus of 80 MPa and a compressive modulus 4 times higher than the BG scaffolds [130]. Pavinatto and coworkers assembled CHI/MWNTs films, built on a fluorine doped tin oxide electrode, to study the detection of 17 α -ethinylestrol [131]. They found a faster electron transfer kinetics and good detection limit of 0.09 $\mu\text{mol/L}$ [131]. Couto *et al.* study the development of LbL coatings using CHI and BG NPs in order to mimic the organic-inorganic structure of nacre [132]. These authors using quartz crystal microbalance showed that this methodology may be used to produce tunable and viscoelastic nanostructured multilayers upon increasing the number of LbL cycles. Moreover, it was shown that after 14 days of immersion in SBF, apatite-like layers distributed over the entire composite surface were achieved exhibiting cauliflower morphology. XRD tests also confirmed crystalline structure of the calcium phosphate layer [132].

2.3.4 Electrospinning

Electrospinning (ES) represents a suitable technique to produce fibers, with diameters in the nm- μm length scale, since it allows controlling morphology, porosity and composition using relatively unsophisticated equipment. Typically, the ES process uses an electric field created between the polymer solution and the collector, which generates internal repulsive forces in the polymer solution and, at a critical point, causes the expulsion of the polymer solution in shape of fibers towards the collector [133, 134]. Three different alternatives of electrospinning can be found, namely: wet-dry electrospinning, wet-wet electrospinning and co-axial electrospinning, Figure 2.6 [110]. The major difference between the first two methods is that the wet-dry method uses a volatile solvent which evaporates as the fibers are spun through the collector, while the wet-wet method spun a non-volatile solvent to a collector with a second solvent. Regarding the last method, it is possible to obtain fibers with a core-sheath structure, once two different components can be spun at the same time [110].

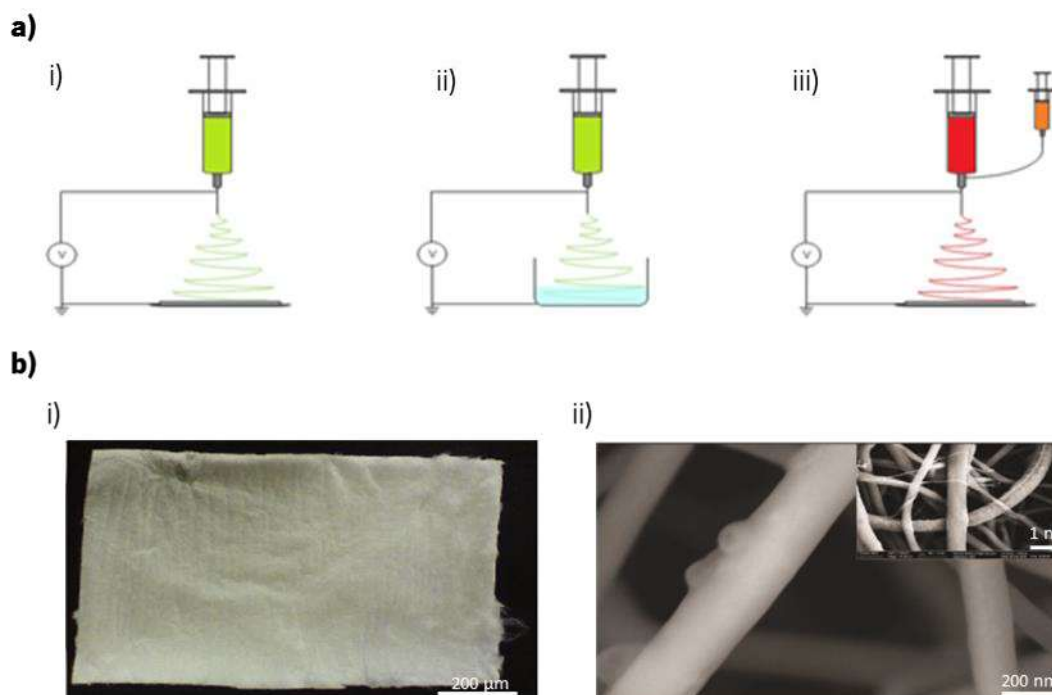


Figure 2.6 (a) Representation of the different electrospinning approaches, namely (i) wet-dry spinning, (ii) wet-wet spinning and (iii) co-axial electrospinning. **(b)** Representation of a (i) macroscopic electrospun chitosan fibermat and (ii) chitosan/hydroxyapatite nanoparticles fibers morphology obtained by SEM with respective insert image at lower magnification [135].

This cost effective and easy-to-manufacture technique has been widely studied for nanocomposites production, including for wound dressings, medical implants and scaffolds, Figure 2.6 b) [111, 136]. For the particular case of soluble polysaccharides such as CHI, the wet-dry methodology is the most used. Bai *et al.* explored the development of electrospun CHI nanofibers functionalized with a quaternary amine, N-[(2-hydroxy-3-trimethylammonium) propyl] chitosan chloride (HTCC), to adsorb and reduce virus presence [137]. Due to the difficulty for electrospinning HTCC alone, these authors used graphene as additive, founding that the good interaction between the graphene and the highly charged trimethyl amine group on the HTCC allowed a 95% reduction of porcine parvovirus due to the higher amount of HTCC that was able to reach the collector [137]. Najafabadi *et al.* studied the ability of CHI and GO to absorb metal ions such as Cu^{2+} , Pb^{2+} , and Cr^{2+} , showing that the obtained nanocomposites were able to absorb such ions, but with a decreasing capacity when pH values were above 6 [138]. Moreover, the adsorbent could be used up to 5 times without losing its initial adsorption capacity [138]. Another example of ES using for nanocomposites development, comes from the work done by Lee *et al.* [139]. These authors, using Ag NPs together with CHI, were able to obtain homogenous nanofibers structures with a high degree effectiveness against bacterial growth, particularly for Ag NPs amount of 2 wt% [139]. Mahdih and coworkers electrospun CHI and MWNTs, obtaining nanofibers

nanocomposites with a conductivity of $9 \times 10^{-5} \text{ S.cm}^{-1}$, showing great potential to be used in biomedical applications [140].

2.4 Biomedical Applications

The composition, architecture, and mechanical properties of nanocomposites are important to engineer implants that can balance the degradation with remodeling of regenerated tissue [52, 144]. In fact, the development of biomimetic nanocomposites with different inorganic nanofillers, incorporated within polymeric materials, has been extensively studied [145, 146]. Natural and synthetic polymeric nanocomposites represent powerful technologies for biomedical applications, namely for tissue regeneration and controlled drug delivery [147, 148]. Several materials have been found to be suitable for biomimetic nanocomposites [17,149]. Herein, the major biomedical applications where CHI nanocomposites can be applied are described as well as a brief overview of the main works done under this scope in the last 5 years. Table 2.1, gives a brief overlook of the works concerning CHI nanocomposites for biomedical applications, being some of them next analyzed.

Table 2.1. Chitosan based nanocomposites for different biomedical applications.

Application	Composition	Processing Technique	Shape	Reference
Biosensing	CHI/DNA/MWNTs	Spin coating	Film	[155]
Biosensing	CHI/GO bond to 5'amine single strand DNA	Spin coating	Film	[156]
Biosensing	CHI/Au NPs/haemoglobin	Dip coating	Membrane	[157]
Biosensing	CHI/Au NPs linked to cytochrome c and glucose oxidase	Electrodeposition	Film	[158]
Bone Regeneration	CHI/HA NPs loaded with icariin	Solvent casting	3D Scaffold	[159]
Bone Regeneration	CHI/HA NPs/ collagen	Freeze drying	3D Scaffold	[160]
Bone Regeneration	CHI/HA NPs/SWNTs	Freeze drying	3D Scaffold	[161]
Bone Regeneration	CHI/BG NPs	Freeze drying	3D Scaffold	[162]
Bone Regeneration	CHI/GO	Freeze drying	3D Scaffold	[163]
Drug Delivery	CHI/layered silicate loaded with doxorubicin	Freeze drying	3D Scaffold	[164]
Drug Delivery	ALG/CHI/ HA NPs loaded with doxorubicin	Solvent casting	Hydrogel	[165]
Drug Delivery	CHI/GO loaded with fluorescein sodium	Solvent casting	Membrane	[166]
Drug Delivery	CHI/MMT loaded with oxytetracycline	Freeze drying	Scaffold	[167]
Tissue Engineering	CHI/CNTs	Freeze drying	3D Scaffold	[168]
Tissue Engineering	CHI/graphene	Solvent casting	Hydrogels	[169]
Tissue Engineering	CHI/HA NPs	Electrospinning	Membrane	[170, 171]
Tissue Engineering	CHI/CNTs	Solvent casting	Hydrogel	[173]
Tissue Engineering	CHI/carbon nanofibers	Freeze drying	3D Scaffold	[174]
Tissue Engineering	CHI/TiO ₂ NPs	Solvent casting	Membrane	[175]
Wound healing	CHI/poly(ethylene glycol)/ZnO/Ag NPs	Solvent casting	Film	[176]
Wound healing	CHI/PVA/graphene	Electrospinning	Membrane	[177]
Wound healing	CHI/MMT loaded with silver sulfadiazine	Solvent casting	Membrane	[178]
Wound healing	CHI/AG NPs	Solvent casting	Membrane	[179]
Wound healing	CHI/AG-MMT	Solvent casting	Film	[180]
Wound healing	CHI/reduced GO	Solvent casting	Film	[181]

2.4.1 Bone Tissue Engineering

Bone is a mineralized connective tissue formed by osteoblasts [150]. The fundamental subunit of bone structure is mineralized collagen fibril that consists of self-assembled triple helices of collagen, carbonated apatite and water molecules [151, 152]. These collagen fibrils are assembled into lamellar structures which are organized into concentric lamellae that compose the osteons of the Haversian canal system. Although not yet understood how the mineralization is triggered, HA nanocrystals tend to grow on these assembled fibrils, with their crystallographic axes aligned with the fibril long axes [151]. From the anatomical point of view, two different regions may be identified in bone: a dense shell of cortical bone that supports and protects; and a porous and cancellous bone at both ends, which is responsible for optimizing weight transfer and minimize the friction at the joints [144]. Cortical bone is made of repeating osteon units, while cancellous bone is an interconnecting framework of trabeculae with bone marrow free spaces. Similarly with the osteon units, also the trabeculae is made of collagen fibers [144].

When exposed to a damage, different types of bone grafts can be used, such as: autografts, allografts and synthetic bone grafts [182]. The first methodology is considered the gold standard for bone repair, however it exhibits significant disadvantages such as: limited availability, donor site morbidity and risk of disease transfer from donor to recipient [183]. In turn, allografts as alternative also show some risks as lack of osteoinduction and osteoconduction, risk of disease transmission and insufficient mechanical properties. Thus the development of synthetic bone grafts where these drawbacks are overcome represents a tremendous need for bone repair [184], in particular through the use of biomimetic devices exhibiting osteoconductive properties [151].

Im *et al.* developed a 3D porous CHI scaffold, through freeze drying technique, with different amounts of nHA and SWNTs, to induce the growth of human osteoblasts [161]. When compared with conventional CHI scaffolds, the introduction of nHA (20 wt%) and SWNTs (1 wt%) allowed a significant enhancement of the tensile and compressive moduli. Cellular assays performed to test the cell adhesion, demonstrated that the introduction of nHA plays an important role in scaffolds cytocompatibility, once the osteoblast adhesion increased 59%. Moreover, when SWNTs were added, a great improvement in cell adhesion was observed. This increase suggests that the addition of SWNTs to nHA/CHI scaffold may have a synergistic effect, improving their cytocompatibility properties [161]. Correia *et al.* studied the combination of CHI with BG nanoparticles, in order to produce scaffolds, obtained by freeze-drying, with hydration induced shape memory and

biomineralization ability [162]. The osteoconductive character of the developed scaffolds was achieved, once SEM images depicted an apatite layer and cauliflower like-structures, with almost total surface covered after 7 days. Concerning the shape memory ability, the nanocomposite scaffolds revealed better shape memory than pure CHI, showing a shape recovery of 89.9%, after a 30% strain applied [162]. Liu *et al.* studied the potential use of electrospun nHA/CHI fibers seeded with bone marrow mesenchymal stem cells (BMSCs) for bone regeneration [171]. These authors found that after 7 days BMSCs exhibited a spindle morphology on nHA/CHI, while spherical shape on CHI, revealing an important effect of HA on supporting cells spreading. Polymerase chain reaction test of mRNA for integrin subunits were notably up-regulated with cells cultured on nHA/CHI compared to CHI after 14 days, highlighting the great potential of using the HA/CHI nanocomposite nanofibers for bone tissue engineering applications [171]. Depan and coworkers investigated the biological response of osteoblasts cells on CHI/GO scaffolds as well as the mechanical properties of the produced nanocomposite material [163]. According to this work, an increase of 44% in the elastic modulus was verified and an enhancement in the cell attachment, proliferation and growth was achieved [163].

2.4.2 Drug Delivery

The increasing limitation of standard drugs caused by nonspecific cell targeting and tissue biodistribution, allied with the rapid metabolism and excretion of those, resulted in a great demand for systems with optimized performance [185, 186]. Nanocarriers have emerged as one of the most potential drug delivery devices once they are able to interact with the cell membranes and enter into the cells by endocytosis, escaping to endosomal compartment, releasing the drug in cytosolic compartments [187]. As main requisites to build-up these systems are the biodegradability and biocompatibility, which typically are provided by natural polymers such as CHI [188, 189].

Justin R. and Chen B. studied the potential application of GO/CHI nanocomposites, obtained by solvent casting, for drug delivery systems, namely for transdermal drug delivery [190]. In order to do that, these authors investigated the optimal amount of GO that should be used to provide both a good mechanical performance and a good release profile of the drug (Fluorescein Sodium). It was found that an amount of 2 wt% showed the best conditions, allowing an increasing in the Young's modulus from 1 to 1.3 GPa, and at the same time an enhancement in the tensile strength and elongation at break. Concerning the drug release, it was shown that this phenomenon

was dependent of the loading ratio of the drug to GO and from the pH of the medium. These authors found that the optimal loading ratio was 45.6% allowing a 72% releasing increase and in a shorter time than CHI [190]. When tested in acidic conditions the release decreased, showing the great potential of these nanocomposites for a selective release [190]. Salcedo *et al.* explored the ability of CHI/MMT nanocomposites to delivery oxytetracycline via oral route [167]. The *in vitro* and oxytetracycline absorption was explored with CaCo-2 cell line and it was shown that the concentrations of nanocomposites with higher average values of cell viability was achieved for a CHI/MMT of 0.25 mg/ml and for oxytetracycline 0.0375 mg/ml amount. Confocal laser scanning microscopy (CLSM) evaluation revealed that the nanocomposite particles are into the depth of the cell substrate, in contact to cell nuclei, indicating an actual internalization and not only a membrane interaction or a deposition of the particles on cell substrate [167]. Recently, Mo *et al.* combined doxorubicin (DOX), an anticancer drug, with hyaluran/CHI/SWNTs [191]. They explored the use of SWNTs as vehicles for DOX, CHI to enhance water solubility and pH sensibility and in particular hyaluran was used once it constitutes a ligand of CD44 receptor, which are overexpressed in cancer cells. The SWNT/CHI/hyaluran/DOX presented lower toxicity to fibroblasts (representative of normal cells) than for HeLa cells (cancer cells representatives). The DOX release showed a high rate when exposed to a pH=5.5 reaching a total release of 85%, when compared with the medium at pH=7.4, showing a selective delivery system mechanism [191].

2.4.3 Soft Tissue Applications

Apart from the last two applications, CHI nanocomposites have also been investigated for soft tissue applications. Wound healing properties of nanocomposites are among the most researched properties for biomedical applications. Wound healing is a dynamic process consisting of four overlapping, and programmed phases, namely: homoeostasis, inflammation, proliferation and tissue remodeling [192, 193]. The microenvironment of the wound healing process is complex and involves the interaction of a large number of different types of cells and molecules [194]. To achieve and promote a better healing process, wound dressings play an important role and should include some essential features, such as: biocompatibility; ability to prevent bleeding and dehydration of the wound; ability to keep a favorable moist environment; protection of the wound against external contamination; permeability to gas and fluid exchanges; ability to absorb exudates from the wound area; thermal isolation; non-toxicity and non-allergenic profile [195, 196]. Hydrogels based on pure CHI with high toughness may be obtained using, for example, double-

network strategies [197]; however, the use of nanocomposites based on CHI matrices are much more usual. Considering these features, Lu *et al.* reported the use of CHI-PVA/graphene nanofibers, produced by ES, for wound healing applications [177]. These authors tested the potential of these membranes on mice and rabbits skin wounds and found that after 5 days, the wound area significantly decreased and at the end of 10 days the skin was completely recovered, while for membranes without graphene, these wound areas still exist [177]. Aguzzi and coworkers explored the use of CHI/MMT nanocomposites loaded with silver sulfadiazine for wound healing purposes [178]. Here, they demonstrated a successful loading of the silver sulfadiazine in the nanocomposites structure, once XRD tests have shown no free drug in the composite matrix, revealing that the intercalated nanocomposites were formed by insertion of drug and/or polymer molecules, with a homogeneous dispersion in the nanocomposite structures [178].

Associated with wound healing process, there is an important property of materials that can also accelerate and benefit the recovery of a tissue, which are the antimicrobial properties. Usually, microbes are able to multiply faster and hinder wound healing, and thus the inhibition of these microorganisms results in better wound dressing materials [177]. Campos *et al.* produced CHI/Ag NPs films with antimicrobial activity, using solvent casting, and studied their effect on Gram-positive and Gram-negative bacteria [179]. It was found that the highest antibacterial activity occurred for films with 3 wt% of Ag NPs, and above this concentration, the bactericidal effect tends to decrease. Moreover, these authors found that the presence of Ag NPs in the CHI polymeric matrix led to appearance of silver ions on the nanocomposite, giving a conductive character to CHI films [179]. Lavorgna *et al.* prepared nanocomposites using a CHI matrix with silver-montmorillonite antimicrobial behavior by replacing Na^+ ions of natural MMT with silver ions [180]. They were able to achieve enhanced mechanical performance, but more importantly they have shown that after 24 h a significant delay in *Pseudomonas aeruginosa* was obtained [180]. Lim *et al.* also explored the ability of rGO and CHI nanocomposites to retard the growth of *Pseudomonas aeruginosa* [181]. The achieved data revealed that bacterial growth was not dependent on the concentration and size of rGO and could be completely suppressed by the low concentration of rGO in the chitosan solution, leading to a maximum viability loss of 100% [181].

2.4.4 Biosensing

The detection of biologically active molecules is extremely important for biomedical purposes [90]. Nanomaterials have demonstrated great ability for biosensing applications once they are able

to achieve enhanced performances with increased sensitivities and lowered detection limits of several orders of magnitudes [198]. Singh and co-workers have demonstrated the achievement of an electrochemical DNA biosensor based on CHI/GO nanocomposites for rapid and sensitive detection of typhoid, using for that a Salmonella Typhi specific 5'-amine labeled single strand DNA (5'-NH₂-ssDNA), covalently bond through CHI/GO by glutaraldehyde [156]. The produced bioelectrode demonstrated to distinguish between complementary and non-complementary sequences, which in part may be related with the large surface-to-volume ratio and good electrochemical activity of GO, and good biocompatibility of CHI, which enhances the DNA immobilization and facilitate electron transfer between DNA and electrode surface [156]. A glucose biosensor developed with cytochrome c and glucose oxidase entrapped on gold nanoparticles and chitosan and constructed on a glassy carbon electrode was fabricate by Song *et al.* [158]. They demonstrated that the deposition of CHI/Au NPs led to an increase of the roughness to 9.51±0.12 nm, which revealed to be important to provide a large surface-to-volume ratio. Besides, a higher sensitivity to glucose and a lower detection limit was obtained [158]. Zhang *et al.* reported the fabrication of a haemoglobin/Au NPs/CHI/graphene biosensor developed on a glassy carbon electrode for hydrogen peroxide detection [157]. The electron transfer properties of the biosensor was analyzed using electrochemical impedance spectroscopy (EIS). The data showed that the use of haemoglobin, Au NPs and graphene improve the electron transfer, reducing the transfer resistance provide by CHI. Besides, a low detection limit (0.35 µM), a good stability (94%) for over one month and a high sensitivity (347.1 mA.cm⁻²M⁻¹) was found for these biosensors [157]. More efforts should be put in combining sensing ability in therapeutic strategies, in order to develop nanocomposites processed as NPs, fibres or coatings for theragnosis applications.

2.5 Conclusions

The use of CHI nanocomposites with different fillers and obtained through various processes have been proposed for different biomedical applications. CHI, a promising biomaterial that by itself presents outstanding properties, revealed to trigger the nanotechnology field when reinforced with various other nano-sized fillers. Depending on the application, the characteristics of each CHI nanocomposites can and must be controlled, designed and modulated regarding the target tissue.

Most of the nanocomposites result from the need to improve a critical feature that plays a major role in some specific tissue, such as the mechanical properties for bone regeneration,

antibacterial activity for wound healing or improved drug delivery for a targeted treatment. Independently of the target, the nanocomposite performance is closely related with the good dispersion of fillers within its polymeric matrix. The successful dispersion allows a good polymer/fillers interface that, independently of the application, always results in high specific interfacial area.

Successful findings have been reported such as osteogenic and osteoconductive nanocomposites when BG NPs are used with CHI, enhanced mechanical, thermal and conductive properties when the fillers are CNTs or graphene, or even antibacterial effects when Ag NPs are incorporated. However, even such promising results have been demonstrated by the described works, a lack of information exists concerning the *in vivo* or even pre-clinical studies. Thus, taking this into consideration, significant and important steps should be taken to understand the *in vivo* interaction of the nanocomposites devices with the host tissue. At the same time some key points should be further explored such as the ability of these materials to be sterilized using conventional methods to be then truly applied in real and daily clinical practice. Nevertheless, the vast opportunities shown by these materials allied with the incredible nanotechnology potential is expected to revolutionize the biomedical field in a near future.

2.6 References

- [1] Mai Y-W, Yu Z-Z. Polymer Nanocomposites- *Woodhead Publishing Series in Composites Science and Engineering*. Woodhead Publishing; 2006. p. 608.
- [2] Alves NM, Mano JF. Chitosan derivatives obtained by chemical modifications for biomedical and environmental applications. *International Journal of Biological Macromolecules*. 2008;43:401-14.
- [3] Rinaudo M. Chitin and chitosan: Properties and applications. *Progress in Polymer Science*. 2006;31:603-32.
- [4] Kumar M. A review of chitin and chitosan applications. *Reactive & Functional Polymers*. 2000;46:1-27.
- [5] Mano JF. Stimuli-responsive polymeric systems for biomedical applications. *Advanced Engineering Materials*. 2008;10:515-27.
- [6] Croisier F, Jerome C. Chitosan-based biomaterials for tissue engineering. *European Polymer Journal*. 2013;49:780-92.
- [7] Riva R, Ragelle H, des Rieux A, Duhem N, Jerome C, Preat V. Chitosan and Chitosan Derivatives in Drug Delivery and Tissue Engineering. In: Jayakumar R, Prabakaran M, Muzzarelli RAA, editors. *Chitosan for Biomaterials II*. Berlin: Springer-Verlag Berlin; 2011. p. 19-44.
- [8] Shahidi F, Arachchi JKV, Jeon YJ. Food applications of chitin and chitosans. *Trends in Food Science & Technology*. 1999;10:37-51.
- [9] Acosta N, Jimenez C, Borau V, Heras A. Extraction and characterization of chitin from crustaceans. *Biomass & Bioenergy*. 1993;5:145-53.
- [10] Madhally SV, Matthew HWT. Porous chitosan scaffolds for tissue engineering. *Biomaterials*. 1999;20:1133-42.
- [11] Kumar M, Muzzarelli RAA, Muzzarelli C, Sashiwa H, Domb AJ. Chitosan chemistry and pharmaceutical perspectives. *Chemical Reviews*. 2004;104:6017-84.
- [12] Singh DK, Ray AR. Biomedical applications of chitin, chitosan and their derivatives. *Rev Macromol Chem Phys*; 2000. p. 69-83.
- [13] Jayakumar R, Prabakaran M, Kumar PTS, Nair SV, Tamura H. Biomaterials based on chitin and chitosan in wound dressing applications. *Biotechnology Advances*. 2011;29:322-37.
- [14] Sudarshan NR, Hoover DG, Knorr D. Antibacterial action of chitosan. *Food Biotechnology*. 1992;6:257-72.
- [15] Ong SY, Wu J, Mochhala SM, Tan MH, Lu J. Development of a chitosan-based wound dressing with improved hemostatic and antimicrobial properties. *Biomaterials*. 2008;29:4323-32.
- [16] Yang J, Tian F, Wang Z, Wang Q, Zeng YJ, Chen SQ. Effect of chitosan molecular weight and deacetylation degree on Hemostasis. *Journal of Biomedical Materials Research Part B-Applied Biomaterials*. 2008;84B:131-7.
- [17] Jayakumar R, Reis RL, Mano JF. Chemistry and applications of phosphorylated chitin and chitosan. *E-Polymers*. 2006:16.
- [18] Lu GY, Kong LJ, Sheng BY, Wang G, Gong YD, Zhang XF. Degradation of covalently cross-linked carboxymethyl chitosan and its potential application for peripheral nerve regeneration. *European Polymer Journal*. 2007;43:3807-18.
- [19] Chaubaroux C, Vrana E, Debry C, Schaaf P, Senger B, Voegel JC, et al. Collagen-Based Fibrillar Multilayer Films Cross-Linked by a Natural Agent. *Biomacromolecules*. 2012;13:2128-35.
- [20] Ajayan PM, Schadler LS, Braun PV. *Nanocomposite Science and Technology*. John Wiley & Sons; 2006. p. 239.

- [21] Hu KS, Gupta MK, Kulkarni DD, Tsukruk VV. Ultra-Robust Graphene Oxide-Silk Fibroin Nanocomposite Membranes. *Advanced Materials*. 2013;25:2301-7.
- [22] Rinaudo M. Main properties and current applications of some polysaccharides as biomaterials. *Polymer International*. 2008;57:397-430.
- [23] Kuilla T, Bhadra S, Yao DH, Kim NH, Bose S, Lee JH. Recent advances in graphene based polymer composites. *Progress in Polymer Science*. 2010;35:1350-75.
- [24] Hu KS, Kulkarni DD, Choi I, Tsukruk VV. Graphene-polymer nanocomposites for structural and functional applications. *Progress in Polymer Science*. 2014;39:1934-72.
- [25] Fischer H. Polymer nanocomposites: from fundamental research to specific applications. *Materials Science & Engineering C-Biomimetic and Supramolecular Systems*. 2003;23:763-72.
- [26] Terrones M, Martin O, Gonzalez M, Pozuelo J, Serrano B, Cabanelas JC, et al. Interphases in Graphene Polymer-based Nanocomposites: Achievements and Challenges. *Advanced Materials*. 2011;23:5302-10.
- [27] Podsiadlo P, Tang ZY, Shim BS, Kotov NA. Counterintuitive effect of molecular strength and role of molecular rigidity on mechanical properties of layer-by-layer assembled nanocomposites. *Nano Letters*. 2007;7:1224-31.
- [28] Das P, Schipmann S, Malho JM, Zhu BL, Klemradt U, Walther A. Facile Access to Large-Scale, Self-Assembled, Nacre-Inspired, High-Performance Materials with Tunable Nanoscale Periodicities. *ACS Applied Materials & Interfaces*. 2013;5:3738-47.
- [29] Avérous L, Pollet E. Environmental Silicate Nano-Biocomposites In: Darder M, Aranda P, Ruiz-Hitzky E, editors. *Chitosan-Clay Bio-Nanocomposites*: Springer London; 2012. p. 365-91.
- [30] Motshekga SC, Ray SS, Onyango MS, Momba MNB. Preparation and antibacterial activity of chitosan-based nanocomposites containing bentonite-supported silver and zinc oxide nanoparticles for water disinfection. *Applied Clay Science*. 2015;114:330-9.
- [31] Dhivya S, Saravanan S, Sastry TP, Selvamurugan N. Nanohydroxyapatite-reinforced chitosan composite hydrogel for bone tissue repair in vitro and in vivo. *Journal of Nanobiotechnology*. 2015;13:13.
- [32] Xiang CL, Li R, Adhikari B, She Z, Li YX, Kraatz HB. Sensitive electrochemical detection of Salmonella with chitosan-gold nanoparticles composite film. *Talanta*. 2015;140:122-7.
- [33] Gupta P, Sharan S, Roy P, Lahiri D. Aligned carbon nanotube reinforced polymeric scaffolds with electrical cues for neural tissue regeneration. *Carbon*. 2015;95:715-24.
- [34] Song KL, Gao AQ, Cheng X, Xie KL. Preparation of the superhydrophobic nano-hybrid membrane containing carbon nanotube based on chitosan and its antibacterial activity. *Carbohydrate Polymers*. 2015;130:381-7.
- [35] Sengiz C, Congur G, Eksin E, Erdem A. Multiwalled Carbon Nanotubes-Chitosan Modified Single-Use Biosensors for Electrochemical Monitoring of Drug-DNA Interactions. *Electroanalysis*. 2015;27:1855-63.
- [36] He LH, Wang HF, Xia GM, Sun J, Song R. Chitosan/graphene oxide nanocomposite films with enhanced interfacial interaction and their electrochemical applications. *Applied Surface Science*. 2014;314:510-5.
- [37] Li YH, Sun JK, Du QJ, Zhang LH, Yang XX, Wu SL, et al. Mechanical and dye adsorption properties of graphene oxide/chitosan composite fibers prepared by wet spinning. *Carbohydrate Polymers*. 2014;102:755-61.
- [38] Han DL, Yan LF, Chen WF, Li W. Preparation of chitosan/graphene oxide composite film with enhanced mechanical strength in the wet state. *Carbohydrate Polymers*. 2011;83:653-8.
- [39] Alexandre M, Dubois P. Polymer-layered silicate nanocomposites: preparation, properties and uses of a new class of materials. *Materials Science & Engineering R-Reports*. 2000;28:1-63.

-
- [40] Azeez AA, Rhee KY, Park SJ, Hui D. Epoxy clay nanocomposites - processing, properties and applications: A review. *Composites Part B-Engineering*. 2013;45:308-20.
- [41] Reddy B. Advances in diverse industrial applications of nanocomposites. *Polymer/Clay Nanocomposites*. 2011.
- [42] Maisanaba S, Pichardo S, Puerto M, Gutierrez-Praena D, Camean AM, Jos A. Toxicological evaluation of clay minerals and derived nanocomposites: A review. *Environmental Research*. 2015;138:233-54.
- [43] Zeng QH, Yu AB, Lu GQ, Paul DR. Clay-based polymer nanocomposites: Research and commercial development. *Journal of Nanoscience and Nanotechnology*. 2005;5:1574-92.
- [44] Ray SS, Okamoto M. Polymer/layered silicate nanocomposites: a review from preparation to processing. *Progress in Polymer Science*. 2003;28:1539-641.
- [45] LeBaron PC, Wang Z, Pinnavaia TJ. Polymer-layered silicate nanocomposites: an overview. *Applied Clay Science*. 1999;15:11-29.
- [46] Arora A, Padua GW. Review: Nanocomposites in Food Packaging. *Journal of Food Science*. 2010;75:R43-R9.
- [47] Park SH, Lee HS, Choi JH, Jeong CM, Sung MH, Park HJ. Improvements in barrier properties of poly(lactic acid) films coated with chitosan or chitosan/clay nanocomposite. *Journal of Applied Polymer Science*. 2012;125:E675-E80.
- [48] Abdeen R, Salahuddin N. Modified Chitosan-Clay Nanocomposite as a Drug Delivery System Intercalation and In Vitro Release of Ibuprofen. *Journal of Chemistry*. 2013:9.
- [49] Lertsutthiwong P, Noomun K, Khunthon S, Limpanart S. Influence of chitosan characteristics on the properties of biopolymeric chitosan-montmorillonite. *Progress in Natural Science-Materials International*. 2012;22:502-8.
- [50] Ennajih H, Bouhfid R, Essassi EM, Bousmina M, El Kadib A. Chitosan-montmorillonite bio-based aerogel hybrid microspheres. *Microporous and Mesoporous Materials*. 2012;152:208-13.
- [51] Wang SS, Shu YQ, Liang BL, Gao LC, Gao M, Yin PG, et al. Nacre-inspired green artificial bionanocomposite films from the layer-by-layer assembly of montmorillonite and chitosan. *Chinese Journal of Polymer Science*. 2014;32:675-80.
- [52] Boccaccini AR, Erol M, Stark WJ, Mohn D, Hong ZK, Mano JF. Polymer/bioactive glass nanocomposites for biomedical applications: A review. *Composites Science and Technology*. 2010;70:1764-76.
- [53] Caridade SG, Merino EG, Alves NM, Bermudez VD, Boccaccini AR, Mano JF. Chitosan membranes containing micro or nano-size bioactive glass particles: evolution of biomineralization followed by in situ dynamic mechanical analysis. *Journal of the Mechanical Behavior of Biomedical Materials*. 2013;20:173-83.
- [54] Hench LL. Bioceramics. *Journal of the American Ceramic Society*. 1998;81:1705-28.
- [55] Rezwani K, Chen QZ, Blaker JJ, Boccaccini AR. Biodegradable and bioactive porous polymer/inorganic composite scaffolds for bone tissue engineering. *Biomaterials*. 2006;27:3413-31.
- [56] Hong Z, Reis RL, Mano JF. Preparation and in vitro characterization of novel bioactive glass ceramic nanoparticles. *Journal of Biomedical Materials Research Part A*. 2009;88A:304-13.
- [57] Hong ZK, Reis RL, Mano JF. Preparation and in vitro characterization of scaffolds of poly(L-lactic acid) containing bioactive glass ceramic nanoparticles. *Acta Biomaterialia*. 2008;4:1297-306.
- [58] Luz GM, Mano JF. Preparation and characterization of bioactive glass nanoparticles prepared by sol-gel for biomedical applications. *Nanotechnology*. 2011;22:11.
-

- [59] Mota J, Yu N, Caridade SG, Luz GM, Gomes ME, Reis RL, et al. Chitosan/bioactive glass nanoparticle composite membranes for periodontal regeneration. *Acta Biomaterialia*. 2012;8:4173-80.
- [60] Seuss S, Lehmann M, Boccaccini AR. Alternating Current Electrophoretic Deposition of Antibacterial Bioactive Glass-Chitosan Composite Coatings. *International Journal of Molecular Sciences*. 2014;15:12231-42.
- [61] Knowles JC. Phosphate based glasses for biomedical applications. *Journal of Materials Chemistry*. 2003;13:2395-401.
- [62] Okamoto M, John B. Synthetic biopolymer nanocomposites for tissue engineering scaffolds. *Progress in Polymer Science*. 2013;38:1487-503.
- [63] Lee JS, Baek SD, Venkatesan J, Bhatnagar I, Chang HK, Kim HT, et al. In vivo study of chitosan-natural nano hydroxyapatite scaffolds for bone tissue regeneration. *International Journal of Biological Macromolecules*. 2014;67:360-6.
- [64] Li XY, Nan KH, Shi S, Chen H. Preparation and characterization of nano-hydroxyapatite/chitosan cross-linking composite membrane intended for tissue engineering. *International Journal of Biological Macromolecules*. 2012;50:43-9.
- [65] Gu CH, Zhang H, Lang MD. Preparation of mono-dispersed silver nanoparticles assisted by chitosan-g-poly(epsilon-caprolactone) micelles and their antimicrobial application. *Applied Surface Science*. 2014;301:273-9.
- [66] Li M, Wang YH, Zhang Y, Yu JH, Ge SG, Yan M. Graphene functionalized porous Au-paper based electrochemiluminescence device for detection of DNA using luminescent silver nanoparticles coated calcium carbonate/carboxymethyl chitosan hybrid microspheres as labels. *Biosensors & Bioelectronics*. 2014;59:307-13.
- [67] Potara M, Jakab E, Damert A, Popescu O, Canpean V, Astilean S. Synergistic antibacterial activity of chitosan-silver nanocomposites on *Staphylococcus aureus*. *Nanotechnology*. 2011;22:9.
- [68] Du Y, Luo XL, Xu JJ, Chen HY. A simple method to fabricate a chitosan-gold nanoparticles film and its application in glucose biosensor. *Bioelectrochemistry*. 2007;70:342-7.
- [69] Li LH, Deng JC, Deng HR, Liu ZL, Xin L. Synthesis and characterization of chitosan/ZnO nanoparticle composite membranes. *Carbohydrate Research*. 2010;345:994-8.
- [70] de Godoi FC, Rodriguez-Castellon E, Guibal E, Beppu MM. An XPS study of chromate and vanadate sorption mechanism by chitosan membrane containing copper nanoparticles. *Chemical Engineering Journal*. 2013;234:423-9.
- [71] Song XL, Luo XD, Zhang QQ, Zhu AP, Ji LJ, Yan CF. Preparation and characterization of biofunctionalized chitosan/Fe₃O₄ magnetic nanoparticles for application in liver magnetic resonance imaging. *Journal of Magnetism and Magnetic Materials*. 2015;388:116-22.
- [72] Zhao LQ, Xue FM, Yu BW, Xie JR, Zhang XL, Wu RH, et al. TiO₂-graphene sponge for the removal of tetracycline. *Journal of Nanoparticle Research*. 2015;17:9.
- [73] Peponi L, Puglia D, Torre L, Valentini L, Kenny JM. Processing of nanostructured polymers and advanced polymeric based nanocomposites. *Materials Science & Engineering R-Reports*. 2014;85:1-46.
- [74] Iijima S. Helical microtubules of graphitic carbon. *Nature*. 1991;354:56-8.
- [75] Thostenson ET, Ren ZF, Chou TW. Advances in the science and technology of carbon nanotubes and their composites: a review. *Composites Science and Technology*. 2001;61:1899-912.
- [76] Moniruzzaman M, Winey KI. Polymer nanocomposites containing carbon nanotubes. *Macromolecules*. 2006;39:5194-205.

-
- [77] Coleman JN, Khan U, Blau WJ, Gun'ko YK. Small but strong: A review of the mechanical properties of carbon nanotube-polymer composites. *Carbon*. 2006;44:1624-52.
- [78] Li CY, Chou TW. Elastic moduli of multi-walled carbon nanotubes and the effect of van der Waals forces. *Composites Science and Technology*. 2003;63:1517-24.
- [79] De Volder MFL, Tawfick SH, Baughman RH, Hart AJ. Carbon Nanotubes: Present and Future Commercial Applications. *Science*. 2013;339:535-9.
- [80] Monthieux M. Filling single-wall carbon nanotubes. *Carbon*. 2002;40:1809-23.
- [81] Yu MF, Lourie O, Dyer MJ, Moloni K, Kelly TF, Ruoff RS. Strength and breaking mechanism of multiwalled carbon nanotubes under tensile load. *Science*. 2000;287:637-40.
- [82] Collins PG, Avouris P. Nanotubes for electronics. *Scientific American*. 2000;283:62.
- [83] Wei BQ, Vajtai R, Ajayan PM. Reliability and current carrying capacity of carbon nanotubes. *Applied Physics Letters*. 2001;79:1172-4.
- [84] Che JW, Cagin T, Goddard WA. Thermal conductivity of carbon nanotubes. *Nanotechnology*. 2000;11:65-9.
- [85] Osman MA, Srivastava D. Temperature dependence of the thermal conductivity of single-wall carbon nanotubes. *Nanotechnology*. 2001;12:21-4.
- [86] Berber S, Kwon YK, Tomanek D. Unusually high thermal conductivity of carbon nanotubes. *Physical Review Letters*. 2000;84:4613-6.
- [87] Farsi M, Sani FM. Effects of multi-walled carbon nanotubes on the physical and mechanical properties of high-density polyethylene/wood flour nanocomposites. *Journal of Thermoplastic Composite Materials*. 2014;27:1139-54.
- [88] Jones DEH. Science of fullerenes and carbon nanotubes - Dresselhaus,MS, Dresselhaus,G, Eklund,PC. *Nature*. 1996;381:384.
- [89] Lehman JH, Terrones M, Mansfield E, Hurst KE, Meunier V. Evaluating the characteristics of multiwall carbon nanotubes. *Carbon*. 2011;49:2581-602.
- [90] Bitounis D, Ali-Boucetta H, Hong BH, Min DH, Kostarelos K. Prospects and Challenges of Graphene in Biomedical Applications. *Advanced Materials*. 2013;25:2258-68.
- [91] Rahmat M, Hubert P. Carbon nanotube-polymer interactions in nanocomposites: A review. *Composites Science and Technology*. 2011;72:72-84.
- [92] Hwang JY, Kim HS, Kim JH, Shin US, Lee SH. Carbon Nanotube Nanocomposites with Highly Enhanced Strength and Conductivity for Flexible Electric Circuits. *Langmuir*. 2015;31:7844-51.
- [93] Hirsch A. Functionalization of single-walled carbon nanotubes. *Angewandte Chemie-International Edition*. 2002;41:1853-9.
- [94] Slonczewski JC, Weiss PR. Band structure of graphite. *Physical Review*. 1958;109:272-9.
- [95] Chen J, Yao BW, Li C, Shi GQ. An improved Hummers method for eco-friendly synthesis of graphene oxide. *Carbon*. 2013;64:225-9.
- [96] Novoselov KS, Fal'ko VI, Colombo L, Gellert PR, Schwab MG, Kim K. A roadmap for graphene. *Nature*. 2012;490:192-200.
- [97] Mayorov AS, Gorbachev RV, Morozov SV, Britnell L, Jalil R, Ponomarenko LA, et al. Micrometer-Scale Ballistic Transport in Encapsulated Graphene at Room Temperature. *Nano Letters*. 2011;11:2396-9.
- [98] Zhu YW, Murali S, Cai WW, Li XS, Suk JW, Potts JR, et al. Graphene and Graphene Oxide: Synthesis, Properties, and Applications. *Advanced Materials*. 2010;22:3906-24.
- [99] Nair RR, Blake P, Grigorenko AN, Novoselov KS, Booth TJ, Stauber T, et al. Fine structure constant defines visual transparency of graphene. *Science*. 2008;320:1308.
- [100] Allen MJ, Tung VC, Kaner RB. Honeycomb Carbon: A Review of Graphene. *Chemical Reviews*. 2010;110:132-45.
-

- [101] Dreyer DR, Park S, Bielawski CW, Ruoff RS. The chemistry of graphene oxide. *Chemical Society Reviews*. 2010;39:228-40.
- [102] Wang GX, Yang J, Park J, Gou XL, Wang B, Liu H, et al. Facile synthesis and characterization of graphene nanosheets. *Journal of Physical Chemistry C*. 2008;112:8192-5.
- [103] Compton OC, Nguyen ST. Graphene Oxide, Highly Reduced Graphene Oxide, and Graphene: Versatile Building Blocks for Carbon-Based Materials. *Small*. 2010;6:711-23.
- [104] Shen H, Zhang LM, Liu M, Zhang ZJ. Biomedical Applications of Graphene. *Theranostics*. 2012;2:283-94.
- [105] Stankovich S, Dikin DA, Dommett GHB, Kohlhaas KM, Zimney EJ, Stach EA, et al. Graphene-based composite materials. *Nature*. 2006;442:282-6.
- [106] Park S, An JH, Piner RD, Jung I, Yang DX, Velamakanni A, et al. Aqueous Suspension and Characterization of Chemically Modified Graphene Sheets. *Chemistry of Materials*. 2008;20:6592-4.
- [107] Luz GM, Mano JF. Biomimetic design of materials and biomaterials inspired by the structure of nacre. *Philosophical Transactions of the Royal Society a-Mathematical Physical and Engineering Sciences*. 2009;367:1587-605.
- [108] Fan HL, Wang LL, Zhao KK, Li N, Shi ZJ, Ge ZG, et al. Fabrication, Mechanical Properties, and Biocompatibility of Graphene-Reinforced Chitosan Composites. *Biomacromolecules*. 2010;11:2345-51.
- [109] Li JH, Ren N, Qiu JC, Mou XN, Liu H. Graphene oxide-reinforced biodegradable genipin-cross-linked chitosan fluorescent biocomposite film and its cytocompatibility. *International Journal of Nanomedicine*. 2013;8:3415-26.
- [110] Zheng YY, Monty J, Linhardt RJ. Polysaccharide-based nanocomposites and their applications. *Carbohydrate Research*. 2015;405:23-32.
- [111] Ambrosio L. *Biomedical Composites*. Elsevier; 2009.
- [112] Boccaccini A, Ma PX. *Tissue Engineering Using Ceramics and Polymers*. 2nded: Woodhead Publishing 2014. p. 728.
- [113] Luz GM, Mano JF. Chitosan/bioactive glass nanoparticles composites for biomedical applications. *Biomedical Materials*. 2012;7:9.
- [114] Depan D. *Biodegradable Polymeric Nanocomposites: Advances in Biomedical Applications*. CRC Press; 2015. p. 257.
- [115] Caridade SG, Merino EG, Alves NM, Mano JF. Bioactivity and Viscoelastic Characterization of Chitosan/Bioglass (R) Composite Membranes. *Macromolecular Bioscience*. 2012;12:1106-13.
- [116] Kithva P, Grondahl L, Martin D, Trau M. Biomimetic synthesis and tensile properties of nanostructured high volume fraction hydroxyapatite and chitosan biocomposite films. *Journal of Materials Chemistry*. 2010;20:381-9.
- [117] He YQ, Zhang NN, Wang WC, He SY, Gong QJ, Qiu HX, et al. Preparation of Reduced Graphene Oxide/Chitosan Composite Films with Reinforced Mechanical Strength. *Frontiers of Advanced Materials and Engineering Technology, Pts 1-3*. 2012;430-432:247-50.
- [118] Sarmiento B, Neves J. *Chitosan-Based Systems for Biopharmaceuticals: Deliver, Targeting and Polymer Therapeutics*. John Wiley & Sons; 2012.
- [119] Anisha BS, Biswas R, Chennazhi KP, Jayakumar R. Chitosan-hyaluronic acid/nano silver composite sponges for drug resistant bacteria infected diabetic wounds. *International Journal of Biological Macromolecules*. 2013;62:310-20.
- [120] Mohandes F, Salavati-Niasari M. Freeze-drying synthesis, characterization and in vitro bioactivity of chitosan/graphene oxide/hydroxyapatite nanocomposite. *Rsc Advances*. 2014;4:25993-6001.

- [121] Olad A, Azhar FF. The synergetic effect of bioactive ceramic and nanoclay on the properties of chitosan-gelatin/nanohydroxyapatite-montmorillonite scaffold for bone tissue engineering. *Ceramics International*. 2014;40:10061-72.
- [122] Sun F, Cha HR, Bae K, Hong S, Kim JM, Kim SH, et al. Mechanical properties of multilayered chitosan/CNT nanocomposite films. *Materials Science and Engineering a-Structural Materials Properties Microstructure and Processing*. 2011;528:6636-41.
- [123] Iler RK. Multilayers of colloidal particles. *Journal of Colloid and Interface Science*. 1966;21:569.
- [124] Decher G. Fuzzy nanoassemblies: Toward layered polymeric multicomposites. *Science*. 1997;277:1232-7.
- [125] Borges J, Rodrigues LC, Reis RL, Mano JF. Layer-by-Layer Assembly of Light-Responsive Polymeric Multilayer Systems. *Advanced Functional Materials*. 2014;24:5624-48.
- [126] Borges J, Mano JF. Molecular Interactions Driving the Layer-by-Layer Assembly of Multilayers. *Chemical Reviews*. 2014;114:8883-942.
- [127] Richardson JJ, Bjornmalm M, Caruso F. Multilayer assembly. Technology-driven layer-by-layer assembly of nanofilms. *Science (New York, NY)*. 2015;2348:2491.
- [128] Caridade SG, Monge C, Gilde F, Boudou T, Mano JF, Picart C. Free-Standing Polyelectrolyte Membranes Made of Chitosan and Alginate. *Biomacromolecules*. 2013;14:1653-60.
- [129] Costa RR, Mano JF. Polyelectrolyte multilayered assemblies in biomedical technologies. *Chemical Society Reviews*. 2014;43:3453-79.
- [130] Yang GJ, Yang XY, Zhang L, Lin M, Sun XL, Chen XY, et al. Counterionic biopolymers-reinforced bioactive glass scaffolds with improved mechanical properties in wet state. *Materials Letters*. 2012;75:80-3.
- [131] Pavinatto A, Mercante LA, Leandro CS, Mattoso LHC, Correa DS. Layer-by-Layer assembled films of chitosan and multi-walled carbon nanotubes for the electrochemical detection of 17 alpha-ethinylestradiol. *Journal of Electroanalytical Chemistry*. 2015;755:215-20.
- [132] Couto DS, Alves NM, Mano JF. Nanostructured Multilayer Coatings Combining Chitosan with Bioactive Glass Nanoparticles. *Journal of Nanoscience and Nanotechnology*. 2009;9:1741-8.
- [133] Martins A, Reis RL, Neves NM. Electrospinning: processing technique for tissue engineering scaffolding. *International Materials Reviews*. 2008;53:257-74.
- [134] Teo WE, Ramakrishna S. A review on electrospinning design and nanofibre assemblies. *Nanotechnology*. 2006;17:R89-R106.
- [135] Frohbergh ME, Katsman A, Botta GR, Lazarovici P, Schauer CL, Wegst UGK, et al. Electrospun hydroxyapatite-containing chitosan nanofibers crosslinked with genipin for bone tissue engineering. *Biomaterials*. 2012;33:9167-78.
- [136] Silva CSR, Luz GM, Gamboa-Martinez TC, Mano JF, Ribelles JLG, Gomez-Tejedor JA. Poly(ϵ -caprolactone) Electrospun Scaffolds Filled with Nanoparticles. Production and Optimization According to Taguchi's Methodology. *Journal of Macromolecular Science Part B-Physics*. 2014;53:781-99.
- [137] Bai BY, Mi X, Xiang X, Heiden PA, Heldt CL. Non-enveloped virus reduction with quaternized chitosan nanofibers containing graphene. *Carbohydrate Research*. 2013;380:137-42.
- [138] Najafabadi HH, Irani M, Rad LR, Haratameh AH, Haririan I. Removal of Cu²⁺, Pb²⁺ and Cr⁶⁺ from aqueous solutions using a chitosan/graphene oxide composite nanofibrous adsorbent. *Rsc Advances*. 2015;5:16532-9.
- [139] Lee SJ, Heo DN, Moon JH, Ko WK, Lee JB, Bae MS, et al. Electrospun chitosan nanofibers with controlled levels of silver nanoparticles. Preparation, characterization and antibacterial activity. *Carbohydrate Polymers*. 2014;111:530-7.

- [140] Mandieh ZM, Mottaghitlab V, Piri N, Haghi AK. Conductive chitosan/multi walled carbon nanotubes electrospun nanofiber feasibility. *Korean Journal of Chemical Engineering*. 2012;29:111-9.
- [141] Mittal V. In-Situ Synthesis of Polymer Nanocomposites. 2011. p. 1-25.
- [142] Liu YT, Long T, Tang S, Sun JL, Zhu ZA, Guo YP. Biomimetic fabrication and biocompatibility of hydroxyapatite/chitosan nanohybrid coatings on porous carbon fiber felts. *Materials Letters*. 2014;128:31-4.
- [143] Chen L, Hu JX, Shen XY, Tong H. Synthesis and characterization of chitosan-multiwalled carbon nanotubes/hydroxyapatite nanocomposites for bone tissue engineering. *Journal of Materials Science-Materials in Medicine*. 2013;24:1843-51.
- [144] McMahon RE, Wang LN, Skoracki R, Mathur AB. Development of nanomaterials for bone repair and regeneration. *Journal of Biomedical Materials Research Part B-Applied Biomaterials*. 2013;101B:387-97.
- [145] Luz GM, Mano JF. Mineralized structures in nature: Examples and inspirations for the design of new composite materials and biomaterials. *Composites Science and Technology*. 2010;70:1777-88.
- [146] Song J, Malathong V, Bertozzi CR. Mineralization of synthetic polymer scaffolds: A bottom-up approach for the development of artificial bone. *Journal of the American Chemical Society*. 2005;127:3366-72.
- [147] Wu CJ, Gaharwar AK, Schexnailder PJ, Schmidt G. Development of Biomedical Polymer-Silicate Nanocomposites: A Materials Science Perspective. *Materials*. 2010;3:2986-3005.
- [148] Oliveira MB, Luz GM, Mano JF. A combinatorial study of nanocomposite hydrogels: on-chip mechanical/viscoelastic and pre-osteoblast interaction characterization. *Journal of Materials Chemistry B*. 2014;2:5627-38.
- [149] Jayakumar R, Prabakaran M, Reis RL, Mano JF. Graft copolymerized chitosan - present status and applications. *Carbohydrate Polymers*. 2005;62:142-58.
- [150] Sahoo NG, Pan YZ, Li L, He CB. Nanocomposites for bone tissue regeneration. *Nanomedicine*. 2013;8:639-53.
- [151] Alves NM, Leonor IB, Azevedo HS, Reis RL, Mano JF. Designing biomaterials based on biomineralization of bone. *Journal of Materials Chemistry*. 2010;20:2911-21.
- [152] Olszta MJ, Cheng XG, Jee SS, Kumar R, Kim YY, Kaufman MJ, et al. Bone structure and formation: A new perspective. *Materials Science & Engineering R-Reports*. 2007;58:77-116.
- [153] Venkatesan J, Jayakumar R, Mohandas A, Bhatnagar I, Kim SK. Antimicrobial Activity of Chitosan-Carbon Nanotube Hydrogels. *Materials*. 2014;7:3946-55.
- [154] Shan CS, Yang HF, Han DX, Zhang QX, Ivaska A, Niu L. Graphene/AuNPs/chitosan nanocomposites film for glucose biosensing. *Biosensors & Bioelectronics*. 2010;25:1070-4.
- [155] Van Thu V, Dung PT, Tam LT, Tam PD. Biosensor based on nanocomposite material for pathogenic virus detection. *Colloids and surfaces B, Biointerfaces*. 2014;115:176-81.
- [156] Singh A, Sinsinbar G, Choudhary M, Kumar V, Pasricha R, Verma HN, et al. Graphene oxide-chitosan nanocomposite based electrochemical DNA biosensor for detection of typhoid. *Sensors and Actuators B-Chemical*. 2013;185:675-84.
- [157] Zhang LL, Han GQ, Liu Y, Tang J, Tang WH. Immobilizing haemoglobin on gold/graphene-chitosan nanocomposite as efficient hydrogen peroxide biosensor. *Sensors and Actuators B-Chemical*. 2014;197:164-71.
- [158] Song YH, Liu HY, Wang Y, Wang L. A glucose biosensor based on cytochrome c and glucose oxidase co-entrapped in chitosan- gold nanoparticles modified electrode. *Analytical Methods*. 2013;5:4165-71.

-
- [159] Fan JJ, Bi L, Wu T, Cao LG, Wang DX, Nan KH, et al. A combined chitosan/nano-size hydroxyapatite system for the controlled release of icariin. *Journal of Materials Science-Materials in Medicine*. 2012;23:399-407.
- [160] Pallela R, Venkatesan J, Janapala VR, Kim SK. Biophysicochemical evaluation of chitosan-hydroxyapatite-marine sponge collagen composite for bone tissue engineering. *Journal of Biomedical Materials Research Part A*. 2012;100A:486-95.
- [161] Im O, Li J, Wang M, Zhang LG, Keidar M. Biomimetic three-dimensional nanocrystalline hydroxyapatite and magnetically synthesized single-walled carbon nanotube chitosan nanocomposite for bone regeneration. *International Journal of Nanomedicine*. 2012;7:2087-99.
- [162] Correia CO, Leite AJ, Mano JF. Chitosan/bioactive glass nanoparticles scaffolds with shape memory properties. *Carbohydrate Polymers*. 2015;123:39-45.
- [163] Depan D, Girase B, Shah JS, Misra RDK. Structure-process-property relationship of the polar graphene oxide-mediated cellular response and stimulated growth of osteoblasts on hybrid chitosan network structure nanocomposite scaffolds. *Acta Biomaterialia*. 2011;7:3432-45.
- [164] Yuan Q, Shah J, Hein S, Misra RDK. Controlled and extended drug release behavior of chitosan-based nanoparticle carrier. *Acta Biomaterialia*. 2010;6:1140-8.
- [165] Abou Taleb MF, Alkahtani A, Mohamed SK. Radiation synthesis and characterization of sodium alginate/chitosan/hydroxyapatite nanocomposite hydrogels: a drug delivery system for liver cancer. *Polymer Bulletin*. 2015;72:725-42.
- [166] Justin R, Chen BQ. Strong and conductive chitosan-reduced graphene oxide nanocomposites for transdermal drug delivery. *Journal of Materials Chemistry B*. 2014;2:3759-70.
- [167] Salcedo I, Sandri G, La Aguzzi C, Bonferoni C, Cerezo P, Sanchez-Espejo R, et al. Intestinal permeability of oxytetracycline from chitosan-montmorillonite nanocomposites. *Colloids and Surfaces B-Biointerfaces*. 2014;117:441-8.
- [168] Axpe E, Bugnicourt L, Merida D, Goiriena-Goikoetxea M, Unzueta I, Sanchez-Eugenia R, et al. Sub-nanoscale free volume and local elastic modulus of chitosan-carbon nanotube biomimetic nanocomposite scaffold-materials. *Journal of Materials Chemistry B*. 2015;3:3169-76.
- [169] Sayyar S, Murray E, Thompson BC, Chung J, Officer DL, Gambhir S, et al. Processable conducting graphene/chitosan hydrogels for tissue engineering. *Journal of Materials Chemistry B*. 2015;3:481-90.
- [170] Liverani L, Abbruzzese F, Mozetic P, Basoli F, Rainer A, Trombetta M. Electrospinning of hydroxyapatite-chitosan nanofibers for tissue engineering applications. *Asia-Pacific Journal of Chemical Engineering*. 2014;9:407-14.
- [171] Liu HH, Peng HJ, Wu Y, Zhang C, Cai YZ, Xu GW, et al. The promotion of bone regeneration by nanofibrous hydroxyapatite/chitosan scaffolds by effects on integrin-BMP/Smad signaling pathway in BMSCs. *Biomaterials*. 2013;34:4404-17.
- [172] Depan D, Kumar AP, Singh RP, Misra RDK. Stability of chitosan/montmorillonite nanohybrid towards enzymatic degradation on grafting with poly(lactic acid). *Materials Science and Technology*. 2014;30:587-92.
- [173] Bellingeri R, Alustiza F, Picco N, Acevedo D, Molina MA, Rivero R, et al. In Vitro Toxicity Evaluation of Hydrogel-Carbon Nanotubes Composites on Intestinal Cells. *Journal of Applied Polymer Science*. 2015;132:7.
- [174] Martins AM, Eng G, Caridade SG, Mano JF, Reis RL, Vunjak-Novakovic G. Electrically Conductive Chitosan/Carbon Scaffolds for Cardiac Tissue Engineering. *Biomacromolecules*. 2014;15:635-43.
-

- [175] Peng CC, Yang MH, Chiu WT, Chiu CH, Yang CS, Chen YW, et al. Composite nano-titanium oxide-chitosan artificial skin exhibits strong wound-healing effect - An approach with anti-inflammatory and bactericidal kinetics. *Macromolecular Bioscience*. 2008;8:316-27.
- [176] Liu Y, Kim HI. Characterization and antibacterial properties of genipin-crosslinked chitosan/poly(ethylene glycol)/ZnO/Ag nanocomposites. *Carbohydrate Polymers*. 2012;89:111-6.
- [177] Lu BG, Li T, Zhao HT, Li XD, Gao CT, Zhang SX, et al. Graphene-based composite materials beneficial to wound healing. *Nanoscale*. 2012;4:2978-82.
- [178] Aguzzi C, Sandri G, Bonferoni C, Cerezo P, Rossi S, Ferrari F, et al. Solid state characterisation of silver sulfadiazine loaded on montmorillonite/chitosan nanocomposite for wound healing. *Colloids and Surfaces B-Biointerfaces*. 2014;113:152-7.
- [179] Gonzalez-Campos JB, Mota-Morales JD, Kumar S, Zarate-Trivino D, Hernandez-Iturriaga M, Prokhorov Y, et al. New insights into the bactericidal activity of chitosan-Ag bionanocomposite: The role of the electrical conductivity. *Colloids and Surfaces B-Biointerfaces*. 2013;111:741-6.
- [180] Lavorgna M, Attianese I, Buonocore GG, Conte A, Del Nobile MA, Tescione F, et al. MMT-supported Ag nanoparticles for chitosan nanocomposites: Structural properties and antibacterial activity. *Carbohydrate Polymers*. 2014;102:385-92.
- [181] Lim HN, Huang NM, Loo CH. Facile preparation of graphene-based chitosan films: Enhanced thermal, mechanical and antibacterial properties. *Journal of Non-Crystalline Solids*. 2012;358:525-30.
- [182] James R, Deng M, Laurencin CT, Kumbar SG. Nanocomposites and bone regeneration. *Frontiers of Materials Science*. 2011;5:342-57.
- [183] Duan B, Wang M, Zhou WY, Cheung WL, Li ZY, Lu WW. Three-dimensional nanocomposite scaffolds fabricated via selective laser sintering for bone tissue engineering. *Acta Biomaterialia*. 2010;6:4495-505.
- [184] Goulet JA, Senunas LE, DeSilva GL, Greenfield M. Autogenous iliac crest bone graft - Complications and functional assessment. *Clinical Orthopaedics and Related Research*. 1997:76-81.
- [185] Mura S, Nicolas J, Couvreur P. Stimuli-responsive nanocarriers for drug delivery. *Nature Materials*. 2013;12:991-1003.
- [186] Lima AC, Sher P, Mano JF. Production methodologies of polymeric and hydrogel particles for drug delivery applications. *Expert Opinion on Drug Delivery*. 2012;9:231-48.
- [187] Goenka S, Sant V, Sant S. Graphene-based nanomaterials for drug delivery and tissue engineering. *Journal of Controlled Release*. 2014;173:75-88.
- [188] Kashyap M, Archana D, Semwal A, Dutta J, Dutta P. Chitin and Chitosan for Regenerative Medicine In: *Medicine CaCfR*, editor.: Springer; 2015. p. 389.
- [189] Prabakaran M, Mano JF. Chitosan-based particles as controlled drug delivery systems. *Drug Delivery*. 2005;12:41-57.
- [190] Justin R, Chen BQ. Characterisation and drug release performance of biodegradable chitosan-graphene oxide nanocomposites. *Carbohydrate Polymers*. 2014;103:70-80.
- [191] Mo YF, Wang HW, Liu JH, Lan Y, Guo R, Zhang Y, et al. Controlled release and targeted delivery to cancer cells of doxorubicin from polysaccharide-functionalised single-walled carbon nanotubes. *Journal of Materials Chemistry B*. 2015;3:1846-55.
- [192] Kataria K, Gupta A, Rath G, Mathur RB, Dhakate SR. In vivo wound healing performance of drug loaded electrospun composite nanofibers transdermal patch. *International Journal of Pharmaceutics*. 2014;469:102-10.
- [193] Guo S, DiPietro LA. Factors Affecting Wound Healing. *Journal of Dental Research*. 2010;89:219-29.

- [194] Abrigo M, McArthur SL, Kingshott P. Electrospun Nanofibers as Dressings for Chronic Wound Care: Advances, Challenges, and Future Prospects. *Macromolecular Bioscience*. 2014;14:772-92.
- [195] Zhong SP, Zhang YZ, Lim CT. Tissue scaffolds for skin wound healing and dermal reconstruction. *Wiley Interdisciplinary Reviews-Nanomedicine and Nanobiotechnology*. 2010;2:510-25.
- [196] Gu SY, Wang ZM, Ren J, Zhang CY. Electrospinning of gelatin and gelatin/poly(L-lactide) blend and its characteristics for wound dressing. *Materials Science & Engineering C-Materials for Biological Applications*. 2009;29:1822-8.
- [197] Costa AMS, Mano JF. Highly robust hydrogels via a fast, simple and cytocompatible dual crosslinking-based process. *Chemical Communications*. 2015;51:15673-6.
- [198] Holzinger M, Le Goff A, Cosnier S. Nanomaterials for biosensing applications: a review. *Frontiers in chemistry*. 2014;2:63.

CHAPTER 3. MATERIALS AND METHODS

3. MATERIALS AND METHODS

The goal of this chapter is to list and describe the materials and experimental methods employed during this work in order to produce graphene oxide and multilayered free-standing membranes. In this chapter, it will be also highlighted the techniques used to characterize the materials.

3.1 Materials

3.1.1 Graphene Oxide (GO)

Multi-walled carbon nanotubes (MWNTs; NC7000- Thin Multiwall Nanotubes) with a purity of 90% and with an average length of 1.5 μm were purchased from Nanocyl™. Exfoliated graphite (EG) with a purity of 99.5% and with an average length of 9.9 μm was obtained from Nacional de Grafite Ltda.

To overcome the poor solubility in solvents, it was important to covalently functionalize the surface of MWNTs and EG through a chemical oxidation. The oxidation process was achieved using different reagents, namely: sulfuric acid (H_2SO_4 ; 95-97%), potassium permanganate (KMnO_4) analytical reagent grade, hydrogen peroxide analytical reagent grade (H_2O_2 ; >30% w/v), hydrochloric acid (HCl ; 10% v/v), all purchased from Fisher Scientific (UK), and distilled water (DW).

3.1.2 Free-Standing (FS) Multilayered Membranes

Chitosan (CHI) of medium molecular weight was purchased from Sigma-Aldrich (Germany), with a degree of N-deacetylation (DD) ranging from 75-85% and a viscosity of 200-800 cP. Prior to be used, the CHI was purified by a recrystallization process. In order to prepare the solutions for the LbL technique, the purified CHI was dissolved in DW and acetic acid 1% (v/v).

The other polyelectrolyte used for the production of FS membranes was sodium alginate (ALG) from brown algae, with a viscosity of 5 to 40 cP, purchased by Sigma-Aldrich. The ALG solutions were prepared dissolving the desirable amount in DW for a 2 mg/mL concentration.

3.2 Methods

3.2.1 Synthesis of GO

The most widely applied method for graphene oxide (GO) production is the modified Hummers method. Starting with the EG, it was extensively oxidized through strong acids and oxidizing agents resulting in oxidized graphene flakes (o-GFs). The main steps performed during this procedure were: 5 g of EG were poured in a dried round bottom flask (100 mL) followed by the addition of 400 mL of H_2SO_4 . The addition of sulfuric acid to the EG reveals to be extremely important, once it acts as a chemical scissor and a chemical drill for graphene planes, facilitating the penetration of the oxidation solution [1]. During 2 hours the solution was magnetically stirred to properly mix the solution in an ice-bath condition; then, 25 g of potassium permanganate (KMnO_4) (corresponding to 5 times the mass of the EG) were slowly added to the previous solution and kept stirring for 15 minutes in an ice-bath condition and left stirring overnight at room temperature. The addition of KMnO_4 is responsible for graphite bisulfate formation once it allows a complete intercalation of H_2SO_4 in every single layer of graphene, resulting in intercalated bisulfate ions. This complete intercalation ensures diffusion of KMnO_4 solution into graphene layers for the oxidation of graphite [1, 2]. After this 15 minutes, the mixture was kept stirring for 2 hours more, at room temperature. Consecutively and to achieve the purification of the mixture, the solution was placed again in an ice-bath and 300 mL of DW were slowly added, changing the solution's color from black to brownish. Then, 30 mL of H_2O_2 were added drop-by-drop, at this stage was possible to visualize another color changing, from brownish to yellowish, see Figure 3.1.



Figure 3.1 Representation of the color changing along with the procedure evolution. **(a)** Magnetic stirring of the solution with EG and H_2SO_4 (solution completely black); **(b)** solution after adding 300 mL of DW (brownish solution) and **(c)** solution following the H_2O_2 adding (yellow solution).

Follow that, the solution was poured into 45 mL tubes and centrifuged under 3500 rpm in a Labofuge 400 (Heraeus Instruments, USA) for 15 minutes. The supernatant was poured away

and the precipitate was washed with DW. These last two steps were repeated 3 times. The resulting precipitate was then collected and poured in another round flask, followed by addition of 250 mL of HCl (10% v/v) and it was left stirring for 15 minutes. The mixture was once again centrifuged for 3 cycles. After the centrifugation procedure, the supernatant was poured away and DW was added to the solid part and then filtrated with a nylon membrane filter (Whatman, UK). The result was dried for 48 h at 100 °C and then milled.

The resultant powder was evaluated using Raman spectroscopy and TGA, before being dispersed in DW. The o-GF solution was obtained by dispersing 57 mg of o-EG powder in 250 mL of DW followed by exposition to 4 hours of ultrasound in a Hielscher ultrasound machine (Ultrasound Technology, Germany) .

Regarding the oxidation of the MWNTs, a similar but more aggressive oxidation process was performed. 4g of MWNTs were poured in a clean 1000 mL round flask and suspended in 500 mL of H₂SO₄, before stirred for 4 hours. Subsequently, 32 g of KMnO₄ (corresponding to 8 times the values of MWNTs) were slowly added and the solution was kept stirring for 2 hours in an ice-bath condition. Then, the mixture was heated up to 60 °C and mixed over-night. During this time the opening of the nanotubes should occur since the mechanism of opening is based on the oxidation of alkenes by permanganate in acid media, as reported by Kosynkyn *et al.*, Figure 3.2 [3].

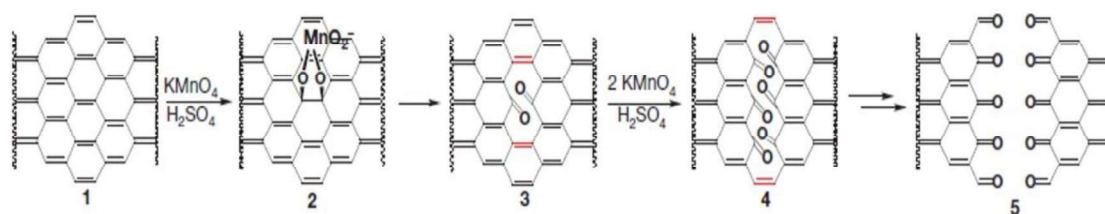


Figure 3.2 Schematic representation of the nanoribbons process. **1)** Initial conformation of MWNTs; **2)** Manganate ester formation; **3)** with further oxidation is possible to achieve the dione; **4)** next to the ketones there is distorts of the β,γ alkenes (red part), making them more prone to the next attack by permanganate. As the process continues, the strength ketones induce less strain on the β,γ alkenes since there is more space for carbonyl projection, however the enlarging hole make them more reactive. The opening has been initiate and the ketones can be converted to carboxylic acid which will be responsible for the aligning of the nanoribbons edges; **5)** the nanotube opens and originates the graphene ribbon [3].

The same purification process was performed, including the addition of 300 mL of H₂O followed by 30 mL of H₂O₂, all steps were performed with the solution placed in an ice-bath. The mixture was centrifuged for 15 minutes under 3500 rpm. The supernatant was poured away and the resulting black sediment was washed with DW followed by another centrifugation cycle. This step was performed 3 times and then the mixture was poured in a round flask, where 250 mL of

HCl (10% v/v) were added and stirred for 10 min. The solution was again centrifuged twice and the mixture was filtrated. The result was dried for 48 hours at 100 °C and finally milled.

Similarly, the resultant powder was evaluated using Raman spectroscopy and TGA, before being dispersed in DW. Finally the o-GNR solution was obtain dispersing 57 mg of o-MWNT powder in 250 mL of DW followed by a 4 hours treatment in the ultrasonic bath.

3.2.2 Structural Characterization of GO

3.2.2.1 Thermogravimetric analysis (TGA)

Thermogravimetric analysis (TGA) has appeared as powerful technique to monitor physical and chemical changes in materials. Fundamentally, this method consists in the measurement of the weight loss as a function of temperature or time. The samples are loaded in a suspended sensitive electronic balance and placed in a furnace, and the weight change is recorded while the sample is subjected to a programmed heating sequence. Usually the samples are analyzed from room temperature to above its decomposition temperature [9].

One of the most important applications of TGA is the assessment of the thermal stability of a material, which is important to compare different materials or to predict the materials lifetime. It can be also used to determine moisture, volatile, and filler contents [9]. The obtained curve can be plotted as result of the mass loss as a function of temperature or in differential way where the change in mass with time is plotted as a function of temperature [10].

To evaluate the thermal stability of o-EG and o-MWNT powder, TGA analysis were performed in Q500 equipment (TA Instruments, USA). 4 mg of o-GF and o-GNR powder were poured in aluminum pans and investigated under a nitrogen atmosphere with a temperature range of 40 °C - 800 °C. The experiments were run at a scanning rate of 10 °C/min.

3.2.2.2 Raman spectroscopy

Raman spectroscopy has emerged as an appealing technology for carbon materials characterization, once it is a fast and nondestructive analytical technique that provides a vibrational spectrum, containing physical and chemical information with high resolution [11, 12].

The basic mechanism principles rely on the inelastic monochromatic light scattering. Normally, when a molecule is irradiated by a monochromatic light, two different types of scattering are observed: elastic and inelastic scattering. In the first case, when the photon interacts with the

molecule and the exchange of energy is zero, the frequency of the scattered photon remains the same and no shift in the frequency is observed, elastic or Rayleigh scattering. In contrast, when the photon gains (anti-Stokes Raman scattering) or loses vibrational energy (Stokes Raman scattering) when in contact with the molecule, the inelastic scattering is accompanied by a photon frequency shift [12, 13].

To evaluate the physical properties and in particular to verify if the oxidation process was successfully achieved, pristine graphite, pristine MWNTs, o-EG and o-MWNT powder were placed over a glass coverslip and analyzed on a LabRAM HR Evolution raman spectrometer (Horiba Scientific, Japan) under a wavelength of 532 nm. The results treatment was performed by LabSpec6 *software*.

3.2.2.3 Ultraviolet-visible (UV-Vis) spectroscopy

The Ultraviolet-Visible (UV-Vis) spectroscopy is a technique used in chemistry, physics and biochemistry for organic molecules structural analysis but also as a tool for determination of the solutions concentration. This technique applies a wavelength ranging from 200-800 nm and typically the apparatus is made by: an UV visible light source; a cell through the light passes; and a detector to analyze the light capable of through the solution. Depending on the system, two approaches can be performed: one where the beam splits into two, passing through the cell containing the solution and the other one through the cell with solvent; or a system where only one beam is used and so, it is necessary to first measure the absorption of the solvent and afterwards the absorbance of the solution [4]. This last approach is the one used in this work.

The detector measures the absorbance based on the relationship between the intensity transmitted through the solvent alone (I_0) and the intensity of light transmitted through the cell with the solution (I), as demonstrated by the following equation (1) [4].

$$A = \log \frac{I_0}{I} \quad (1)$$

Regarding the concentration analysis, the Beer-Lambert law (equation (2)) where the absorbance (A) is directly proportional to the concentration (C), the width of the cell (l) and the absorptivity coefficient (ϵ), can be used.

$$A = \epsilon l C \quad (2)$$

Although, this formula is a limiting law for dilute solutions, once the absorptivity coefficient (ϵ) is independent of the concentration at the given wavenumber only when the absorbance (A) is lower than 1. For above values the absorptivity coefficient is no longer constant [5].

In view of the above considerations, UV-vis spectroscopy was performed to quantify the o-GF and o-GNR concentration present in solution. For this purpose, a UV-2401 PC equipment (Shimadzu, Japan) with quartz cells was used and several dilutions were performed to obtain a non-saturated spectrum.

3.2.2.4 Fourier transform infrared (FTIR) spectroscopy

The Fourier transform infrared (FTIR) spectroscopy is a standard method of materials analysis which provides information about the vibration of atoms in a compound. This method is widely used due to its low cost, consistency of results and ease of use characteristics. Usually, the FTIR equipment is composed by an interferometer which owns a semitransparent moving mirror (beam splitter) that splits every frequency into distinct beams. One direct to the sample and the other to the system. The obtained attenuation beam is expressed in time domain and it is converted to frequency domain using Fourier transform algorithm [6].

The FTIR analysis can be performed in: transmission, where a transparent matrix to the infrared (IR) beam, such as KBr, NaF₂ or CaF₂ is used and regarding the attenuation of the beam after passing the sample an absorption pattern for the whole mid-infrared spectroscopy region is obtained; in reflection mode, useful for in situ analysis of materials that strongly absorbed the IR radiation and when the surface of the sample needs to be analyzed [7]; and finally, the attenuated reflection mode (ATR) that uses the total reflection angle to further investigate the chemical composition of smooth surfaces [6, 8].

Therefore, FTIR analysis were performed in 4100 FTIR Spectrometer (Jasco, Japan) for o-GFs and o-GNRs characterization. For that, the solutions were drop-by-drop added to a CaF₂ substrate and the water was evaporated in a hot plate. 32 spectral scans were repeated and collected under the wave number range from 500-4500 cm⁻¹.

3.2.2.5 Zeta potential

When particles are in contact with aqueous solutions it is formed an interfacial charge that leads to the rearrangement of the free ions in the solution. The formation of this interface is usually

named as electrical double layer (EDL). In the EDL, it is possible to find a thin layer of immobile counterions, next to the solid surface, called the compact layer or Stern layer, and a mobile layer formed by co-ions designed as diffuse layer [14, 15]. As the particles move through the solution, due to gravity or some applied potential, the ions move with it. At some distance, in the diffuse layer, there is a boundary where above that the ions do not move with the particle, the slipping plane. The zeta potential (ζ) is the electrostatic potential at the slipping plane.

Regarding the above information, and in order to select the suitable material for the assembly of o-GNR and o-GF layers, three zeta potential measurements of the later solutions were performed in a Zetasizer Nano-Zs equipment (Malvern Instruments, UK). The presented results are the average of these measurements.

3.2.3 Production of the FS Multilayered Membranes

In order to produce FS membranes it was important to prepare polyelectrolytes solutions. The CHI solution was prepared dissolving and stirring over-night purified CHI of medium molecular weight in DW and 1% (v/v) acetic acid. The acetic acid added in this solution plays an important role in this reaction, once chitosan is neither soluble in neutral nor in basic conditions. CHI is polycation at a pH bellows its pKa [16] and adding this acid allows to protonate the free amino groups. Regarding the ALG solution, sodium alginate was dissolved in DW and stirred over-night. Both solutions were prepared with a concentration of 2 mg/mL and the pH value was corrected to 5.5 using 0.5M HCl and 0.5M NaOH.

The previous aqueous solutions of o-GF and o-GNR, with a concentration of 0.25 mg/mL, were also pH calibrated but for a basic value of 8. This value was established after an optimization process where it was verified that this is the pH where the solutions were completely stable and no deposition of the o-GF and o-GNR occurred. The pH calibration was also performed using 0.5M HCl and 0.5M NaOH.

To build-up the (CHI/ALG/CHI/o-GF)₁₀₀ and (CHI/ALG/CHI/o-GNR)₁₀₀ FS multilayered membranes, it was used a polypropylene (PP) support. These supports were rinsed with ethanol and DW and dried with a nitrogen flow before each use.

The assembling of each layer was achieved by alternating deposition of the support in different solutions to form 100 (tL) tetra layers made of CHI, ALG, CHI and GO which was accomplished using a dipping robot designed to perform this particular technique. The PP substrates were firstly dipped in the CHI solution for 6 min then rinsed in an aqueous solution (both

at pH 5.5) for 4 min. Subsequently, they were immersed in ALG solution (pH 5.5) for 6 min followed by rinsing in aqueous solution for 4 min at pH 5.5. An empty cup was placed in the seventh position to minimize the changing of solutions pH between the PE and the GO solutions. Then, the substrates were immersed into a GO solution (o-GF or o-GNR at pH 8) for 6 min and rinsed with an aqueous solution at pH 8 during 4 min. Figure 3.3 illustrates the steps and solutions positions to assemble the different layers.



Figure 3.3 Schematic representation of the LbL processing. **(a)** Methodology used to produce $(\text{CHI}/\text{ALG}/\text{CHI}/\text{o-GF})_{100}$ or $(\text{CHI}/\text{ALG}/\text{CHI}/\text{o-GNR})_{100}$ where **1** and **5**: CHI solutions (2 mg/ml; pH=5.5); **2**, **4** and **6**: washing solutions (DW; pH=5.5); **3**: ALG solution (2 mg/ml; pH=5.5); **7**: empty cup; **8**: o-GF or o-GNR solutions (0.25 mg/ml; pH=8); **9**: washing solutions (DW; pH=8). **(b)** Methodology used to produce $(\text{CHI}/\text{ALG}/\text{CHI}/\text{ALG})_{100}$, where **1** and **5**: CHI solutions (2 mg/ml; pH=5.5); **2**, **4** and **6**: washing solutions (DW; pH=5.5); **3**: ALG solution (2 mg/ml; pH=5.5); **7**: empty cup; **8**: ALG solution (2 mg/ml; pH=5.5); **9**: washing solutions (DW; pH=5.5).

Control FS membranes with the same number of layers were also built-up only with CHI and ALG. Figure 3.3 b) illustrates the procedure used to achieve $(\text{CHI}/\text{ALG}/\text{CHI}/\text{ALG})_{100}$. The performed steps were similar to the previous, although instead of o-GFs and o-GNRs, ALG was used.

At the end of the process the membranes were collected and dried inside a plastic flask to minimize the shrinkage phenomenon. After drying, the membranes were easily detached from the substrate and kept for further analysis.

3.2.4 FS Multilayered Membranes Characterization

3.2.4.1 Scanning electron microscopy (SEM)

Scanning electron microscopy (SEM) is an outstanding technique used nowadays for scientific research. Its high resolution, combined with great ability of depth focus and X-ray analysis makes it a distinct technique to observe microscopic structures as well as phases from different materials, especially in the materials science field [20].

The operating system is based on the irradiation of a desirable area with an electron beam that will swept the surface of specimen. When the beam reaches the sample, different signals are generated, including secondary electrons, backscattered electrons, Auger electrons and characteristics X-rays. In the specific case of SEM, secondary and backscattered electrons are extremely important once they vary with the topography of the material and so composition and surface topography can be studied [21].

Regarding the above information, the morphology of the free-standing membranes was characterized, on both sides, using a JSM-6010LV SEM (JEOL, Japan). Before each analysis, the samples were sputtered with a gold layer, using a sputter coater EM ACE600 (Leica Microsystems, Germany). For the observation of the cross-section, the detached membranes were fractured using nitrogen.

3.2.4.2 Atomic force microscopy (AFM) imaging

The atomic force microscopy (AFM) has appeared as a nondestructive tool capable of probing the local properties of materials surface, including imaging of surfaces and force measurements, with atomic scale [22].

Regarding the AFM apparatus, five essential components are found, including: an AFM probe, which consists in a sharp tip at the end of a cantilever; an optical laser, for cantilever deflections measuring; a piezoelectric scanner that moves the tip along the sample; a feedback system that monitors the forces between the tip and the molecules on the materials surface; and finally a conversion system from raw data into an image, see Figure 3.4.

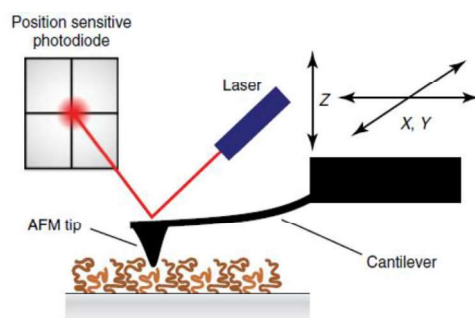


Figure 3.4 Schematic representation of AFM system [22].

The interaction of the tip with the surface when close or in mechanical contact results into mechanical deflections of the cantilever, which is detected optically by the laser. The detector converts these deflections into voltages signals, which are continuously recorded. Depending on the operation mode, different features can be analyzed, for instance the topography can be assessed through the contact or tapping mode, and the mechanical properties through the dynamic force mode [22].

For topography and roughness analysis, dried FS membranes were imaged using a Dimension Icon AFM equipment (Bruker, France) with an air cantilever (SNL-10D) (Bruker, France) with a spring constant of 0.06 N/m, operating in a ScanAsyst mode.

The topography of the membranes was analyzed with 512×512 pixels² at line rates of 1Hz and for surface roughness analysis, AFM images with $5 \times 5 \mu\text{m}^2$ were obtained, followed by root mean squared roughness (R_{RMS}) and average height value (H_{av}) calculation. The analysis of the images was performed using NanoScope Analysis *software* and at least three measurements were done.

3.2.4.3 Raman mapping

To evaluate the presence and distribution of o-GF and o-GNR along the CHI/ALG free-standing membranes, Raman spectroscopy was performed. Through this technique, Raman maps or images were obtained, placing the membranes on a glass coverslip and taking a series of Raman point measurements in the area depicted in the video image.

The equipment was the same as the one used previously for graphene characterization, although with an excitation source of 785 nm and with 100x objective lens. The spectra were recorded at room temperature and the final results were analyzed with a LabSpec6 *software*.

3.2.4.4 TGA measurements

TGA studies were performed to quantify the filler amount in the membranes, in particular the amount of o-GF and o-GNR assembled during the LbL process.

A Q500 equipment (TA Instruments, USA) was used and the samples mass was ≈ 4 mg. The process undergone using a nitrogen atmosphere with a temperature range between 40°C and 800°C . The experiments were run at a scanning rate of $10^{\circ}\text{C}/\text{min}$ and at least 3 measurements were performed.

3.2.4.5 Water contact angle (WCA) measurements

The interface water/material represents an important characteristic in many applications, including in biological and technological systems [23]. This feature is extremely affected by several factors such as: curvature, roughness and chemistry of the surface. Depending on the application, different behaviors can be desirable, for instance, hydrophilic surfaces are preferred for cell attachment and proliferation, and in turn, hydrophobic surfaces can be wanted for self-cleaning materials [24].

One of the most used techniques to evaluate the materials wettability is the water contact angle (WCA) measurement. This angle is obtained by the Young's equation and its measurement is made between the surface of the material and the line tangent to the droplet radius from the point where the material contacts with the drop [25].

Depending on the WCA value, different behaviors are seen. Typically, for a WCA lower than 90° , a spreading of the drop is seen on the surface and the material is described as hydrophilic. When it gets higher than 90° , a hydrophobic character is shown, and so the droplet tends to bead or shrink away from the surface-Figure 3.5.

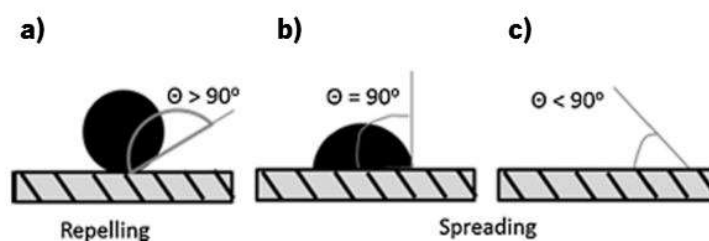


Figure 3.5 Schematic representation of contact angle measurements on a solid surface. **(a)** Hydrophobic surface; **(b)** and **(c)** hydrophilic surfaces [25].

Considering the last information, the wettability of the surfaces was evaluated by water contact angle measurements. For that, an OCA15plus goniometer equipment (DataPhysics, Germany) was used and at least three measurements of each condition were performed on each membrane surface. The measurements were achieved after a motor-driven syringe dispensed 5 μ l of distilled water, at room temperature and the pictures were taken as the drop contact the surface. The results treatment was performed by SCA20 *software*.

3.2.4.6 Water uptake (WU)

Water uptake (WU) is an important method to characterize biomaterials. This process is affected by several factors, such as: density, physical state and glass transition temperature (T_g) of the polymer [26]. Regarding the multilayered systems, WU is also dependent of the chemical characteristics of each layer and on the layer position in the system, being the interface an important factor for water transport [27]. This phenomenon affects several features of the materials, including: degradation, swelling, mechanical properties, biological response and drug release [26].

Therefore, the produced free-standing membranes were physical characterized in terms of water uptake by soaking dry membranes, previously weighed, in PBS (Sigma, USA) at 37°C for 5 min, 15min, 30min, 1h, 3h, 5h, 7h, 24h and 48h. After each time point, the membranes were taken from the PBS solution and the excess was removed with a filter paper. The FS membranes were then weighed. To quantify the water uptake, Equation (3) was used:

$$\text{Water uptake (\%)} = \frac{W_w - W_d}{W_d} \times 100 \quad (3)$$

where W_w is the weight of the membranes in the swollen state and W_d is the weight in dry conditions.

3.2.4.7 Weight loss

When implanted in the human body and until no longer needed, a biomedical device should maintain its properties, being then degraded, absorbed, and excreted. Typically, the hydrolysis of a semi crystalline polymer occurs in two different phases. Initially, the water penetrates the bulk of

the material, attacking the chemical bonds in the amorphous phase and in a second phase, enzymatic attack of the fragments occurs, leading to the mass loss of the polymer [28].

Pre-weighed membranes were soaked in a phosphate buffer saline solution (PBS), pH=7.4, with sodium azide (0.02% w/v) as well as in a PBS solution with lysozyme in a concentration of 0.013mg/ml, for 0, 1, 3, 7, 14 and 21 days, at 37°C. After each time point, the samples were removed from the solution, washed with distilled water and dried. The weight loss quantification was calculated following Equation (4):

$$\text{Weight loss (\%)} = \frac{(W_i - W_f)}{W_i} \times 100 \quad (4)$$

where W_i is the initial dry weight of the sample and W_f is the final dry weight of the sample, at a certain time point. Each experiment was repeated three times and the average value was taken as the weight loss.

3.2.4.8 Mechanical characterization

3.2.4.8.1 *Tensile testing*

The behavior of a biomaterial under loading is particularly important for the applications success, once a major cause of failure is related with the mechanical mismatch between the graft and the host tissue. One of the most important and primary tests for evaluation of the mechanical properties is the tensile testing. Typically, in this test a strip with a uniform length (L) is subjected to an axial load (P) and the strength of interest may be measured in terms of either the stress necessary to cause plastic deformation or the maximum stress that the material can withstand [17].

The produced membranes were subjected to tensile tests using a universal mechanical testing equipment (Instron 5543, USA). Specimens were cut into a rectangular shape (5×20 mm²) and measurements were taken using a 1kN load cell under a loading speed of 1 mm/min and a gauge length of 10 mm. At least five samples were tested, for each composition, in order to calculate the mean and standard deviation value of the ultimate tensile strength and strain at failure.

3.2.4.8.2 Dynamic mechanical analysis (DMA)

Different techniques can be used to mechanically test polymeric materials, including dynamic mechanical analysis (DMA). This technique is known for being a nondestructive method, where the viscoelastic properties of the material can be investigated through the application of an oscillatory stress to the sample, and the resulting strain is determined as function of frequency and/or temperature [18].

Typically a viscoelastic polymer is characterized for showing an elastic and viscous behavior, where the applied stress is proportional to strain and rate of strain. Regarding these materials two compartments can be seen: (i) following the application of a constant stress, the strain is not constant but it continues to deform with the time; (ii) during this process the material may store energy to recover its initial shape [18].

Due to the presence of elastic and fluid behaviors, a complex modulus may be defined-equation (5).

$$E^* = \frac{\sigma_0}{\varepsilon_0} (\cos(\delta) + i \sin(\delta)) \quad (5)$$

where, $E' = \frac{\sigma_0}{\varepsilon_0} (\cos(\delta))$ is referred as a storage modulus representing the energy stored in the sample per cycle and $E'' = \frac{\sigma_0}{\varepsilon_0} (\sin(\delta))$ is the loss that represents the energy loss per cycle [19].

The DMA experiments were performed using a Tritec 2000B equipment (Triton Technology, UK). The membranes were cut with 5 mm width and 20 mm length, and the thickness was determined in three different points of each sample, using a micrometer. Previously to the DMA tests, the samples were soaked overnight, in a PBS solution, to reach the equilibrium, and after that, the measurements were carried out at 37°C with total immersion of the sample in a reservoir containing PBS. The experiments were carried out using a stress mode cycle of increasing frequency starting at 0.1 Hz and ending at 15 Hz.

3.2.4.9 Cellular assays

The *in vitro* biocompatibility assessment of materials is important to study the behavior of cells to a particular topography, chemistry or surface activity. Concerning the cell viability, proliferation, rate of adhesion, changes in cellular morphology and retention of phenotype, different

findings can be achieved to evaluate the direct or indirect toxic effects of the material [29]. Here, it was explored some of the standard tests to perform this assessment and which are important to understand the interaction between the produced FS membranes and cells.

3.2.4.9.1 *Cell culture and seeding*

L929 mouse fibroblasts line (L929, European Collection of Cell Cultures) was used to test the *in vitro* biocompatibility of the (CHI/ALG/CHI/ALG)₁₀₀, (CHI/ALG/CHI/o-GF)₁₀₀ and (CHI/ALG/CHI/o-GNR)₁₀₀ membranes for 1, 3 and 7 days.

Cells were cultured in complete Dulbecco's modified minimum essential medium (DMEM) medium supplemented with 3.7 g/L sodium bicarbonate, 10% FBS and 1% penicillin-streptomycin (pH 7.4), in 150 cm² tissue culture flasks and incubated at 37 °C in a humidified air atmosphere of 5% CO₂. Every 2-3 days the medium was replaced. Prior to cell seeding, samples with 10 x 10 mm² were sterilized by immersion in 70% (v/v) ethanol for 2h and then washed twice with sterile phosphate buffered saline (PBS). After this step, the membranes were immersed in cell culture medium for complete swelling. The cells were seeded in the membranes (in triplicate) at a density of 50 000 cells/sample and nourished with DMEM. The cultures were incubated at 37 °C in a humidified air atmosphere of 5% CO₂.

3.2.4.9.2 *DAPI-phalloidin staining*

In order to determine the morphology and viability of the cells, fluorescence staining was performed with phalloidin tetramethylrhodamine and 4',6-diamidino-2-phenylindole (DAPI). Phalloidin is a small toxin that can easily penetrate into densely packed actin network and which is able to bind to actin and prevent its depolymerization, making it an ideal probe for detection of cytoskeleton [31]. In turn, DAPI is able to strongly bind to adenosine and thymidine regions of nuclear DNA, and when bounded it fluoresces due to the inhibition of internal rotation in DAPI's molecular structure [32].

At each time point DAPI (20 mg/mL, Sigma Aldrich, USA) and phalloidin (20 mg/mL, Sigma Aldrich, USA) were used. Prior to staining, culture medium was removed and the membranes were washed with sterile PBS. Formalin (10%, ThermoFisher) was added for 30 min, to fix the cells above the samples. After that, formalin was removed and the samples were washed with PBS. Following this, 1 mL of PBS with 10 µL of phalloidin was added and kept at room temperature, protected from light, during 45 minutes. Subsequently, the samples were washed with PBS and

stained with 1 μ L of DAPI in 1 mL of PBS for 15 minutes. After 15 minutes, the samples were washed with PBS and images were obtained using inverted fluorescence microscope (Zeiss, Germany).

3.2.4.9.3 *MTS assay*

Different types of tetrazolium compounds have been used to assess the metabolic activity and to detect viable cells, including 3-(4,5-dimethylthiazol-2-yl)-5-(3-carboxymethoxyphenyl)-2-(4-sulfophenyl)-2H-tetrazolium (MTS). The reduction of this compound in the presence of phenazine methosulfate (PMS) results in a brown water soluble formazan product, that in PBS presents an absorbance peak at 490-500 nm. Measuring the amount of the formed product it is possible to obtain a relative quantification of the cells number, once the product is proportional to the number of cells [30].

In this work, a MTS colorimetric assay (Cell Titer 96 AQueous One Solution Cell Proliferation Assay, Promega, USA) was used. At each time point the samples were washed with PBS and then immersed in a MTS solution, prepared by using a 1:5 ratio of MTS reagent and serum free cell culture medium. After immersing the samples were incubated in this solution for 3h at 37 °C with a humidified atmosphere containing 5% CO₂. Afterwards, 100 μ L (in triplicate) of each well were transferred to a new 96-well plate and finally the optical density (OD) was read at 490 nm on a multiwell microplate reader (Synergy HT, Bio-Tek Instruments). All cytotoxicity tests were conducted by using three replicates.

3.2.4.9.4 *DNA quantification*

The seeding efficiency and proliferation of cells into the developed membranes was investigated through the quantification of double-stranded DNA (dsDNA). At each time point and using the PicoGreen dsDNA kit (Life Technologies, UK), the DNA was quantified. Initially, cells were lysed by osmotic and thermal shock and consecutively the recovered supernatant was read on a microplate reader (BioTek, USA) using a 485 and 528 nm as excitation and emission wavelengths, respectively. Triplicates were performed for each sample and the DNA amounts were calculated using a standard curve.

3.3 Statistical Analysis

Data were expressed as average \pm standard deviation (SD) of at least three replicates. Normality tests were performed using Shapiro-Wilk tests. Depending if the population was normally distributed or not, parametric or nonparametric were used, respectively. For the tensile tests and AFM assays the population was normally distributed and One way Anova followed by Tukey's test was used. In the particular case of the cellular assays, Two way Anova was used. For WCA assays where the population was not normally distributed Kruskal–Wallis test was employed. The statistical analysis was performed using the *software* GraphPad Prism 6.0 for Windows. Statistical significance was accepted for a (*) $p < 0.05$. The error bars denote the standard deviation.

3.4 References

- [1] Chen J, Yao BW, Li C, Shi GQ. An improved Hummers method for eco-friendly synthesis of graphene oxide. *Carbon*. 2013;64:225-9.
- [2] Sorokina NE, Khaskov MA, Avdeev VV, Nikol'skaya IV. Reaction of graphite with sulfuric acid in the presence of KMnO₄. *Russian Journal of General Chemistry*. 2005;75:162-8.
- [3] Kosynkin DV, Higginbotham AL, Sinitskii A, Lomeda JR, Dimiev A, Price BK, et al. Longitudinal unzipping of carbon nanotubes to form graphene nanoribbons. *Nature*. 2009;458:872-U5.
- [4] Anderson R, Bendell D, Goundwater P. *Organic Spectroscopy Analysis*. Royal Society of Chemistry; 2004. p. 176.
- [5] Perkampus H. *UV-VIS Spectroscopy and Its Applications*. 1 ed: Springer Berlin Heidelberg; 1992. p. 244.
- [6] Schmitt J, Flemming HC. FTIR-spectroscopy in microbial and material analysis. *International Biodeterioration & Biodegradation*. 1998;41:1-11.
- [7] Ricci A, Olejar KJ, Parpinello GP, Kilmartin PA, Versari A. Application of Fourier Transform Infrared (FTIR) Spectroscopy in the Characterization of Tannins. *Applied Spectroscopy Reviews*. 2015;50:407-42.
- [8] Stuart B. *Infrared Spectroscopy: Fundamentals and Applications*. John Wiley & Sons; 2004. p. 242.
- [9] Lampman S. *Characterization and Failure Analysis of Plastics*. ASM International; 2003. p. 489.
- [10] Stuart BH. *Polymer Analysis*. John Wiley & Sons; 2002. p. 279.
- [11] Kudelski A. Analytical applications of Raman spectroscopy. *Talanta*. 2008;76:1-8.
- [12] Das RS, Agrawal YK. Raman spectroscopy: Recent advancements, techniques and applications. *Vibrational Spectroscopy*. 2011;57:163-76.
- [13] Efremov EV, Ariese F, Gooijer C. Achievements in resonance Raman spectroscopy review of a technique with a distinct analytical chemistry potential. *Analytica Chimica Acta*. 2008;606:119-34.
- [14] Kirby BJ, Hasselbrink EF. Zeta potential of microfluidic substrates: Theory, experimental techniques, and effects on separations. *Electrophoresis*. 2004;25:187-202.
- [15] Sze A, Erickson D, Ren LQ, Li DQ. Zeta-potential measurement using the Smoluchowski equation and the slope of the current-time relationship in electroosmotic flow. *Journal of Colloid and Interface Science*. 2003;261:402-10.
- [16] Martins AF, Facchi SP, Follmann HDM, Pereira AGB, Rubira AF, Muniz EC. Antimicrobial activity of chitosan derivatives containing n-quaternized moieties in its backbone: a review. *International Journal of Molecular Sciences*. 2014;15:20800-32.
- [17] David J. *Introduction to Tensile Testing*. 2nd ed: ASM International; 2004. p. 283.
- [18] Jones DS. Dynamic mechanical analysis of polymeric systems of pharmaceutical and biomedical significance. *International Journal of Pharmaceutics*. 1999;179:167-78.
- [19] Menczel J, Prime RB. *Thermal Analysis of Polymers: Fundamentals and Applications*. Wiley; 2009.
- [20] Michler G. *Electron Microscopy of Polymers*. Springer Science & Business Media; 2008. p. 473.

- [21] Goldstein J. Scanning Electron Microscopy and X-Ray Microanalysis: A Text for Biologists, Materials Scientists, and Geologists Plenum Press; 1992. p. 820.
- [22] Trache A, Meininger GA. Atomic force microscopy (AFM). Current protocols in microbiology. 2008;Chapter 2:Unit 2C.
- [23] Giovambattista N, Debenedetti PG, Rosky PJ. Effect of surface polarity on water contact angle and interfacial hydration structure. Journal of Physical Chemistry B. 2007;111:9581-7.
- [24] Tang ZY, Wang Y, Podsiadlo P, Kotov NA. Biomedical applications of layer-by-layer assembly: From biomimetics to tissue engineering. Advanced Materials. 2006;18:3203-24.
- [25] Kaur S, Sundarrajan S, Rana D, Sridhar R, Gopal R, Matsuura T, et al. Review: the characterization of electrospun nanofibrous liquid filtration membranes. Journal of Materials Science. 2014;49:6143-59.
- [26] Valenzuela LM, Michniak B, Kohn J. Variability of water uptake studies of biomedical polymers. Journal of Applied Polymer Science. 2011;121:1311-20.
- [27] Baukh V, Huinink HP, Adan OCG, Erich SJF, van der Ven LGJ. Water-Polymer Interaction during Water Uptake. Macromolecules. 2011;44:4863-71.
- [28] Middleton JC, Tipton AJ. Synthetic biodegradable polymers as orthopedic devices. Biomaterials. 2000;21:2335-46.
- [29] Di Silvio L. Cellular response to biomaterials. In: Gurav N, Di Silvio L, editors. Biocompatibility of degradable polymers for tissue engineering: Woodhead Publishing Series in Biomaterials 2009. p. 648.
- [30] Cory AH, Owen TC, Barltrop JA, Cory JG. Use of an aqueous soluble tetrazolium formazan assay for cell-growth assays in culture. Cancer Communications. 1991;3:207-12.
- [31] Wehland J, Osborn M, Weber K. Phalloidin-induced actin polymerization in cytoplasm of cultured-cells interferes with cell locomotion and growth. Proceedings of the National Academy of Sciences of the United States of America. 1977;74:5613-7.
- [32] Tarnowski BI, Spinale FG, Nicholson JH. DAPI as a useful stain for nuclear quantitation. Biotechnic & histochemistry : official publication of the Biological Stain Commission. 1991;66:297-302.

CHAPTER 4. FREE-STANDING

MULTILAYERED MEMBRANES BASED ON GRAPHENE AND NATURAL POLYMERS FOR BIOMEDICAL APPLICATIONS

4. FREE-STANDING MULTILAYERED MEMBRANES BASED ON GRAPHENE AND NATURAL POLYMERS FOR BIOMEDICAL APPLICATIONS

Duarte Moura^{1,2}, Sofia G. Caridade^{1,2}, Maria P. Sousa^{1,2}, Eunice Cunha³, João F. Mano^{1,2}, Maria C. Paiva³, Natália M. Alves^{1,2}.

¹ 3B's Research Group, Biomaterials, Biodegradables and Biomimetics, University of Minho, Headquarters of the European Institute of Excellence on Tissue Engineering and Regenerative Medicine, AvePark-Parque de Ciência e Tecnologia, 4805-017 Barco, Taipas, Guimarães, Portugal.

² ICVS/3B's, Associate PT Government Laboratory, Braga/Guimarães, Portugal.

³ Institute for Polymers and Composites/13N, Department of Polymer Engineering, University of Minho, 4800-058 Guimarães, Portugal.

Abstract

Carbon-based nanomaterials such as graphene oxide (GO) have been considered promising candidates as nanocomposites fillers, not only due to their outstanding mechanical properties, but also owing to the great potential to provide essential chemical and physical properties. Due such interesting properties we propose herein to develop new free-standing (FS) membranes based on chitosan, alginate and GO through layer-by-layer assembly. First, the GO was synthesized from graphite and multi-walled carbon nanotubes using a modified Hummer's method that resulted in oxidized graphene flakes (o-GF) and oxidized graphene nanoribbons (o-GNR), respectively. In a first step, the structures and properties of both o-GF and o-GNR were characterized. Afterwards, FS membranes were produced and their morphological, thermal, mechanical properties and the GO dispersion along the membranes were assessed. Moreover, their degradation and swelling profiles were evaluated as well as their biological behavior. The results from the first studies showed that both graphite and nanotubes were successfully oxidized, revealing the bonding of oxygen containing groups, such as hydroxyl and carbonyl groups. Concerning the FS membranes, the addition of o-GF and o-GNR resulted in rougher membranes with an hydrophilic behavior. The mechanical analysis revealed a significant increase in both the elastic modulus and the ultimate tensile strength. Thermogravimetric analysis showed that the presence of o-GF or o-GNR did not change the thermal stability of the membranes. The biological assays revealed that the addition of o-GF resulted in membranes with enhanced cytocompatibility. Therefore, GO reinforced membranes show potential for biomedical applications, in particular, o-GF membranes for wound healing, cardiac and bone engineering applications.

Keywords: Graphene Oxide; Chitosan; Alginate; Free-standing membranes; Biomedical applications

Graphene is a monolayer of sp^2 bonded carbon atoms, arranged in an hexagonal lattice, with a bond length of 0.142 nm [1]. This material is the building block of other carbon allotropes such as nanotubes and graphite [2], and it was found to have an elastic modulus of approximately 1 TPa, an intrinsic electrical conductivity of $6 \times 10^5 \text{ S.m}^{-1}$, a thermal conductivity of $5.1 \times 10^3 \text{ W.m}^{-1}.\text{K}^{-1}$ and a theoretical specific area of $2630 \text{ m}^2.\text{g}^{-1}$ [3-5]. Due to the aforementioned characteristics, graphene and its derivatives have been further explored for a wide range of applications in the biomedical field, such as biosensing [6, 7], drug and gene delivery [8, 9], and tissue engineering [10, 11].

Graphene oxide (GO), including oxidized graphene flakes (o-GF) and oxidized graphene nanoribbons (o-GNR), is one of the most cost-effective and large scale derivatives obtained through the oxidation process of graphite and multi-walled nanotubes (MWNTs), and which is capable of generating graphene after undergoing a reduction process [12]. Although a precursor of graphene, GO by itself also shows remarkable features including: a hydrophilic behavior and solubility in water and polar solvents [13, 14], low nanotoxicology [15], a large specific surface area and a large concentration of functional groups [16] such as epoxy, hydroxyl, carboxyl and carbonyl groups [14, 16, 17]. The presence of these groups represents a major advantage for the interfacial interaction between GO and the polymer chosen for producing nanocomposites, resulting in a strong and revolutionary nanocomposite material, particularly when the nanofiller is homogeneously dispersed in the polymeric matrix [18]. Graphene and GO have revealed to be promising materials for biomedical applications, providing physical and chemical conditions for the development of new tissues capable to influence the proliferation and differentiation of different cells, mimicking the structure and function of the extracellular matrix [19, 20].

Natural polymers have been explored and used for health care applications due to their great similarity with the extracellular matrix (ECM) and biodegradability properties [21, 22]. Chitosan (CHI), a linear and semi-crystalline natural-derived polysaccharide obtained from the N-deacetylation of chitin which major sources are different biological structures such as the exoskeleton of insects and crustaceans, reveals a nontoxic, antibacterial, antifungal, mucoadhesive, haemostatic and biocompatible behavior [23-26]. Apart from CHI, alginate (ALG) is also one of the most investigated biomaterials. In fact, this natural polysaccharide is hydrophilic, biocompatible and non-immunogenic, with the ability to absorb 200 to 300 times more water than its own weight [27, 28]. Because of that, both materials are widely explored for biomedical

purposes [29-32], including as wound dressing materials [33], drug release vehicles [34], and as extracellular matrix models for biological studies [16].

Layer-by-Layer (LbL) assembly has emerged as a simple and environmental technique to obtain materials with a nanometer and micrometer scale control of the size, morphology and molecular structure [35, 36]. This method is based in a sequential adsorption of oppositely charged macromolecules on a substrate surface, via electrostatic or non-electrostatic forces, which includes hydrophobic interactions, hydrogen bonds, van der Waals forces, charge transfer interactions and covalent bonds [37]. Depending on the substrate, different structures may result, including free-standing membranes (FS). Using substrates with low surface energy has revealed to be a versatile approach to achieve robust multilayer FS membranes without using any sacrificial or dissolution layer [35]. The use of these two biopolymers for FS membranes production has been studied by several authors. Martins *et al.* have shown the ability to produce biocompatible CHI/ALG nanolayered films through LbL [38]. Caridade *et al.* have developed FS membranes based in ALG and CHI [39], able to be loaded with bone morphogenetic protein 2 [40].

One of the major drawbacks of natural polymers is their low mechanical performance. GO has emerged as an inorganic filler capable to provide a better mechanical performance when embedded in such polymeric matrixes. Ionita *et al.* reported a significant improvement in the mechanical and thermal degradation properties of ALG/GO films obtained by a solvent casting method, even for small amounts of GO (0.5 wt%) [16]. Cellulose/GO films obtained by LbL demonstrated good homogeneity, resulting in an increase of the hardness (263%) and Young modulus (111%) [36]. Justin *et al.* studied the effect of GO in a CHI polymeric matrix. These authors not only described an increase in the ultimate tensile strength, particularly for GO amounts between 0.25 wt% and 2 wt.% but also demonstrated an improvement of 72% on drug release when GO was combined with the drug [41]. Li *et al.* prepared genipin-cross linked CHI/GO films by solvent casting and found an enhancement of the mechanical and degradation properties along with an improved cytocompatibility with mouse preoblasts [42]. Although some works concerning the use of GO as reinforcement element of biopolymers have been published [16, 43], to the best of our knowledge this is the first time that natural polymers such as CHI and ALG were assembled with GO through the LbL technique to obtain FS membranes.

In the light of the above observations, the present study aims to develop (CHI/ALG/CHI/GO)₁₀₀ FS membranes through the LbL self-assembly technique where o-GF and o-GNR are used as nanofillers to reinforce the intrinsic properties of the polymeric matrix. Depending

on the filler, the produced FS membranes could be potentially used in different biomedical applications, namely for tissue engineering applications, wound healing, drug delivery or as non-adhesive substrates. Initially, the produced GO were characterized by Ultraviolet-Visible Spectroscopy (UV-Vis), Fourier Transform Infrared Spectroscopy (FTIR), Raman Spectroscopy and Thermogravimetric Analysis (TGA). The nanocomposite membranes were characterized by Scanning Electron Microscopy (SEM), Atomic Force Microscopy (AFM), TGA and Raman Mapping. The mechanical performance, wettability, water uptake, degradation and biological behavior of the obtained FS membranes were also explored.

4.1 Experimental Section

4.1.1 Materials

MWNTs (purity approx. 90%; average length=1.5 μm) were supplied by Nanocyl™ (Belgium) and exfoliated graphite (EG) (purity approx. 99.5%; average length=9.9 μm) was obtained from Nacional de Grafite Ltda. (Brazil). To covalently functionalize the surface of MWNTs and EG, a chemical oxidation process was applied using different reagents, including: sulfuric acid (H_2SO_4 ; 95-97%), potassium permanganate (KMnO_4) analytical reagent grade, hydrogen peroxide analytical reagent grade (H_2O_2 ; >30% w/v), hydrochloric acid (HCl ; 10% v/v), all purchased from Fisher Scientific (UK), and distilled water (DW). Regarding the production of the FS membranes, CHI (medium molecular weight) was purchased from Sigma-Aldrich (Germany), with a degree of N-deacetylation (DD) ranging from 75-85% and a viscosity of 200-800 cps. Prior to be used, the CHI was purified by a recrystallization process. Sodium alginate from brown algae (ALG) was purchased by Sigma-Aldrich, with a viscosity of 5 to 40 cps, and along with CHI it was used as polymeric matrix.

4.1.2 Synthesis of GO

O-GF were synthesized by a modified Hummers' method. Briefly, 400 mL of H_2SO_4 were added to 5 g of EG and stirred vigorously during 2 h, in an ice-bath. 25 g of KMnO_4 were slowly added to the previous solution and kept stirring overnight, at room temperature. Consecutively, the solution was transferred to an ice-bath and 300 mL of DW were slowly added. Then, 30 mL of H_2O_2 were added drop-by-drop and remained stirring for 30 min. o-GNRs were obtained by a similar process. 4 g of MWNTs were poured in 500 mL of H_2SO_4 and stirred for 4 h. Secondly, in an ice

bath, 32 g of KMnO_4 were slowly added and kept stirring for 2 h. The mixture was then heated up to 60 °C and stirred overnight. The same purification process was performed, including the addition of 300 mL of DW followed by 30 mL of H_2O_2 , all steps performed with the solution placed in an ice-bath. Afterwards, both solutions were poured into 45 mL tubes and centrifuged under 3500 rpm in a Labofuge 400 (Heraeus Instruments, USA), for 15 min and the supernatant was discarded. The precipitate was washed with DW for a total of 3 cycles. The resulting precipitate was then collected followed by the addition of 250 mL of HCl and it was left stirring for 15 min. The mixture was once again centrifuged and washed for 3 cycles. After the centrifugation procedure, the supernatant was discarded and DW was added to the solid part and then filtered with a nylon membrane filter (Whatman, UK). The solid was dried for 48 h at 100 °C and finally milled. It is important to notice that at this stage, the resultant powder consists of oxidized exfoliated graphite (o-EG) and oxidized multi-walled carbon nanotubes (o-MWNT), where the different layers of graphene were not completely separated. In order to achieve extensive exfoliation, o-EG and o-MWNT were dispersed in DW and submitted to 4 h ultrasound treatment in the ultrasonic bath, where exfoliation of the graphene layers was achieved resulting in o-GF and o-GNR from EG and MWNTs, respectively. The final suspensions had a concentration of 0.25 mg/mL and the pH value was adjust for a basic value of 8.

4.1.3 Structural Characterization of GO

4.2.3.1 Characterization of EG and MWNT submitted to the modified Hummers' method

In a first step, EG and MWNT synthesized by the modified Hummers' method were characterized by TGA and Raman spectroscopy. To evaluate the thermal stability of o-EG and o-MWNTs powders, TGA analysis were performed in Q500 equipment (TA Instruments, USA). The measurements were performed in a nitrogen atmosphere with a temperature ranging from 40 °C to 800 °C, and with a scanning rate of 10 °C/min. To verify if the oxidation process was successfully achieved, EG, MWNTs, o-EG and o-MWNTs powders were placed over a glass coverslip and analyzed on a LabRAM HR Evolution Raman spectrometer (Horiba Scientific, Japan) using a laser excitation wavelength at 532 nm. The results treatment was performed by LabSpec6 *software*.

4.2.3.2 Characterization of o-GF and o-GNR

For chemical characterization of the as-synthesized GO, UV-Visible spectroscopy (UV-vis.) was performed on o-GF and o-GNR solutions, using a UV-2401 PC spectrometer (Shimadzu, Japan) on quartz cells with 1 cm path length. Fourier Transform Infrared Spectroscopy (FTIR) analysis was performed on a 4100 FTIR Spectrometer (Jasco, Japan). For FTIR experiments, both o-GF and o-GNR solutions were drop-by-drop added to a CaF₂ substrate and placed in a hot plate to evaporate the water, and finally a powder form of each solution was achieved. The spectrum was obtained with 32 spectral scans per sample, repeated and collected under the wave number ranging from 500-4500 cm⁻¹. The stability of the GO solutions were assessed with a Zetasizer Nano-Zs equipment (Malvern Instruments, UK), and at least three zeta potential measurements were performed for each sample. The results presented are the average of these measurements.

4.1.4 Production of the Free-standing (FS) Multilayered Membranes

The production of the FS multilayered films was achieved on a polypropylene (PP) substrate. Prior to be used, each substrate was washed with DW and ethanol followed by drying them with a nitrogen flow. The polyelectrolyte solutions were prepared with a concentration of 2 mg/mL, at pH 5.5.

The assembling of each layer was achieved by alternate dipping of the support in the different polyelectrolytes (prepared freshly) and GO solutions to form 100 tetra layers (tL) of CHI/ALG/CHI/GO. The substrates were first dipped in the CHI solution for 6 min then rinsed in DW (both at pH 5.5) for 4 min. Subsequently, they were immersed in ALG solution (pH 5.5) for 6 min followed by rinsing in DW for 4 min at pH 5.5. After that, the substrate was dipped again in a CHI solution, rinsed with DW (using the same conditions as before) and let to dry at room temperature during 2 min. Then, the substrates were immersed into a GO solution (o-GF or o-GNR at pH 8) for 6 min and rinsed with DW at pH 8 during 4 min. This procedure was repeated using a home dipping robot until the deposit of 100 tL was achieved. These FS membranes will be named hereafter (CHI/ALG/CHI/o-GF)₁₀₀ and (CHI/ALG/CHI/o-GNR)₁₀₀. (CHI/ALG/CHI/ALG)₁₀₀ FS membranes were produced and used as controls. For that, the same procedure described above was used, although no layers of o-GFs or o-GNRs were assembled. The FS membranes were collected and dried inside a plastic flask to minimize the shrinkage phenomenon. After drying, the membranes were easily detached from the substrate and kept for further analysis.

4.1.5 Scanning Electron Microscopy (SEM) of the FS membranes

The morphologies of the FS membranes were characterized, on both sides, using a JSM-6010LV SEM (JEOL, Japan), operating at 15 kV accelerating voltage. Before each analysis, the samples were sputtered with a gold layer, using a sputter coater 108A (Cressington, UK). For the cross-section observations, the FS were dipped in liquid nitrogen and cryo-fractured, and the morphology of the material across the thickness was observed.

4.1.6 Atomic Force Microscopy (AFM) Imaging

For topography and roughness analysis, dried FS membranes were imaged using a Dimension Icon AFM equipment (Bruker, France) equipped with an air cantilever (SNL-10D) (Bruker, France) with a spring constant of 0.06 N/m, operating in a ScanAsyst mode. The topography of the membranes was analyzed with 512×512 pixels² at line rates of 1Hz and for surface roughness analysis. AFM images with $5 \times 5 \mu\text{m}^2$ were obtained, followed by root mean squared roughness (R_{rms}) and average height value (H_{av}) calculation. The analysis of the images was performed using NanoScope Analysis *software* and at least three measurements were done for each sample.

4.1.7 Raman Mapping

For the observation of both o-GF and o-GNR distribution in the polymeric matrix, Raman mapping was performed using a LabRAM HR Evolution Raman spectrometer (Horiba Scientific, Japan) with a laser excitation wavelength of 785 nm and with a 100× objective lens. The spectra was recorded at room temperature and the final results were analyzed with a LabSpec6 *software*.

4.1.8 Thermogravimetric Analysis (TGA)

Thermogravimetric analysis was performed on a TA Q500 equipment (TA Instruments, USA). For that, approximately 4 mg of each FS membrane was cut. The samples were heated in nitrogen atmosphere from 40°C-800 °C at a heating rate of 10 °C/min. At least 3 measurements were performed for each sample.

4.1.9 Contact Angle Measurements

The wettability of all surfaces was evaluated by water contact angle measurements. Static contact angle measurements were carried out using the sessile drop method on a contact angle

analyzer from DataPhysics Instruments (Filderstadt, Germany), model OCA 15+, with a high-performance image processing system. A drop (5 μ L) of water was deposited on the sample surface by a motor driven syringe at room temperature and the images were acquired as the drop contacted the surface. The results were analyzed using the SCA20 *software* and at least three measurements were performed on each membrane surface.

4.1.10 Water Uptake (WU)

The produced FS membranes were physically characterized in terms of water uptake by soaking dry membranes, previously weighed, in phosphate buffer saline solution (PBS; Sigma, USA) at 37 °C during 5 min, 15 min, 30 min, 1 h, 3 h, 5 h, 7 h, 24 h and 48 h. After each soaking period, the membranes were taken from PBS solution, the excess was removed with a filter paper and the weight was measured. The water absorption percentage was calculated according to equation (1):

$$\text{Water uptake (\%)} = \frac{W_w - W_d}{W_d} \times 100 \quad (1)$$

where W_w is the weight of the membranes in the swollen state and W_d is the weight in dry conditions.

4.1.11 Weight Loss

For the enzymatic biodegradation tests, samples with 10x10 mm² were pre-weighed and soaked in PBS with sodium azide (0.02% w/v, >99.5%)(Sigma Aldrich, USA) and lysozyme from hen egg white (Sigma-Aldrich, UK) in a concentration of 13 mg/L. The vials were stored in an incubator for 0, 1, 3, 7, 14 and 21 days at 37°C. After each incubation period, the samples were removed from the solution, washed with DW and dried at room temperature. The weight loss was calculated following equation (2):

$$\text{Weight loss (\%)} = \frac{(W_i - W_f)}{W_i} \times 100 \quad (2)$$

where W_i is the initial dry weight of the sample and W_f is the final dry weight of the sample, at each incubation period. Each experiment was repeated three times for each sample, and the average value was taken as the weight loss percentage.

4.1.12 Mechanical Characterization

Dynamic mechanical analysis (DMA) was carried out to evaluate the mechanical/viscoelastic properties of the FS membranes. All measurements were performed using a Tritec2000B DMA from Triton Technology (UK), equipped with the tensile mode. The membranes were cut with ≈ 5 mm width. Prior to the DMA assays, samples were soaked overnight, in a PBS solution, to reach the swelling equilibrium. The geometry of each sample was then measured accurately, the thickness was measured on three different regions of each sample using a micrometer (Mitutoyo, Japan). The measurements were carried out at 37 °C and FS membranes were analyzed immersed in a PBS solution placed in a Teflon® reservoir. FS membranes were clamped in the DMA apparatus with a grip distance of 10 mm and immersed in the PBS bath. After equilibrating at 37 °C, the DMA spectra were obtained performing a frequency scan from 0.1 to 10 Hz. A static pre-load of 1 N was applied during the tests to keep the sample straight. At least three specimens were tested for each condition.

The tensile properties were investigated using a universal mechanical testing equipment (Instron Ltd., UK). Specimens were cut into a rectangular shape (5×20 mm²) and measurements were carried out using 1 kN load under a loading speed of 1 mm/min and a gauge length of 10 mm. At least five samples were tested for each composition, in order to obtain statistically significant data for the ultimate tensile strength and strain at failure. As done in DMA assays, the samples were soaked overnight, in a PBS solution, to reach the swelling equilibrium.

4.1.13 Biological Assays

4.2.13.1 Cell culturing and seeding

L929 mouse fibroblasts line (L929, European Collection of Cell Cultures) were used to test the *in vitro* biocompatibility of the (CHI/ALG/CHI/ALG)₁₀₀, (CHI/ALG/CHI/o-GF)₁₀₀ and (CHI/ALG/CHI/o-GNR)₁₀₀ membranes for 1, 3 and 7 days. Cells were cultured in complete Dulbecco's modified minimum essential medium (DMEM) medium supplemented with 3.7 g/L sodium bicarbonate, 10% FBS and 1% penicillin-streptomycin (pH 7.4), in 150 cm² tissue culture

flasks and incubated at 37 °C in a humidified air atmosphere of 5% CO₂. Every 2-3 days the medium was replaced.

Prior to cell seeding, samples with 10×10 mm² were sterilized by immersion in 70% (v/v) ethanol for 2 h and then washed twice with sterile phosphate buffered saline (PBS). After this, the membranes were immersed in cell culture medium for complete swelling. The cells were seeded in the membranes (in triplicate) at a density of 50 000 cells/sample and nourished with DMEM. The cultures were incubated at 37 °C in a humidified air atmosphere of 5% CO₂.

4.2.13.2 DAPI-phalloidin staining

The morphology and viability of the cells was assessed using fluorescence staining with phalloidin tetramethylrhodamine and 4',6-diamidino-2-phenylindole (DAPI). At each time point DAPI (20 mg/mL, Sigma Aldrich, USA) and phalloidin (20 mg/mL, Sigma Aldrich, USA) were used. Prior to staining, culture medium was removed and the membranes were washed with sterile PBS. Formalin (10%, ThermoFisher) was added for 30 min, to fix the cells of the above samples. After that, formalin was removed and the samples were washed with PBS. Following this, 1 mL of PBS with 10 µL of phalloidin was added and kept at room temperature, protected from light, during 45 min. Subsequently, the samples were washed with PBS and stained with 1 µL of DAPI in 1 mL of PBS for 15 min. After 15 min, the samples were washed again with PBS and images were obtained using an inverted fluorescence microscope (Zeiss, Germany).

4.2.13.3 MTS assay

The metabolic activity of the L929 cells was measured using the MTS colorimetric assay (Cell Titer 96 AQueous One Solution Cell Proliferation Assay, Promega, USA). At each time point the samples were washed with PBS and then immersed in a MTS solution, prepared by using a 1:5 ratio of MTS reagent and serum free cell culture medium and let to incubate in this solution for 3 h at 37 °C with a humidified atmosphere containing 5% CO₂. Afterwards, 100 µL (in triplicate) of each well were transferred to a new 96-well plate and finally the optical density (OD) was read at 490 nm on a multiwell microplate reader (Synergy HT, Bio-Tek Instruments). Three independent experiments were performed for the cytotoxicity tests.

4.2.13.4 DNA quantification

The seeding efficiency and proliferation of cells into the developed membranes was also investigated through the quantification of double-stranded DNA (dsDNA). The DNA was quantified at each time point (1, 3 and 7 days), using the PicoGreen dsDNA kit (Life Technologies, UK). Initially, cells were lysed by osmotic and thermal shock and consecutively the recovered supernatant was read on a microplate reader (BioTek, USA) using a 485 and 528 nm as excitation and emission wavelengths, respectively. Triplicates were performed for each sample and the DNA amounts were calculated using a standard curve.

4.1.14 Statistical Analysis

Data were expressed as average \pm standard deviation (SD) of at least three replicates. Normality tests were performed using Shapiro-Wilk tests. The normality of the population distribution was assessed, and parametric or non-parametric tests were used for normal or non-normal distributions, respectively. For the tensile tests and AFM assays the population was normally distributed and One way Anova followed by Tukey's test were used. In the particular case of the cellular assays, the Two way Anova was used. For WCA assays where the population was not normally distributed Kruskal–Wallis test was employed. The statistical analysis was performed using the *software* GraphPad Prism 6.0 for Windows. Statistical significance was accepted for a $p < 0.05$ (*). The error bars present in the graphics denote the standard deviation.

4.2 Results and Discussion

4.2.1 Structural Characterization of Carbon Nanoparticles Oxides

The oxidation process by the modified Hummers' method was evaluated on both o-EG and o-MWNTs powders. Figure 4.1 a), shows that the thermal degradation of o-EG occurs essentially in two steps presenting a slow weight loss at approximately 150 °C followed by an abrupt decrease in weight for the temperature range of 170 °C to 275 °C indicating that the thermal decomposition of the o-EG started above 170 °C. Regarding the o-MWNTs powder, it can be observed in Figure 4.1 b) that the weight loss occurs in three steps. A continuous slow degradation was verified until approximately 490 °C. The weight loss increases at a faster rate in the range of 490 °C to 590 °C. These values are in agreement with the results shown by Chen *et al.* [44]. In accordance with the authors, the stability of the slope along the degradation process reveals a high purity of the material.

Above 590 °C, the o-MWNT degradation decreases slowly, originating a residual weight loss of $\approx 5\%$, that may be assigned to metal or metal oxide present in the MWNT before the thermal degradation [44]. Below 150 °C the weight loss may be attributed to the evaporation of strongly adsorbed water, revealing a higher water content for o-MWNT compared to o-EG. Above this temperature the thermal degradation of the oxygen-containing functional groups (-OH, -COC-, -CO, -COOH, etc) takes place, producing mainly CO and CO₂. The residual weigh observed above 800 °C is mostly constituted by sp² carbon [45-47]. In general, both materials exhibit similar thermal degradation residue (38.2% and 39.7%, for o-EG and o-MWNT, respectively).

Raman spectroscopy is an useful technique for graphene-based materials characterization. Figure 4.1 c) and d), reveals three major peaks. The first, near 1350 cm⁻¹ (D band), is due to the presence of disorder in the sp² carbon lattice of graphene atoms [3, 45]; the second peak at 1580 cm⁻¹ (G band) is assigned to the E_{2g} phonon mode of graphite, and results from the in-plane bond-stretching motion of the ordered sp² bonded carbon atoms [46, 47]; and the peak at 2700 cm⁻¹ (2D band) has almost the double frequency of the D band and results from the second order Raman scattering [45]. Typically, this last peak can be used to determine the number of stacked layers (up to 5) in few-layer graphene, by the shape, width and position of the peaks [46, 48].

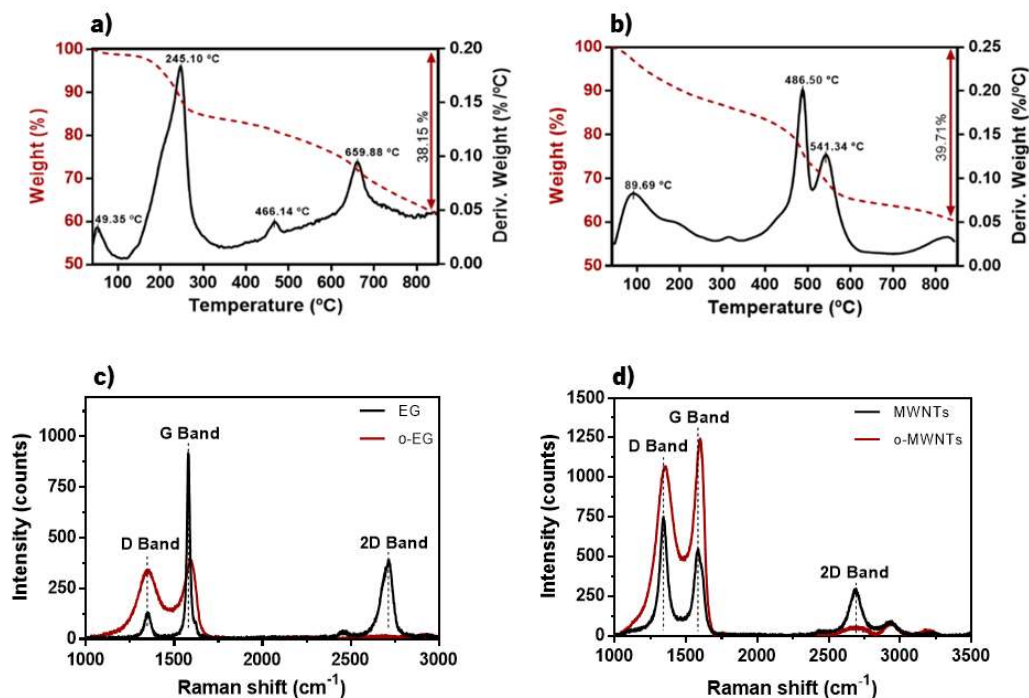


Figure 4.1 TGA thermograms of (a) o-EG and (b) o-MWNTs, under a heating rate of 10 °C/min; (c) and (d) are the Raman spectra obtained at 532 nm for o-EG and pristine EG and o-MWNTs and pristine MWNTs, respectively.

o-EG and o-MWNTs are characterized by broader D and G bands compared to EG and MWNT respectively. For EG an increase in D band intensity is observed after oxidation which may be related with an increase in the graphene structural defect content caused by the oxidation process. The intensity ratio of these two peaks (I_D/I_G) increased from 0.12 to 0.85. The MWNT show an inverse behavior, with a decrease of I_D/I_G from 1.38 to 0.84 in the oxidized material. The ratio between these peaks has been used as a method to predict the disorders caused by chemical covalent modification, ripples, edges and charged impurities [48]. In particular, it was reported that the D peak reveals a weak intensity for edges in a zigzag conformation and a stronger intensity if an armchair edge is formed [48]. For graphite, it is possible to verify an increase in the ratio, which according to the literature suggests a reduction of the in-plane sp^2 character [36]. The different behavior observed for the MWNTs may be explained by the high concentration of defects in the pristine form caused mostly by the production technique. After the oxidation, the resulting o-MWNT show a smaller size with most of the impurities and defects present on the edges. As explained previously, the low D peak intensity present on the oxide state may suggest a zigzag edge conformation. The 2D bands of both Raman spectra, show a large decrease in the intensity after oxidation. This is indicative of a significant loss of regular hexagonal sp^2 carbon lattice after the oxidation procedure. Besides, it reveals that both materials lost their carrier mobility, as suggested by Zhu *et al.* [48].

After ultrasonication of the o-EG and o-MWNTs during 4 h to obtain o-GF and o-GNR, respectively, the water suspensions and solid materials obtained were analyzed. The UV-Vis spectra of o-GF in Figure 4.2 a) (red line) shows an absorption band at 234 nm. The UV-vis spectra may be attributed to $\pi \rightarrow \pi^*$ and $n \rightarrow \pi^*$ electronic transitions of the conjugated bonds. The absorption peak observed for o-GNR solution (dark line) is shifted to higher wavelength, at 246.5 nm, probably related to small differences in the chemical composition of the oxidation products. The obtained values are in agreement with those reported in other works [41, 49].

FTIR analysis was carried out to characterize the chemistry of the functional groups bonded to the oxidized materials. The resulting spectra in Figure 4.2 b), show similar transmittance bands for both materials. The peak at 1708 cm^{-1} for o-GNR is related with the C=O stretching vibration of carboxyl and carbonyl groups that may originate in ketone, while the peak present at 1723 cm^{-1} for o-GF is related with the lactone groups [50]. Both o-GF and o-GNR present a peak near 1580 cm^{-1} (1581 and 1583 , respectively) corresponding to the sp^2 C=C stretching vibrations, and therefore this peak is associated with the non-oxidized graphene domains [51]. The peak present

at approximately 1420 cm^{-1} in both spectra, may be assigned to the deformation vibrations of C-OH groups [51]. For o-GF and o-GNR the peaks observed in the range between $1226\text{--}1110\text{ cm}^{-1}$ may be assigned to stretching vibrations of C-O in alkoxy or epoxy groups [52]. Regarding the wide peak observed near 3403 cm^{-1} , it is associated to the O-H stretching vibration and may be due to the presence of intercalated water [53].

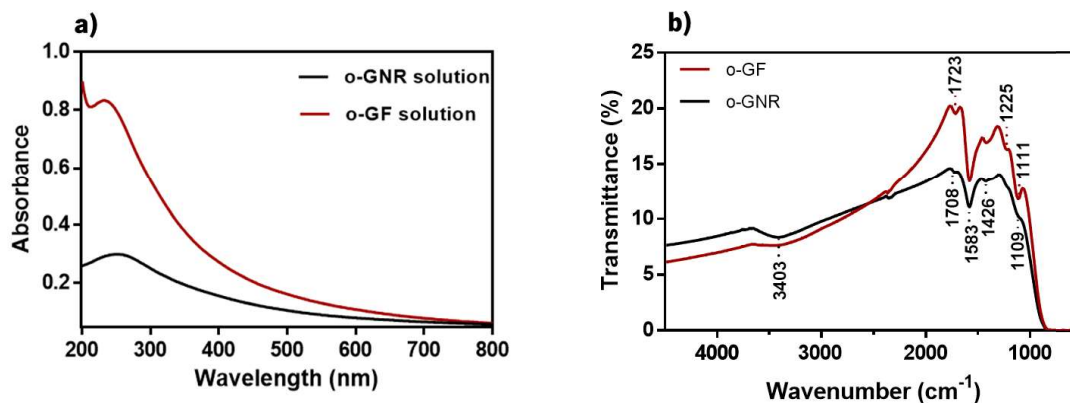


Figure 4.2 (a) UV-Vis spectra of o-GNR (black line) and o-GF (red line) aqueous solution at a concentration of 0.25 mg/mL . **(b)** FTIR spectra of dried o-GNR (black line) and o-GF (red line).

The stability of the colloidal suspension was characterized by zeta potential (ζ) measurements. O-GF presents a zeta value of $-49\pm 9\text{ mV}$ and o-GNR of $-37\pm 8\text{ mV}$. According to the literature these ζ values are indicative that both o-GF and o-GNR are capable to form stable suspensions in water, mainly due to the electrostatic repulsion between the particles, provided by the negative charge, which is caused by the ionization of the carboxylic acid and phenolic groups under basic pH conditions [54, 55].

4.2.2 Scanning Electronic Microscopy (SEM) Analysis

The morphology of both sides of the FS membranes as well as their cross-section were analyzed by SEM. All the membranes were easily removed from the PP substrate and demonstrated an easy handling. SEM images revealed a higher roughness for the upper side of the membranes, Figure 4.3 a₁), b₁) and c₁), when compared to the surface in contact with the substrate, Figure 4.3 a₂), b₂) and c₂), as confirmed by AFM (see section 4.3.3, Figure 4.4) and which has already been described on previous works [39]. The roughness of the side in contact with the substrate increases in the FS membranes that contain o-GF and o-GNR, and was attributed to the these particles embedded in the polymeric matrix, as stated by Ionita *et al.* [16]. Nevertheless, these FS membranes still exhibit a flat morphology which, according with Costa *et al.*, could be an important

characteristic to achieve adhesive properties and thus, to strengthen the adhesion to medical devices or even to anatomic structures such as bone [16, 56]. The addition of o-GF resulted in less porous membranes compared to the controls (Figure 4.3 b₁) and concerning the cross-section (Figure 4.3 b₃), the SEM images exhibit wrinkle-like structures, that were not present in the (CHI/ALG/CHI/ALG)₁₀₀ membranes, and thus may be assigned to the presence of o-GF [18].

The nanocomposite membranes with o-GNR, Figure 4.3 c₁) and c₂), show similar morphology, although with less porosity than the previous ones. The cross-section, Figure 4.3 c₃), shows an ordered layer structure, which was also reported by other authors when GO was added to a polymeric matrix [36, 57]. The orientation of this lamellar structure is parallel to the membrane structure, which possibly may indicate a unidirectional distribution and deposition of o-GNRs [16, 18]. As explained by Han *et al.*, this may also be related to the differences between CHI/ALG and GO properties, namely in the stiffness [58]. Both nanocomposite membranes show a much denser structure, which may arise from the strong interaction between CHI with o-GF and o-GNR, and that would result in an enhancement of the mechanical properties [58]. Moreover, no exposed o-GF or o-GNR sheets were visualized, which emphasizes the strong interaction with the surrounding CHI/ALG molecules, as supported by Li *et al.* [42]. This strong interface may also account for the decrease in the porosity. In general, all membranes showed a homogeneous morphology and some porosity, which is important for nutrients and gases diffusion [39, 59, 60], regarding future applications in the biomedical field.

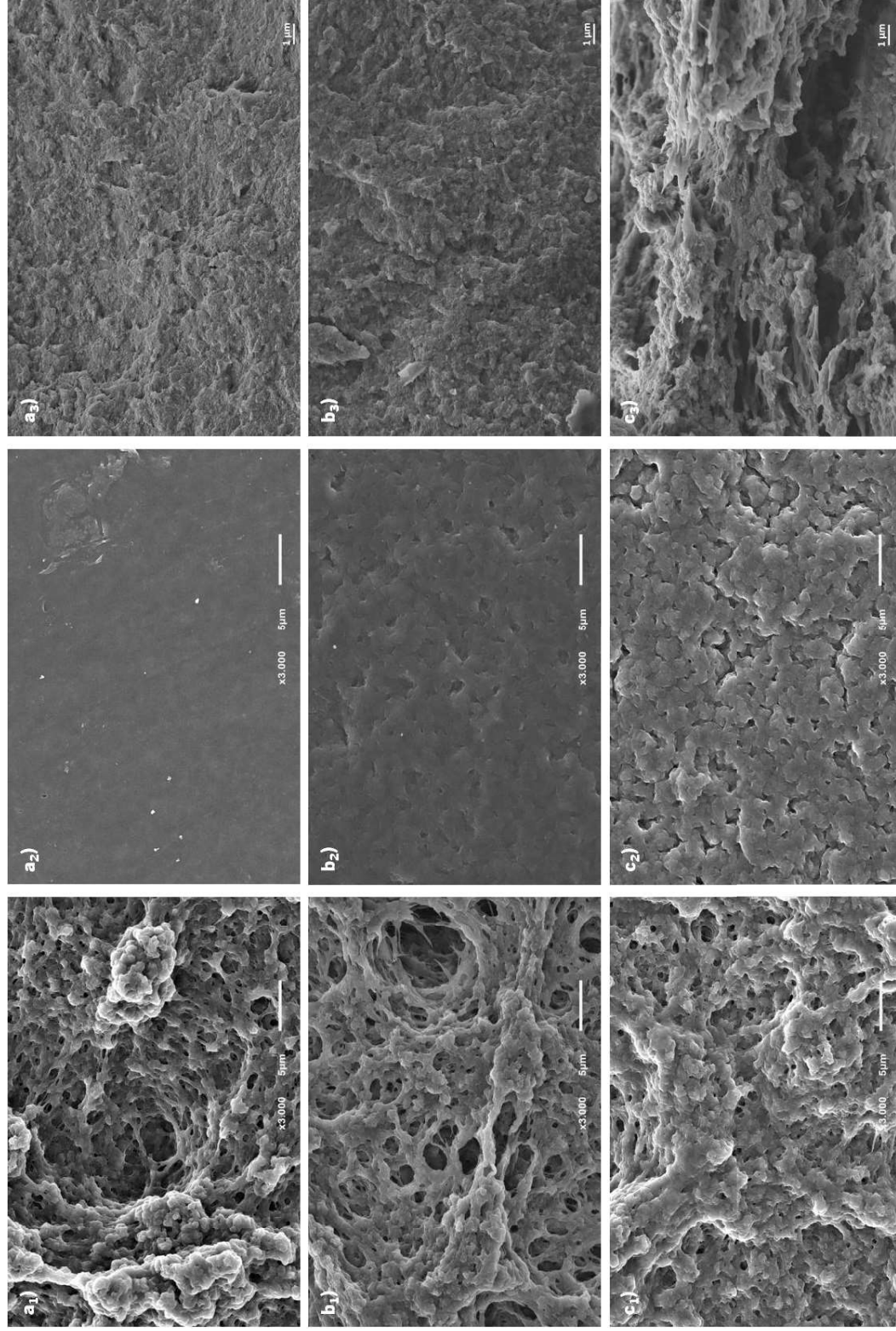


Figure 4.3 SEM images of **(a₁)** upper side and **(a₂)** substrate side of (CHI/ALG/CHI/ALG)₁₀₀FS; **(b₁)** upper side and **(b₂)** substrate side of (CHI/ALG/CHI/ALG)₁₀₀FS; **(c₁)** upper side and **(c₂)** substrate side of (CHI/ALG/CHI/o-GNR)₁₀₀FS. The cross-section of each membrane is depicted on **(a₃)**, **(b₃)** and **(c₃)** micrographs.

4.2.3 AFM Analysis

Surface topographies of the membranes were imaged using AFM. The root-mean-square deviation values of the surface roughness (R_{RMS}) for the region represented in Figure 4.4 a), b) and c) ($5 \times 5 \mu\text{m}^2$) were evaluated. The R_{RMS} (Figure 4.4 d), obtained for the controls have shown that the substrate side is flatter, 49 ± 15 nm, than the upper side of the membranes, 61 ± 21 nm. In fact, the roughness increase may be explained by the significant presence of polymeric loops and tails in the upper side of the membranes, producing rough surface areas, while the side in contact with the substrate, due to its flat topography, will produce a more molecularly smooth surface [61]. Similar roughness observations were achieved by other authors [35, 39] and we also observed such behavior by SEM (Section 4.3.2, Figure 4.4 a) and b)). When o-GF and o-GNR were added to the polymeric matrix, significant changes were visualized. An increase in the roughness of both composite membranes is clearly visible from Figure 4.4 b_i) and c_i), where o-GF membranes demonstrated to reach a roughness value up to 185 ± 10 nm and the o-GNR membranes up to 224 ± 65 nm. Such results were expected, especially for o-GNR once, similarly to what happens to CNT, these structures easily bend or present a twisty morphology, which may result in bundles structures [62]. A similar behavior was described by Gudarzi *et al.* [63]. The increase in the roughness can result in an improvement of the stiffness, fracture toughness and ductility, once the roughness increase suggests an induced crack deflection [64].

The average height (H_{AV}) values are shown in Figure 4.4 e). The H_{AV} range from 40 to 170 nm and when compared with the R_{RMS} it is possible to see that the values almost match, indicating that although a roughness area was achieved with the adding of oxidized nanoparticles, the roughness is constant along the membranes. At last, it is worth mentioning that the surface roughness on the substrate side does not change significantly with the presence of o-GF and o-GNR, and for that reason their 2D and 3D images were not represented.

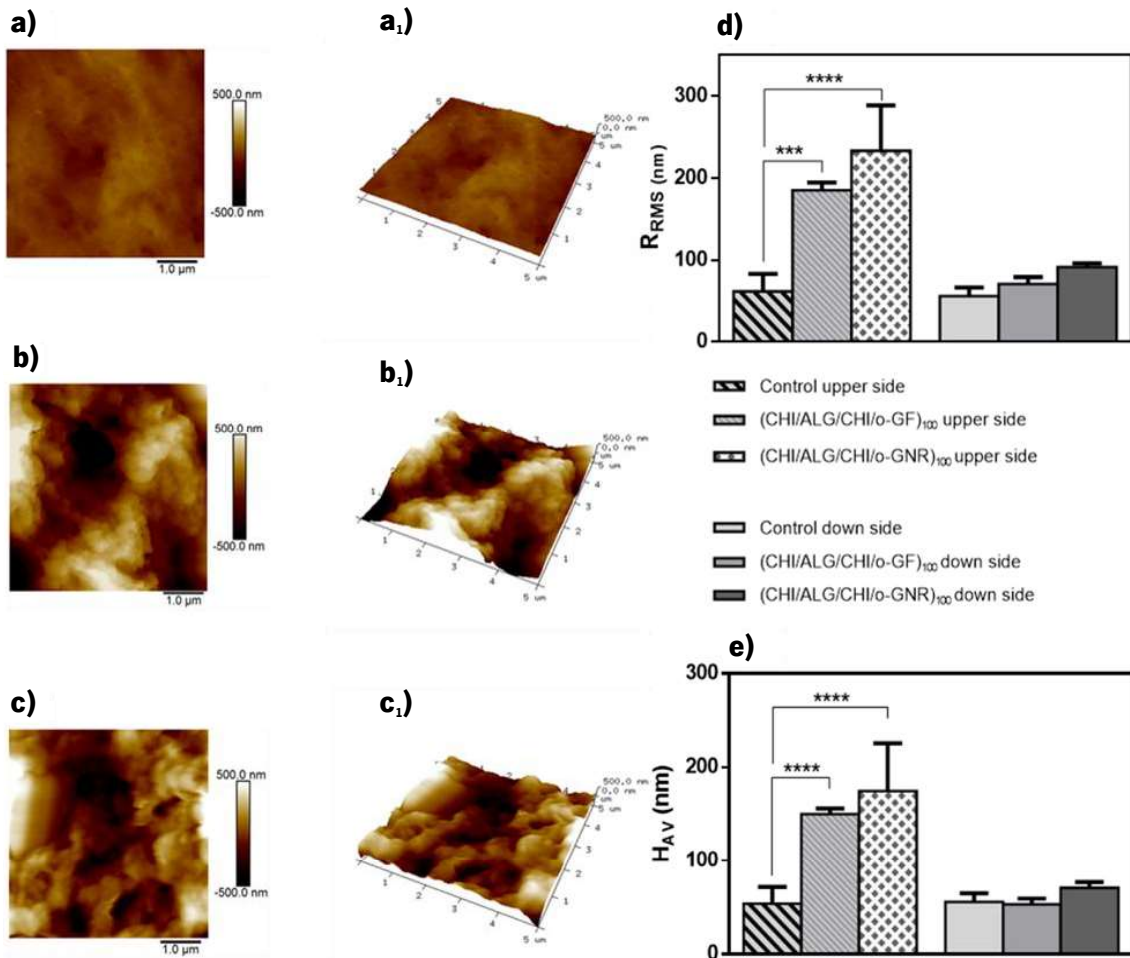


Figure 4.4 AFM surface images with respective 3D representation of: controls FS membranes (**a; a₁**), (CHI/ALG/CHI/o-GF)₁₀₀ membranes (**b; b₁**) and (CHI/ALG/CHI/o-GNR)₁₀₀ membranes (**c; c₁**). (**d**) R_{RMS} and (**e**) is the H_{AV} . Significant differences were state for $p < 0.001$ (***) and $p < 0.0001$ (****).

4.2.4 Raman Mapping

Raman mapping was used to analyze the o-GF and o-GNR dispersion in the CHI/ALG matrix, Figure 4.5 a) and c), respectively. In order to map the nanoparticles dispersion, the integrated intensity was calculated over the spectral range of $1500-1700\text{ cm}^{-1}$ (G peak) as indicated in Figure 4.5 e) and f). The spectra compare the o-GF and o-GNR acquired in the membrane and directly on the nanoparticles, using a wavelength excitation of 785 nm. The blue color intensity correlates with the concentration of o-GF and o-GNR in the membrane, within a thickness of approximately $1\text{ }\mu\text{m}$. The presence of o-GF and o-GNR was continuously observed along the FS membranes, for the mapping of at least three samples of each material.

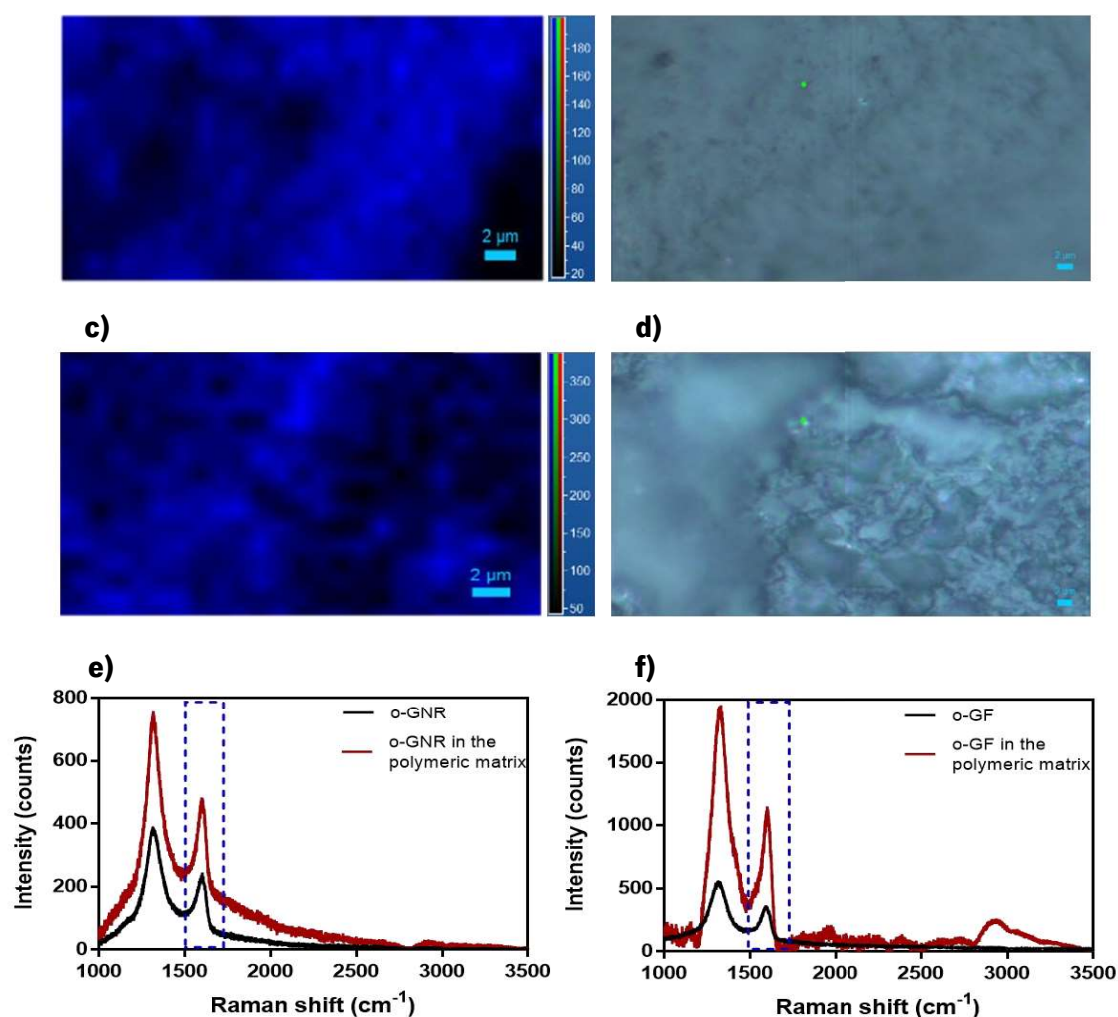


Figure 4.5 (a,c) Distribution of o-GNR and o-GF (blue) in the polymeric matrix (CHI/ALG) obtained by Raman spectroscopy, with respective intensity color scale (a.u); **(b,d)** optical image of the o-GNR and o-GF composite membranes; **(e,f)** Raman spectra obtained for the o-GNR and o-GF before (black line) and after the dispersion (red line) in the (CHI/ALG) matrix, respectively.

4.2.5 TGA Analysis

The thermal stability and the weight composition of o-GF and o-GNR containing FS membranes were evaluated by TGA. Figure 4.6 a) illustrates that all the membranes present a similar initial weight loss that may be related to the elimination of strongly adsorbed water. The total weight loss measured after thermal decomposition, at the end of the TGA test, shows a higher final weight % when o-GF and o-GNR are present, indicating that the fillers were successfully incorporated within the polymers and allowing the approximate quantification of their weight content. The difference in residual weight measured from the composite with o-GF to the composite with layered polymers was approximately 1.6 wt.%, while for the o-GNR composite it was

approximately 1.1 wt.%. Considering that the o-GF and o-GNR alone present a residual weight that may be near 62 and 60 wt.%, respectively, when heat treated to 800 °C in inert atmosphere (Figure 4.1 a) and b)), the weight composition of fillers in the FS membranes may be estimated to be up to 2.6 wt.% and 1.8 wt.% for o-GF and o-GNR, respectively.

Analyzing the thermograms and corresponding DTGA (Figure 4.6 a) and b)), it is observed that the thermal stability of the composite membranes remain unaltered with the addition of o-GF and o-GNR.

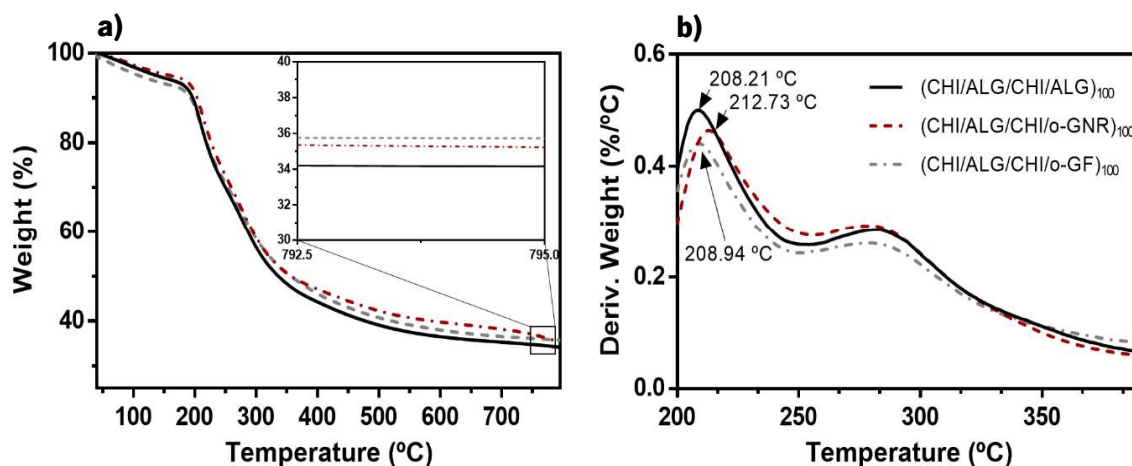


Figure 4.6 TGA graphic representation (a) Thermogravimetric (TGA) curves with inset showing a magnification for the temperature range of 792.5-795 °C and (b) Derivative of the weight loss curves (DTGA) for all membranes, as a function of temperature (°C).

4.2.6 Water Contact Angle (WCA) Measurements

The results of the WCA measurements made for the obtained FS membranes are depicted in Figure 4.7. It is observed that, independently of the side, the control membranes (CHI/ALG/CHI/ALG)₁₀₀ show a WCA around 100°. This finding is supported by similar results shown by Silva *et al.* for CHI/ALG films [59].

For the FS membranes containing o-GF and o-GNR, two different behaviors are observed. On the side in contact with the substrate during the LbL process (down side), it is possible to verify that no significant changes occurred, when compared to the controls membranes. This is explained by the presence of the same material layer, CHI, and thus the same behavior is obtained. Regarding the upper side of the nanocomposite membranes, significant changes were verified. Both, (CHI/ALG/CHI/o-GF)₁₀₀ and (CHI/ALG/CHI/o-GNR)₁₀₀, show a decrease in the WCA presenting values of $77.37 \pm 5.51^\circ$ and $79.92 \pm 4.54^\circ$, respectively. In other words, both membranes turned

hydrophilic when both forms of GO were added. This result is supported by other works that reported a WCA of 30.7° for GO, as well as, by the capability of this material to establish hydrogen bonds due to the carboxylate groups present on the edge of the GO structure [65]. Comparing the upper side of the GO membranes, it is possible to see that no significant changes occurred, showing that the effects of the groups present on the surface are similar for both oxidized graphene flakes and graphene nanoribbons are similar.

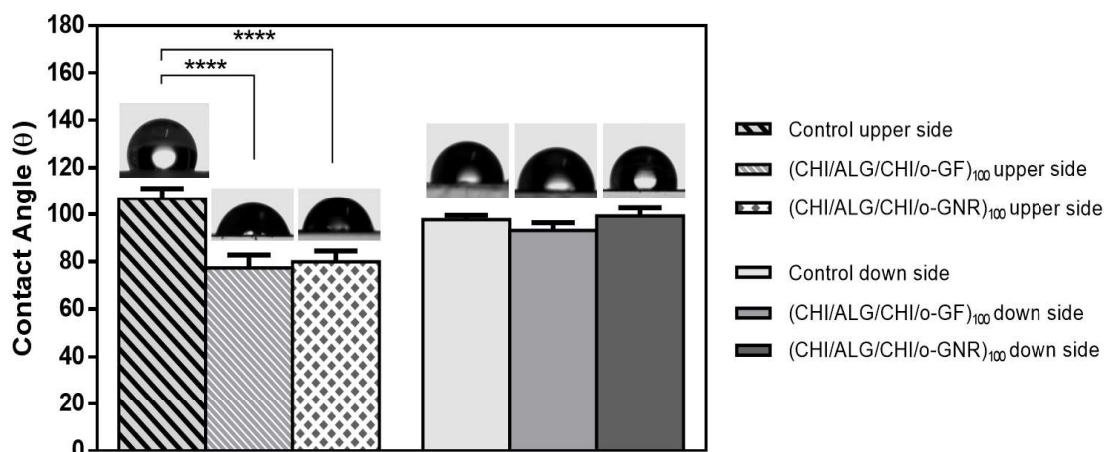


Figure 4.7 Water contact angle results with representative images for both sides of all membranes. Significant differences were state for $p < 0.0001$ (****).

4.2.7 Swelling Ability Studies

The swelling behavior of the produced FS membranes was evaluated during 48 h in PBS medium at 37°C - see Figure 4.8. Concerning the $(\text{CHI}/\text{ALG}/\text{CHI}/\text{ALG})_{100}$ control membranes, the results show that they attain the equilibrium after 3 h reaching a maximum swelling of approximately 280 %. Globally, it is verified that the incorporation of both forms of GO in the polymeric matrix reduce the water uptake (WU) of the nanocomposite FS membranes and more time is necessary to achieve the WU equilibrium. This behavior may result from the lower space for water storage capacity and decrease in the expansion ratio, caused by hydrogen bonding between the GO and the CHI, as suggested by Li *et al.* [42]. The SEM images also corroborate these results (Section 4.3.2, Figure 4.3), once a decrease in the porosity was verified when o-GF and o-GNR were added, hindering the WU capability. Although the addition of GO led to hydrophilic membranes, the decrease in the WU could be explained by the bridge between GO and CHI, in a process similar to the one observed for genipin and CHI [59]. Therefore, the addition of both GO to the CHI/ALG membranes seems to control the swelling behavior, showing the ability to replace

other cross-linking methods, as suggested in literature, and to be potentially applied as, heart valves or skin scaffolds [42].

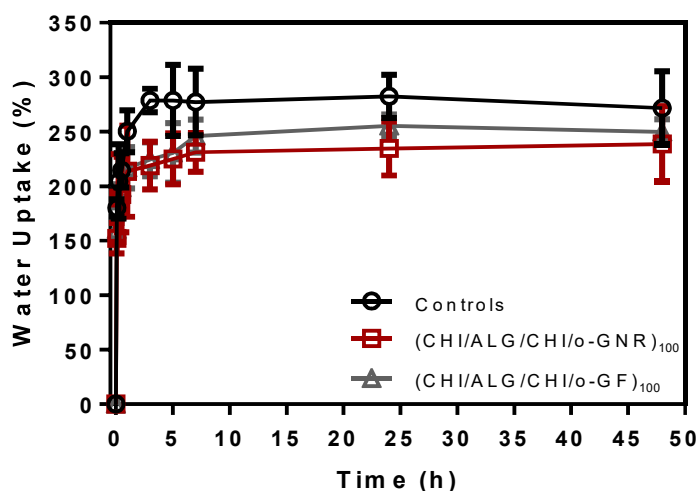


Figure 4.8. Variation of the water uptake ability as a function of time of (CHI/ALG/CHI/ALG)₁₀₀ (black round symbol), (CHI/ALG/CHI/o-GF)₁₀₀ (grey triangle symbol) and (CHI/ALG/CHI/o-GNR)₁₀₀ (red square symbol) in PBS at 37 °C.

4.2.8 Biodegradation Studies

When implanted in human body, a biomaterial should be capable of provide a sustainable platform for cell proliferation/differentiation and potential growth and replacement of a tissue. Among several factors, the degradation rate is one of the most important, once it is required that the formation of the new tissue matches with the degradation of the material [66]. In order to assess this feature, lysozyme was used to study the degradation behavior of the FS membranes. This enzyme is present in different human tissues, cells, and fluids, in different concentrations around 7-13 mg/L [67]. For convenience, the maximum concentration was employed during the study.

Figure 4.9 indicates that the controls FS membranes always reach a higher and faster weight loss than the nanocomposite membranes. The degradation assays that were performed with PBS medium, both nanocomposite membranes present a weight loss around 15% of its initial weight in which the degradation is more pronounced in the first three days. In turn, the (CHI/ALG/CHI/ALG)₁₀₀ control membranes possess a weight loss of about 25% of their initial weight up to 21 days. Higher weight loss values are verified when lysozyme is used as the degradation medium. Although both nanocomposite membranes present higher degradation in the presence of the enzyme their weight loss does not exceed the values shown by the control membranes in PBS.

Furthermore, the (CHI/ALG/CHI/ALG)₁₀₀ membranes, when immersed in lysozyme, were the more degraded materials reaching 35% of weight loss. These results indicate that the incorporation of o-GF and o-GNR seems to induce a greater resistance to degradation. One of the reasons to explain this performance may be related with the water uptake capability. As seen previously, the nanocomposite membranes possess lower capability to swell and thus, the amount of PBS and enzyme entering into the polymeric matrix is lower, resulting in a lower weight loss. Moreover, the observable weight loss in the nanocomposite membranes could result from lysozyme immobilization on the GO surface. As reported in literature, the surface that is rich of functional groups of GO allows the immobilization of the lysozyme through electrostatic interactions [68], avoiding the degradation of the material. The obtained results are corroborated with the literature [42].

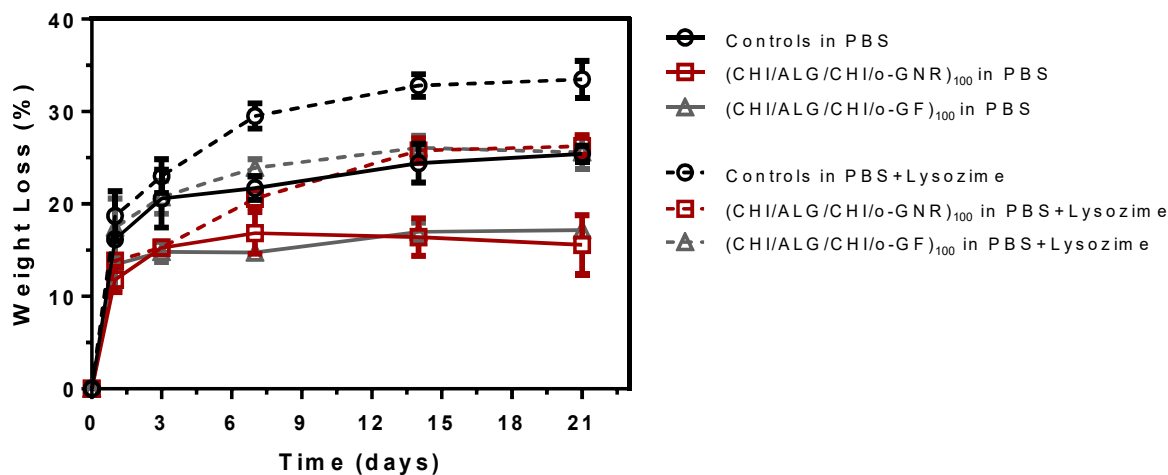


Figure 4.9 Degradation behavior of (CHI/ALG/CHI/ALG)₁₀₀ (black round symbol), (CHI/ALG/CHI/o-GF)₁₀₀ (grey triangle symbol) and (CHI/ALG/CHI/o-GNR)₁₀₀ (red square symbol) FS membranes when immersed in PBS or Lysozyme over a period of 21 days at 37 °C.

4.2.9 DMA Analysis

DMA experiments were performed to evaluate the effects of the incorporation of GO on the mechanical/viscoelastic properties of CHI/ALG FS membranes. The variation of the storage (elastic) modulus E' along the frequency is presented in Figure 4.10 a). Overall, for all the FS membranes studied, E' increases with frequency as already reported in other works [35, 40]. Such behavior is even more pronounced for the FS membranes containing o-GNR. Figure 4.10 a) shows that the addition of o-GF and o-GNR results in an increased stiffness of the membranes, reaching values 2 times and 4 times higher than the controls, respectively, being in agreement with other

graphene-reinforced polymer composite work [69], where it was found that even for an amount as low as 0.1 wt% an increase in stiffness of approximately 2 times was verified [69]. Such values are also supported by the water uptake tests, where it was shown that the ability of the nanocomposite membranes to swell decreases relative to the polymer composite membranes (see Section 4.3.7).

Tan δ is the ratio of the amount of energy dissipated by viscous mechanisms relative to energy stored in the elastic component providing information about the damping properties of the membranes. Tan δ is very similar for all FS membranes exhibiting a slight increase with the frequency (Figure 4.10 b)). The control membrane and the FS membranes containing o-GF presented slightly higher dissipative properties at the higher frequencies, which can be related to their lower stiffness. Moreover, since tan δ presents values between 0.1 and 0.3, the membranes show a viscoelastic performance, revealing an important feature for biomedical applications, since the living tissues and their biological constituents also exhibit a viscoelastic behavior [35, 70].

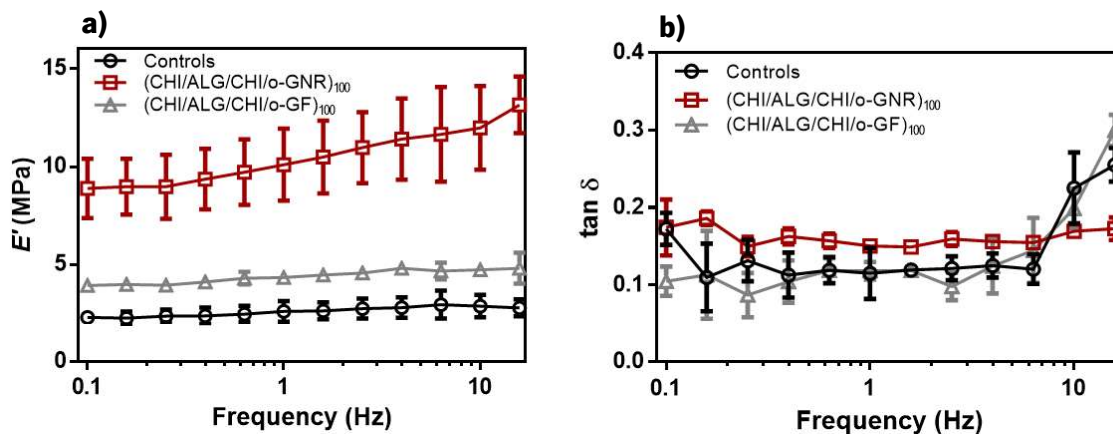


Figure 4.10 DMA measurements. Variation of the Storage modulus (a) and the loss factor (b) along a frequency scan ranging from 0.1-15 Hz, at 37°C of the FS membranes while immersed in PBS to closely simulate the physiological conditions.

4.2.10 Tensile Tests

The mechanical behavior of the FS membranes was also characterized by tensile tests. The ultimate tensile strength (UTS) and strain at failure (ϵ_b) values are presented in Figure 4.11 a) and b), respectively. Figure 4.11 a) shows that when the membranes contained o-GF and o-GNR as fillers, a higher UTS is achieved reaching 1.98 ± 0.28 MPa (two times higher than the controls; $p < 0.0001$) and 1.20 ± 0.21 MPa ($p < 0.001$), respectively. This improvement suggests that GO and the polymer matrix are strongly bonded through chemical interactions, such as hydrogen bonds [58], with the ability to achieve an uniform stress distribution, possibly due to the alignment of GO

in the polymeric matrix (see Section 4.3.2) minimizing the presence of stress concentration spots and leading to a stronger material [16, 18].

The elongation at break, Figure 4.11 b), presents a significant difference between the controls and o-GF ($p < 0.0001$) and o-GNR ($p < 0.0001$), duplicating for o-GF and increasing 2.5 times for o-GNR. This may result from the strong interfacial adhesion between the oxidized nanoparticles and the polymer [71]. The strain increase could also result from the slippage of the different GO sheets when stress is applied [72]. Thus, the addition of o-GF and o-GNR results in a simultaneous increase of the strength, stiffness and ductility of the membranes, as reported by other authors for similar materials [73, 74].

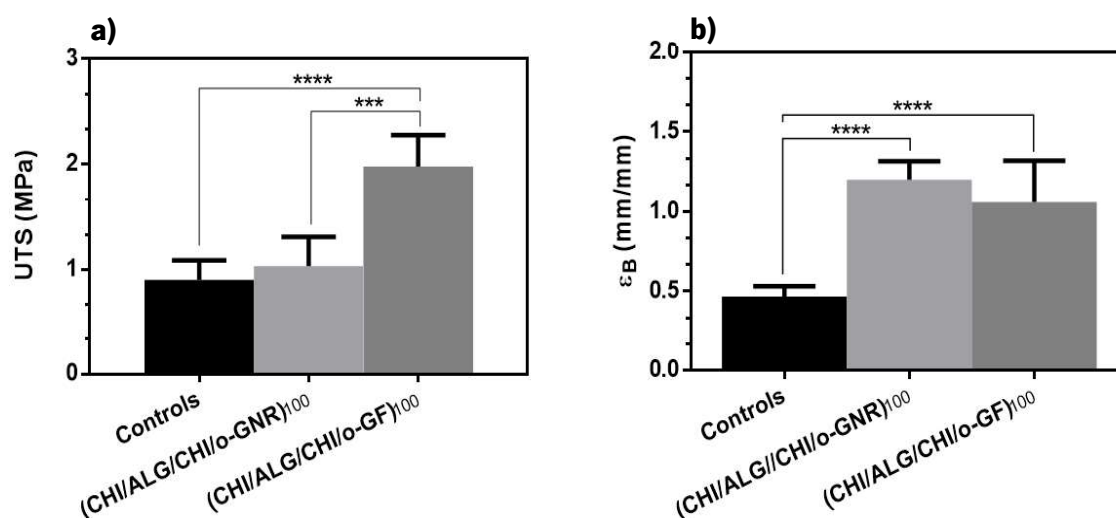


Figure 4.11 Representation and comparison of mechanical properties of controls, o-GNR and o-GF composite membranes. **(a)** Ultimate tensile strength (UTS) and **(b)** strain at break (ϵ_B). Significant differences were found for $p < 0.001$ (***) and $p < 0.0001$ (****).

4.2.11 Biological assays

The cytocompatibility of the produced membranes was evaluated by *in vitro* culture with L929 cells on the membranes during 1, 3 and 7 days. To understand how cells adhered to the FS membranes and which morphology they presented, a DAPI-phalloidin test was performed (Figure 4.12). Comparing all the formulations it can be noticed that cells behave quite differently for each condition. Although presenting a round shape on day 1, the cells start to adhere to the membranes' surface; the (CHI/ALG/CHI/o-GNR)₁₀₀ formulation is the one that presents less cells attached on their surface. After 3 days, it is seen an increase in cell number on controls and (CHI/ALG/CHI/o-GF)₁₀₀ membranes, where cells are well spread and anchored to the membranes surface. However,

such effect is not verified on the (CHI/ALG/CHI/o-GNR)₁₀₀ membranes in which no significant changes on cell density and morphology of the cells is noticed by comparing to day 1. On day 7, (CHI/ALG/CHI/o-GNR)₁₀₀ membranes still exhibit poor proliferation, although some cells started to reveal a stretched shape morphology. On the other hand, (CHI/ALG/CHI/ALG)₁₀₀ and (CHI/ALG/CHI/o-GF)₁₀₀ membranes present an increase in cell proliferation, being almost all the surface area covered by adhered cells, especially for the ones that contain o-GF. Moreover, after 7 days, the cells on the (CHI/ALG/CHI/o-GF)₁₀₀ FS membrane show a similar morphology and behavior when compared with tissue culture polystyrene (TCPS).

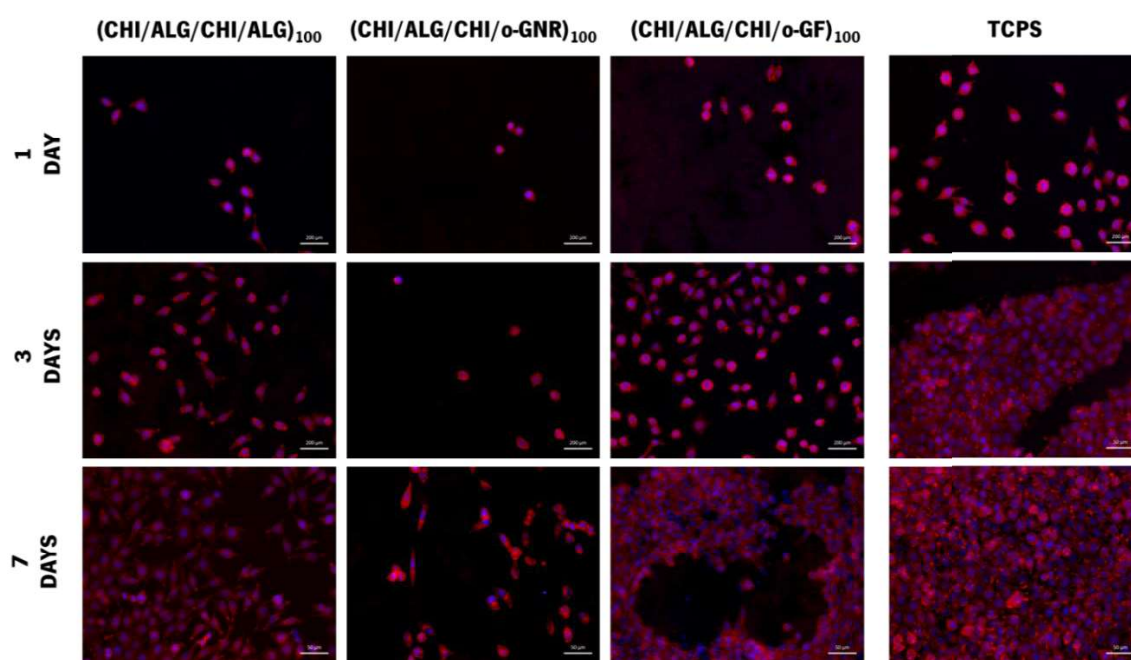


Figure 4.12 Evaluation of cells' morphology using DAPI for nuclei staining (blue labeled) and phalloidin for F-actin filaments staining (red labeled) by fluorescence microscopy at 1, 3, and 7 days post-seeding on (CHI/ALG/CHI/ALG)₁₀₀, (CHI/ALG/CHI/o-GNR)₁₀₀ and (CHI/ALG/CHI/o-GF)₁₀₀ FS membranes.

MTS assays were used to evaluate the cellular viability on the FS membranes - Figure 4.13

a). Overall, all conditions present an increase in cell viability over the time period of the experiments. At day 1, TCPS present significant differences in relation to the (CHI/ALG/CHI/o-GNR)₁₀₀ ($p < 0.05$) FS membranes. At day 3, TCPS are significantly different from all the FS membranes ($p < 0.0001$) by comparing it to (CHI/ALG/CHI/ALG)₁₀₀ and (CHI/ALG/CHI/o-GNR)₁₀₀ and ($p < 0.001$) in the case of (CHI/ALG/CHI/o-GF)₁₀₀. On day 7, the same differences as day 3 are verified between the TCPS and the FS membranes. Moreover, at this time point, significant differences could be observed by comparing (CHI/ALG/CHI/o-GNR)₁₀₀ with (CHI/ALG/CHI/ALG)₁₀₀ ($p < 0.01$) and with (CHI/ALG/CHI/o-GF)₁₀₀ ($p < 0.0001$). Such results revealed that, concerning the produced

membranes, (CHI/ALG/CHI/o-GF)₁₀₀ are the FS membranes that allow cells to express better metabolic activity and the (CHI/ALG/CHI/o-GNR)₁₀₀ are the ones that exhibit the lower metabolic activity.

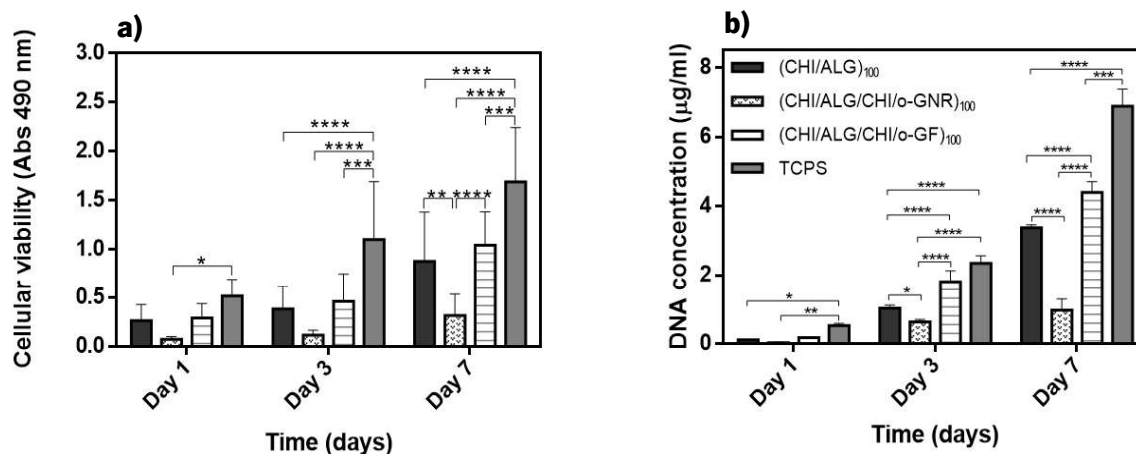


Figure 4.13 (a) Cellular viability analysis for (CHI/ALG/CHI/ALG)₁₀₀, (CHI/ALG/CHI/o-GNR)₁₀₀ and (CHI/ALG/CHI/o-GF)₁₀₀ membranes using the MTS assay for 1,3 and 7 days. (b) DNA quantification assay performed on (CHI/ALG/CHI/ALG)₁₀₀, (CHI/ALG/CHI/o-GNR)₁₀₀ and (CHI/ALG/CHI/o-GF)₁₀₀. Significant differences were found for $p < 0.05$ (*), $p < 0.01$ (**), $p < 0.001$ (***) and $p < 0.0001$ (****), $N=3$.

The cell proliferation over a period of 7 days was assessed by DNA quantification (Figure 4.13 b)). Analyzing the graph, it is possible to verify that along with the culture time all formulations led to an increase in cell proliferation. Comparing all the formulations with TCPS at day 1, significant differences are observed for (CHI/ALG/CHI/ALG)₁₀₀ ($p < 0.05$) and for (CHI/ALG/CHI/o-GNR)₁₀₀ ($p < 0.01$). In the case, of (CHI/ALG/CHI/o-GF)₁₀₀ no significant differences are observed. On day 3, significant differences are observed between (CHI/ALG/CHI/o-GNR)₁₀₀ and (CHI/ALG/CHI/ALG)₁₀₀ ($p < 0.05$) and (CHI/ALG/CHI/o-GF)₁₀₀ ($p < 0.0001$). Moreover, at this time point no significant differences are found between (CHI/ALG/CHI/o-GF)₁₀₀ and TCPS but, significant differences are found in the case of (CHI/ALG/CHI/ALG)₁₀₀ ($p < 0.0001$). At day 7 it is observed a pronounced increase on cell proliferation in the case of (CHI/ALG/CHI/ALG)₁₀₀ that lead to higher differences when comparing this condition to the (CHI/ALG/CHI/o-GNR)₁₀₀ ones ($p < 0.0001$). Moreover, the (CHI/ALG/CHI/o-GF)₁₀₀ condition is significantly different in relation to (CHI/ALG/CHI/o-GNR)₁₀₀ ($p < 0.0001$) and (CHI/ALG/CHI/ALG)₁₀₀ ($p < 0.0001$).

The biological results demonstrated that the presence of o-GF and o-GNR in the polymeric matrix lead to different effects on the L929 cell behavior. Observing the data obtained, when o-GF is present a better metabolic activity, adhesion and proliferation are verified when compared to (CHI/ALG/CHI/ALG)₁₀₀ and (CHI/ALG/CHI/o-GNR)₁₀₀ and, in some cases, the results are

comparable with TCPS. According with the literature, this improvement on cells' spreading and proliferation is the result of the hydrophilic behavior demonstrated previously, once cells adhere better to moderate hydrophilic surfaces rather than hydrophobic or super hydrophilic surfaces, creating a more suitable surface that may result in a fibronectin functionality maintenance [75, 76]. The roughness increase it is also pointed as a factor that could help fibronectin adsorption [75, 77]. Moreover, the stiffness increase and water uptake decrease also contributed to an enhanced cellular behavior, since cells tend to prefer stiffer and lower hydration membranes [78, 79]. These results are consistent with other works where GO were used as filler of different polymeric matrix and where a benefic effect was verified when GO was incorporated [15, 80, 81]. Thus, due to the significant increase of the cell proliferation, improved mechanical properties, enhanced thermal stability, these membranes may find a wide number of applications, such as: wound healing, cardiac and bone engineering.

Unlike the previous membranes, (CHI/ALG/CHI/o-GNR)₁₀₀ membranes resulted in a reduction of L929 viability, adhesion and proliferation. Since these membranes present similar morphological, mechanical and physical properties as (CHI/ALG/CHI/o-GF)₁₀₀ membranes, including WCA, stiffness and water uptake, the poor cell adhesion exhibited by these membranes is attributed to the o-GNR filler. In fact, a possibility to these behavior may be related on the o-GNR structure, i.e, these GO derivatives have a ribbon-like structure while o-GF possess a flake-like structure, thus it is hypothesized that ribbons structures may cause physical damage on cells membranes, namely through the blade like action of these structures [82]. Moreover, and as reported in bibliography, the functionalization of graphene based materials with oxygen atoms leads to a positive effect on the cytotoxicity, so another factor that may have contributed to this effect on the (CHI/ALG/CHI/o-GNR)₁₀₀ membranes is the possibility of some of the MWNTs have not been totally unzipped and so they do not exhibit a good functionalization of the surface, reducing their cytocompatibility. Along with this feature, the presence of some impurities on MWNTs, including metal catalysts used for MWNTs production that could be still entrapped on o-GNR structures would also reduce cytocompatibility [69, 83].

4.3 Conclusions

In summary, (CHI/ALG/CHI/o-GF)₁₀₀ and (CHI/ALG/CHI/o-GNR)₁₀₀ multilayered FS membranes were successfully developed by the LbL process. Significant changes in the membranes morphology were found when compared with the control (CHI/ALG/CHI/ALG)₁₀₀,

including in terms of roughness and porosity. Infrared spectroscopy showed that o-GF and o-GNR contained different C=O functional groups, and zeta potential measurements confirmed the higher polarity of the o-GF aqueous suspensions. These differences in chemical composition also reflected on the membranes' surface wettability characteristics. Thermogravimetric analysis allowed the approximate determination of the o-GF and o-GNR overall weight content of 2.6% and 1.8%, respectively. Moreover, the good dispersion of both nanofillers was confirmed by Raman spectroscopy mapping that was consequential for the membranes dynamic and static mechanical properties, including the elastic modulus and UTS. An increase in the resistance to degradability and decreased swelling in aqueous environments was measured. The biological assays indicated that the cells on the surface of the FS membranes with o-GF were viable and were able to proliferate over a period of 7 days. Concerning the (CHI/ALG/CHI/o-GNR)₁₀₀ further work needs to be carried out to understand the reduced cytocompatibility of the o-GNR containing membranes, in particular to ascertain if it is due to lower hydrophilicity or if residual metal catalysts, originating on the carbon nanotubes used, are still present. If the latter effect is discarded, future work may contemplate the production of membranes with an inner core of o-GNR layers for high mechanical reinforcement, and outer o-GF layers with good mechanical properties and high cell proliferation ability. Future work may include the production of o-GNR from metal-free CNT.

Ultimately, and according with the obtained results, it was demonstrated that the developed (CHI/ALG/CHI/o-GF)₁₀₀ membranes exhibit interesting characteristics that can provide essential features for biomedical applications, including wound healing, cardiac and bone engineering.

Acknowledgements

This work was supported by BioSea Glue and by LA ICVS/3BS-2015-2017 projects. This work was also financially supported by Foundation for Science and Technology (FCT) through the scholarship SFRH/BPD/96797/2013 granted to Sofia G. Caridade and through the scholarship SFRH/BD/97606/2013 granted to Maria Sousa.

4.5 References

- [1] Slonczewski JC, Weiss PR. Band structure of graphite. *Physical Review*. 1958;109:272-9.
- [2] Geim AK, Novoselov KS. The rise of graphene. *Nature Materials*. 2007;6:183-91.
- [3] Chen J, Yao BW, Li C, Shi GQ. An improved Hummers method for eco-friendly synthesis of graphene oxide. *Carbon*. 2013;64:225-9.
- [4] Novoselov KS, Fal'ko VI, Colombo L, Gellert PR, Schwab MG, Kim K. A roadmap for graphene. *Nature*. 2012;490:192-200.
- [5] Mayorov AS, Gorbachev RV, Morozov SV, Britnell L, Jalil R, Ponomarenko LA, et al. Micrometer-Scale Ballistic Transport in Encapsulated Graphene at Room Temperature. *Nano Letters*. 2011;11:2396-9.
- [6] Wang Y, Li YM, Tang LH, Lu J, Li JH. Application of graphene-modified electrode for selective detection of dopamine. *Electrochemistry Communications*. 2009;11:889-92.
- [7] Feng LY, Chen Y, Ren JS, Qu XG. A graphene functionalized electrochemical aptasensor for selective label-free detection of cancer cells. *Biomaterials*. 2011;32:2930-7.
- [8] Chen BA, Liu M, Zhang LM, Huang J, Yao JL, Zhang ZJ. Polyethylenimine-functionalized graphene oxide as an efficient gene delivery vector. *Journal of Materials Chemistry*. 2011;21:7736-41.
- [9] Feng LZ, Zhang SA, Liu ZA. Graphene based gene transfection. *Nanoscale*. 2011;3:1252-7.
- [10] Lee WC, Lim C, Shi H, Tang LAL, Wang Y, Lim CT, et al. Origin of Enhanced Stem Cell Growth and Differentiation on Graphene and Graphene Oxide. *ACS Nano*. 2011;5:7334-41.
- [11] Lim HN, Huang NM, Lim SS, Harrison I, Chia CH. Fabrication and characterization of graphene hydrogel via hydrothermal approach as a scaffold for preliminary study of cell growth. *International Journal of Nanomedicine*. 2011;6:1817-23.
- [12] Park S, Ruoff RS. Chemical methods for the production of graphenes. *Nature Nanotechnology*. 2009;4:217-24.
- [13] Kim J, Cote LJ, Kim F, Yuan W, Shull KR, Huang JX. Graphene Oxide Sheets at Interfaces. *Journal of the American Chemical Society*. 2010;132:8180-6.
- [14] Hu KS, Kulkarni DD, Choi I, Tsukruk VV. Graphene-polymer nanocomposites for structural and functional applications. *Progress in Polymer Science*. 2014;39:1934-72.
- [15] Wang K, Ruan J, Song H, Zhang JL, Wo Y, Guo SW, et al. Biocompatibility of Graphene Oxide. *Nanoscale Research Letters*. 2011;6:8.
- [16] Ionita M, Pandele MA, Iovu H. Sodium alginate/graphene oxide composite films with enhanced thermal and mechanical properties. *Carbohydrate Polymers*. 2013;94:339-44.
- [17] Pei SF, Cheng HM. The reduction of graphene oxide. *Carbon*. 2012;50:3210-28.
- [18] Pandele AM, Ionita M, Crica L, Dinescu S, Costache M, Iovu H. Synthesis, characterization, and in vitro studies of graphene oxide/chitosan-polyvinyl alcohol films. *Carbohydrate Polymers*. 2014;102:813-20.
- [19] Nayak TR, Andersen H, Makam VS, Khaw C, Bae S, Xu XF, et al. Graphene for controlled and accelerated osteogenic differentiation of human mesenchymal stem cells. *ACS Nano*. 2011;5:4670-8.

- [20] Shin SR, Aghaei-Ghareh-Bolagh B, Gao XG, Nikkhah M, Jung SM, Dolatshahi-Pirouz A, et al. Layer-by-layer assembly of 3d tissue constructs with functionalized graphene. *Advanced Functional Materials*. 2014;24:6136-44.
- [21] Ikada Y, Tsuji H. Biodegradable polyesters for medical and ecological applications. *Macromolecular Rapid Communications*. 2000;21:117-32.
- [22] Mano JF, Silva GA, Azevedo HS, Malafaya PB, Sousa RA, Silva SS, et al. Natural origin biodegradable systems in tissue engineering and regenerative medicine: present status and some moving trends. *J R Soc Interface*. 2007;4:999-1030.
- [23] Kumar M. A review of chitin and chitosan applications. *Reactive & Functional Polymers*. 2000;46:1-27.
- [24] Jayakumar R, Prabakaran M, Kumar PTS, Nair SV, Tamura H. Biomaterials based on chitin and chitosan in wound dressing applications. *Biotechnology Advances*. 2011;29:322-37.
- [25] Sudarshan NR, Hoover DG, Knorr D. Antibacterial action of chitosan. *Food Biotechnology*. 1992;6:257-72.
- [26] Ong SY, Wu J, Moochhala SM, Tan MH, Lu J. Development of a chitosan-based wound dressing with improved hemostatic and antimicrobial properties. *Biomaterials*. 2008;29:4323-32.
- [27] Liakos I, Rizzello L, Scurr DJ, Pompa PP, Bayer IS, Athanassiou A. All-natural composite wound dressing films of essential oils encapsulated in sodium alginate with antimicrobial properties. *International Journal of Pharmaceutics*. 2014;463:137-45.
- [28] Orive G, Ponce S, Hernandez RM, Gascon AR, Igartua M, Pedraz JL. Biocompatibility of microcapsules for cell immobilization elaborated with different type of alginates. *Biomaterials*. 2002;23:3825-31.
- [29] Croisier F, Jerome C. Chitosan-based biomaterials for tissue engineering. *European Polymer Journal*. 2013;49:780-92.
- [30] Rinaudo M. Chitin and chitosan: Properties and applications. *Progress in Polymer Science*. 2006;31:603-32.
- [31] Rane KD, Hoover DG. Production of chitosan by fungi. *Food Biotechnology*. 1993;7:11-33.
- [32] Aranaz I, Harris R, Heras A. Chitosan Amphiphilic Derivatives. *Chemistry and Applications. Current Organic Chemistry*. 2010;14:308-30.
- [33] Huang XF, Sun YF, Nie JY, Lu WT, Yang L, Zhang ZL, et al. Using absorbable chitosan hemostatic sponges as a promising surgical dressing. *International Journal of Biological Macromolecules*. 2015;75:322-9.
- [34] Tada DB, Singh S, Nagesha D, Jost E, Levy CO, Gultepe E, et al. Chitosan film containing poly(d,l-lactic-co-glycolic acid) nanoparticles: a platform for localized dual-drug release. *Pharmaceutical Research*. 2010;27:1738-45.
- [35] Silva JM, Duarte ARC, Caridade SG, Picart C, Reis RL, Mano JF. Tailored freestanding multi layered membranes based on chitosan and alginate. *Biomacromolecules*. 2014;15:3817-26.
- [36] Tang L, Li X, Du D, He CJ. Fabrication of multilayer films from regenerated cellulose and graphene oxide through layer-by-layer assembly. *Progress in Natural Science-Materials International*. 2012;22:341-6.

- [37] Borges J, Mano JF. Molecular Interactions Driving the layer-by-layer assembly of multilayers. *Chemical Reviews*. 2014;114:8883-942.
- [38] Martins GV, Merino EG, Mano JF, Alves NM. Crosslink effect and albumin adsorption onto chitosan/alginate multilayered systems: an in situ qcm-d study. *Macromolecular Bioscience*. 2010;10:1444-55.
- [39] Caridade SG, Monge C, Gilde F, Boudou T, Mano JF, Picart C. Free-standing polyelectrolyte membranes made of chitosan and alginate. *Biomacromolecules*. 2013;14:1653-60.
- [40] Caridade SG, Monge C, Almodovar J, Guillot R, Lavaud J, Josserand V, et al. Myoconductive and osteoinductive free-standing polysaccharide membranes. *Acta Biomaterialia*. 2015;15:139-49.
- [41] Justin R, Chen BQ. Characterisation and drug release performance of biodegradable chitosan-graphene oxide nanocomposites. *Carbohydrate Polymers*. 2014;103:70-80.
- [42] Li JH, Ren N, Qiu JC, Mou XN, Liu H. Graphene oxide-reinforced biodegradable genipin-cross-linked chitosan fluorescent biocomposite film and its cytocompatibility. *International Journal of Nanomedicine*. 2013;8:3415-26.
- [43] Liu Y, Park M, Shin HK, Pant B, Choi J, Park YW, et al. Facile preparation and characterization of poly(vinyl alcohol)/chitosan/graphene oxide biocomposite nanofibers. *Journal of Industrial and Engineering Chemistry*. 2014;20:4415-20.
- [44] Chen XH, Chen CS, Chen Q, Cheng FQ, Zhang G, Chen ZZ. Non-destructive purification of multi-walled carbon nanotubes produced by catalyzed CVD. *Materials Letters*. 2002;57:734-8.
- [45] Singh V, Joung D, Zhai L, Das S, Khondaker SI, Seal S. Graphene based materials: Past, present and future. *Progress in Materials Science*. 2011;56:1178-271.
- [46] Weng XX, Cao QX, Liang LX, Chen JR, You CP, Ruan YM, et al. Simultaneous determination of dopamine and uric acid using layer-by-layer graphene and chitosan assembled multilayer films. *Talanta*. 2013;117:359-65.
- [47] Venkanna M, Chakraborty AK. Synthesis and characterizations of graphene oxide and reduced graphene oxide nanosheets. 58th DAE Solid State Physics Symposium. Patiala, INDIA: Amer Inst Physics; 2013. p. 574-6.
- [48] Zhu YW, Murali S, Cai WW, Li XS, Suk JW, Potts JR, et al. Graphene and graphene oxide: synthesis, properties, and applications. *Advanced Materials*. 2010;22:3906-24.
- [49] Kosynkin DV, Higginbotham AL, Sinitskii A, Lomeda JR, Dimiev A, Price BK, et al. Longitudinal unzipping of carbon nanotubes to form graphene nanoribbons. *Nature*. 2009;458:872-U5.
- [50] Guo HL, Wang XF, Qian QY, Wang FB, Xia XH. A Green Approach to the synthesis of graphene nanosheets. *Acs Nano*. 2009;3:2653-9.
- [51] Acik M, Lee G, Mattevi C, Pirkle A, Wallace RM, Chhowalla M, et al. The role of oxygen during thermal reduction of graphene oxide studied by infrared absorption spectroscopy. *Journal of Physical Chemistry C*. 2011;115:19761-81.
- [52] Navarro-Pardo F, Martinez-Barrera G, Martinez-Hernandez AL, Castano VM, Rivera-Armenta JL, Medellin-Rodriguez F, et al. Effects on the thermo-mechanical and crystallinity properties of nylon 6,6 electrospun fibres reinforced with one dimensional (1D) and two dimensional (2D) carbon. *Materials*. 2013;6:3494-513.

- [53] Gao RG, Hu NT, Yang Z, Zhu QR, Chai J, Su YJ, et al. Paper-like graphene-Ag composite films with enhanced mechanical and electrical properties. *Nanoscale Research Letters*. 2013;8:8.
- [54] Konkana B, Vasudevan S. Understanding Aqueous dispersibility of graphene oxide and reduced graphene oxide through pK(a) measurements. *Journal of Physical Chemistry Letters*. 2012;3:867-72.
- [55] Li D, Muller MB, Gilje S, Kaner RB, Wallace GG. Processable aqueous dispersions of graphene nanosheets. *Nature Nanotechnology*. 2008;3:101-5.
- [56] Costa RR, Neto AI, Calgeris I, Correia CR, Pinho ACM, Fonseca J, et al. Adhesive nanostructured multilayer films using a bacterial exopolysaccharide for biomedical applications. *Journal of Materials Chemistry B*. 2013;1:2367-74.
- [57] Cano M, Khan U, Sainsbury T, O'Neill A, Wang ZM, McGovern IT, et al. Improving the mechanical properties of graphene oxide based materials by covalent attachment of polymer chains. *Carbon*. 2013;52:363-71.
- [58] Han DL, Yan LF, Chen WF, Li W. Preparation of chitosan/graphene oxide composite film with enhanced mechanical strength in the wet state. *Carbohydrate Polymers*. 2011;83:653-8.
- [59] Silva JM, Caridade SG, Oliveira NM, Reis RL, Mano JF. Chitosan-alginate multilayered films with gradients of physicochemical cues. *Journal of Materials Chemistry B*. 2015;3:4555-68.
- [60] Hajicharalambous CS, Lichter J, Hix WT, Swierczewska M, Rubner MF, Rajagopalan P. Nano- and sub-micron porous polyelectrolyte multilayer assemblies: Biomimetic surfaces for human corneal epithelial cells. *Biomaterials*. 2009;30:4029-36.
- [61] Shiratori SS, Rubner MF. pH-dependent thickness behavior of sequentially adsorbed layers of weak polyelectrolytes. *Macromolecules*. 2000;33:4213-9.
- [62] Olek M, Ostrander J, Jurga S, Mohwald H, Kotov N, Kempa K, et al. Layer-by-layer assembled composites from multiwall carbon nanotubes with different morphologies. *Nano Letters*. 2004;4:1889-95.
- [63] Gudarzi MM, Sharif F. Enhancement of dispersion and bonding of graphene-polymer through wet transfer of functionalized graphene oxide. *Express Polymer Letters*. 2012;6:1017-31.
- [64] Rafiee MA, Rafiee J, Srivastava I, Wang Z, Song HH, Yu ZZ, et al. Fracture and Fatigue in Graphene Nanocomposites. *Small*. 2010;6:179-83.
- [65] Goenka S, Sant V, Sant S. Graphene-based nanomaterials for drug delivery and tissue engineering. *Journal of Controlled Release*. 2014;173:75-88.
- [66] Reis RL, Neves NM, Mano JF, Gomes ME, Marques AP, Azevedo HS. *Natural-Based Polymers for Biomedical Applications*. Elsevier; 2008. p. 832.
- [67] Hankiewi.J, Swiercze.E. Lysozyme in human body-fluids. *Clinica Chimica Acta*. 1974;57:205-9.
- [68] Zhang JL, Zhang F, Yang HJ, Huang XL, Liu H, Zhang JY, et al. Graphene oxide as a matrix for enzyme immobilization. *Langmuir*. 2010;26:6083-5.
- [69] Fan HL, Wang LL, Zhao KK, Li N, Shi ZJ, Ge ZG, et al. Fabrication, mechanical properties, and biocompatibility of graphene-reinforced chitosan composites. *Biomacromolecules*. 2010;11:2345-51.

- [70] Mano JF, Reis RL, Cunha AM. Dynamic mechanical analysis in polymers for medical applications. *Polymer Based Systems on Tissue Engineering, Replacement and Regeneration*. 2002;86:139-64.
- [71] Wan CY, Chen BQ. Reinforcement and interphase of polymer/graphene oxide nanocomposites. *Journal of Materials Chemistry*. 2012;22:3637-46.
- [72] Liu RY, Xu AW. Byssal threads inspired ionic cross-linked narce-like graphene oxide paper with superior mechanical strength. *Rsc Advances*. 2014;4:40390-5.
- [73] Wan CY, Frydrych M, Chen BQ. Strong and bioactive gelatin-graphene oxide nanocomposites. *Soft Matter*. 2011;7:6159-66.
- [74] Yang XM, Tu YF, Li LA, Shang SM, Tao XM. Well-dispersed chitosan/graphene oxide nanocomposites. *Acs Applied Materials & Interfaces*. 2010;2:1707-13.
- [75] Wilson CJ, Clegg RE, Leavesley DI, Pearcy MJ. Mediation of biomaterial-cell interactions by adsorbed proteins: A review. *Tissue Engineering*. 2005;11:1-18.
- [76] Mendelsohn JD, Yang SY, Hiller J, Hochbaum AI, Rubner MF. Rational design of cytophilic and cytophobic polyelectrolyte multilayer thin films. *Biomacromolecules*. 2003;4:96-106.
- [77] Richert L, Lavalle P, Payan E, Shu XZ, Prestwich GD, Stoltz JF, et al. Layer by layer buildup of polysaccharide films: Physical chemistry and cellular adhesion aspects. *Langmuir*. 2004;20:448-58.
- [78] Picart C, Elkaim R, Richert L, Audoin T, Arntz Y, Cardoso MD, et al. Primary cell adhesion on RGD-functionalized and covalently crosslinked thin polyelectrolyte multilayer films. *Advanced Functional Materials*. 2005;15:83-94.
- [79] Hillberg AL, Holmes CA, Tabrizian M. Effect of genipin cross-linking on the cellular adhesion properties of layer-by-layer assembled polyelectrolyte films. *Biomaterials*. 2009;30:4463-70.
- [80] Pinto AM, Moreira S, Goncalves IC, Gama FM, Mendes AM, Magalhaes FD. Biocompatibility of poly(lactic acid) with incorporated graphene-based materials. *Colloids and Surfaces B-Biointerfaces*. 2013;104:229-38.
- [81] Chang YL, Yang ST, Liu JH, Dong E, Wang YW, Cao AN, et al. In vitro toxicity evaluation of graphene oxide on A549 cells. *Toxicology Letters*. 2011;200:201-10.
- [82] Pinto AM, Goncalves IC, Magalhaes FD. Graphene-based materials biocompatibility: A review. *Colloids and Surfaces B-Biointerfaces*. 2013;111:188-202.
- [83] Smart SK, Cassady AI, Lu GQ, Martin DJ. The biocompatibility of carbon nanotubes. *Carbon*. 2006;44:1034-47.

CHAPTER 5. CONCLUSIONS AND FUTURE WORK

5. CONCLUSIONS AND FUTURE WORK

5.1 General Conclusions

Many attempts have been made in order to improve the mechanical properties of natural polymers. Several works have been reported that the use of graphene oxide (GO) nanocomposite materials as nanofillers could be a good strategy to improve the mechanical properties of polymeric matrix as well as to provide physical and chemical conditions for the development of new tissues capable of influencing the proliferation and differentiation of different cells.

In order to take advantages of the outstanding properties of both natural polymers and GO, the development of free-standing (FS) membranes composed of natural polymers and GO intended for biomedical applications was the focus of this thesis. Firstly, we were able to synthesize, using a modified Hummers' method, two different kinds of GO: oxidized graphene flakes (o-GF) and oxidized graphene nanoribbons (o-GNR) from exfoliated graphite and multi-walled carbon nanotubes, respectively. The success of the oxidation process had a pivotal importance once oxygen functional groups improved the bonding between the polymeric matrix and GO and also renders it a soluble character, capability of loading drugs and physiological stability. The oxidation process was confirmed by several techniques that allowed to verify the presence of such functional groups and where it was also possible to confirm the presence of some non-oxidized graphene domains. Moreover, both o-GF and o-GNR presented a negative zeta potential that was an important parameter for the establishment of the deposition sequence during the buildup of the FS membranes. Afterwards, we utilized the layer-by-layer (LbL) technology for the production of FS membranes. The membranes were named as (CHI/ALG/CHI/o-GF)₁₀₀, (CHI/ALG/CHI/o-GNR)₁₀₀ and (CHI/ALG/CHI/ALG)₁₀₀ where the last ones were used as controls. All the FS membranes produced could be easily and reproducibly prepared in mild conditions without any post-processing step to detach them and were very easy to handle. The morphological characterization revealed that the presence of o-GF and o-GNR led to rougher and highly orientated membranes, with a homogenous and unidirectional distribution of oxidized nanoparticles along the polymeric matrix, particularly in the case of (CHI/ALG/CHI/o-GNR)₁₀₀ membranes. The presence of both o-GF and o-GNR also conducted to hydrophilic membranes with no significant changes on thermal stability. Moreover, the incorporation of both GO induced a greater resistance to degradation and enhanced

mechanical properties such as strength, stiffness and ductility as compared with the control membranes. Finally, the biological data demonstrated that the presence of o-GF in the CHI/ALG matrix led to an enhanced biological performance, showing a good proliferation and higher viability of the cells seeded on this membranes. On the other hand, the presence of o-GNR turned the membranes less cytocompatible comparing with CHI/ALG control membranes and (CHI/ALG/CHI/o-GF)₁₀₀.

The data obtained in this thesis suggests that the incorporation of GO in polymeric matrix can be promising for future biomedical applications. For instance, (CHI/ALG/CHI/o-GF)₁₀₀ could be used for wound healing, for tissue engineering particularly for bone and heart tissue applications. Although valuable outcomes were obtained, much research must be done in order to direct the developed membranes for specific applications envisaged.

5.2 Future Work

As aforementioned, due to the valuable results obtained in this work, more research must be done in order to fully understand the behavior of such devices and to explore new potential fields of application. Therefore, the following topics are suggested as future work:

- (1) To fully understand and control the oxidation process of graphene. Although the synthesis has been widely studied where different procedures have been suggested, the uniformity from batch to batch is very difficult. In fact, the type of starting material and the modifications undertaken during the oxidation reaction, usually results in materials with different levels of impurities and dispersibility. Thus, it is extremely important to establish some uniformity to minimize the heterogeneity of GO.
- (2) To study the possibility to restore the conductive properties of graphene. In literature it has been reported that the graphene possess conductive properties and when oxidized this property is lost. Thus, it could be very interesting to investigate if our synthesized GO possess such non-conductive characteristic and if the GO have such property, it could be useful to try restore it. For that, we propose to use UV-irradiation or to use natural antioxidants during the LbL process, such as melatonin or even cinnamon. Such conductive properties could be very interesting for cardiac applications.
- (3) To study the possibility to mix GO within the ALG polymeric solutions for the LbL process. This strategy is suggested to maximize the stability of the GO solution. In this thesis, we

demonstrated that strong interactions between the natural polymers used and the GO. However, it could be interesting to investigate the properties of the FS membranes with the GO dissolved within the alginate solution.

- (4) Depending on the type of application envisaged, deep biological assays need to be performed in order to check if the FS membranes could be adequate substrates for cell adhesion, proliferation and differentiation.